Diss. ETH No. 28678

SEGREGATION AND FINGERING INSTABILITY IN GRANULAR MEDIA

A thesis submitted to attain the degree of

DOCTOR OF SCIENCES OF ETH ZURICH
(Dr. sc. ETH Zürich)

presented by

MENG LIU

M. Sc. Chinese Academy of Sciences
born on 13.01.1991
citizen of P. R. China

accepted on the recommendation of
Prof. Dr. Christoph Müller, examiner
Prof. Dr. Alexander Penn, co-examiner
Prof. Dr. Fernando Hernández Jiménez, co-examiner

2022

Meng Liu
Segregation and Fingering Instability in Granular Media
Diss. ETH No. 28678

ABSTRACT

Granular systems are ubiquitous in both industry and nature, yet we still know comparatively little of the physics governing their dynamics. Owing to this lack of insight, there is still no continuum description of granular systems that can describe accurately phenomena that are commonly encountered such as segregation. Hence, this doctoral thesis is concerned with obtaining a better understanding of phenomena that occur in bi-disperse granular systems, i.e. the dynamics and segregation of intruders and the formation of Rayleigh-Taylor-like fingering structures.

First, the doctoral thesis investigates the motion of a single intruder in dynamic granular systems, i.e., a dense shear flow and a vibro-fluidized bed. To this end, we develop a granular buoyancy model using a generalization of the Archimedean formulation of the buoyancy force inspired by previous work on buoyancy in chute flows. The first model system that was studied is a convection-free vibrated system, allowing us to calculate the buoyancy force through three different approaches, i.e., a generalization of the Archimedean formulation, the spring force of a virtual spring and through the granular pressure field. The buoyancy forces obtained through these three approaches agree very well, providing strong evidence for the validity of the generalization of the Archimedean formulation of the buoyancy force which only requires information about the solid fraction of the intruder (defined as ratio of its volume to its Voronoi volume), hence allowing for a calculation of the buoyancy force that is computationally efficient as coarse-graining is avoided. In a second step to increase the complexity of the granular system, convection is introduced. In such a system, the lift force acting on the intruder is composed of granular buoyancy and a drag force. Using a drag model for the slow velocity regime, the lift force, directly measured through a virtual spring, is predicted accurately via the proposed generalization of the Archimedean formulation of granular buoyancy. The lift force model developed here allowed us in turn to rationalize the dependence of the lift force on the density of the bed particles and the intruder diameter, and the independence of the

lift force on the intruder density and the vibration strength (once a critical value is exceeded).

Next, we develop a new lift force model to describe the motion of intruders in dense, granular shear flows. Our derivation is based on the thermal buoyancy model of Trujillo and Hermann (2003) but takes into account both granular temperature and pressure differences in the derivation of the net buoyancy force acting on the intruder. We further extend the model to take into account also density differences between the intruder and the bed particles. The model predicts very well the rising and sinking of intruders, the lift force acting on intruders as determined by discrete element model (DEM) simulations and the neutral-buoyancy limit of intruders in shear flows. Phenomenologically, we observe that the presence of an intruder leads to a cooling effect and a local flattening of the shear velocity profile (lower shear rate). The cooling effect increases with intruder size and explains the sinking of large intruders. On the other hand, the introduction of small to mid-sized intruders, i.e., up to 4 times the bed particle size, leads to a reduction in the granular pressure compared to the hydrostatic pressure, which in turn explains the rising of small to mid-sized intruders.

Lastly, we turn to a newly discovered Rayleigh-Taylor (RT)-like fingering instability in binary granular media. Fingering instabilities akin to the Rayleigh-Taylor (RT) instability in fluids have been observed in a binary granular system in which dense and small particles are layered on top of lighter and larger particles, when the system is subjected to vertical vibration and fluidizing gas flow. Using observations from experiments and numerical modelling we explore whether the theory developed to describe the Rayleigh-Taylor (RT) instability in fluids is also applicable to binary granular systems. Our results confirm multiple key properties of the RT instability theory for binary granular systems: (i) The characteristic wavenumber is constant with time, (ii) the amplitude of the characteristic wavenumber initially grows exponentially and (iii) the dispersion relation between the wavenumbers k of the interface instability and the growth rates $n(k)$ of their amplitudes holds also for binary granular systems. Our results show that inter-particle friction is essential for the RT instability to occur in granular media. For zero particle friction the interface instability bears a greater resemblance to the Richtmyer-Meshkov instability. We further define a yield criterion Y by treating the granular medium as a viscoplastic material; only for $Y > 15$ fingering occurs.

Interestingly, previous works has shown that instabilities in the Earth's lower mantle, another viscoplastic material, also occur for similar values of Y.

ZUSAMMENFASSUNG

Granulare Systeme sind sowohl in der Industrie als auch in der Natur allgegenwärtig, jedoch wissen wir immer noch vergleichsweise wenig über die physikalischen Grundlagen ihrer Dynamik. Aufgrund dieser mangelnden Kentniss gibt es immer noch keine Kontinuumsbeschreibung granularer Systeme, welche häufig auftretende Phänomene wie Entmischung genau beschreiben könnte. Diese Dissertation strebt daher nach einem besseren Verständnis von Phänomenen, die in bi-dispersen granularen Systemen auftreten, d.h. die Dynamik und Entmischung von Fremdkörpern und die Bildung von Rayleigh-Taylor-ähnlichen Fingerstrukturen.

In dieser Dissertation wird zunächst die Bewegung eines einzelnen Fremdkörpers in dynamischen granularen Systemen, d.h. einer dichten Scherströmung und einem vibro-fluidisierten Bett, untersucht. Zu diesem Zweck wird ein granulares Auftriebsmodell entwickelt, das eine Verallgemeinerung der archimedischen Formulierung der Auftriebskraft verwendet, die von früheren Arbeiten über den Auftrieb in Rutschenströmungen inspiriert wurde. Das erste untersuchte Modellsystem ist ein konvektionsfreies, vibrierendes System, das es uns ermöglicht, die Auftriebskraft durch drei verschiedene Ansätze zu berechnen, nämlich durch eine Verallgemeinerung der archimedischen Formulierung, durch die Federkraft einer virtuellen Feder und durch das granulare Druckfeld. Die mit diesen drei Ansätzen erhaltenen Auftriebskräfte stimmen sehr gut überein, was ein starker Beweis für die Gültigkeit der Verallgemeinerung der archimedischen Formulierung der Auftriebskraft ist, welche nur Informationen über den Feststoffanteil des Fremdkörpers (definiert als Verhältnis seines Volumens zu seinem Voronoi-Volumen) erfordert und somit eine Berechnung der Auftriebskraft ermöglicht, die rechnerisch effizient ist, da sogenanntes coarse-graining vermieden wird. In einem zweiten Schritt, der die Komplexität des granularen Systems erhöht, wird Konvektion eingeführt. In einem solchen System setzt sich die auf den Fremdkörper wirkende Auftriebskraft aus dem granularen Auftrieb und einer Widerstandskraft zusammen. Unter Verwendung eines Widerstandsmodells für langsame granulare Strömungen wird die Auftriebskraft, die direkt über eine virtuelle Feder gemessen wird, durch die vorgeschlagene Verallgemeinerung der archimedischen Formulierung des granularen

Auftriebs genau vorhergesagt. Das hier entwickelte Auftriebskraftmodell ermöglichte es uns wiederum, die Abhängigkeit der Auftriebskraft von der Dichte der Bettpartikel und dem Durchmesser des Fremdkörpers sowie die Unabhängigkeit der Auftriebskraft von der Dichte des Fremdkörpers und der Vibrationsstärke (sobald ein kritischer Wert überschritten wird) zu erklären.

Anschließend entwickeln wir ein neues Auftriebskraftmodell zur Beschreibung der Bewegung von Fremdkörpern in dichten, granularen Scherströmungen. Unsere Herleitung basiert auf dem thermischen Auftriebsmodell von Trujillo und Hermann (2003), berücksichtigt aber sowohl die Temperatur- als auch die Druckunterschiede im Granulat bei der Herleitung der Nettoauftriebskraft, die auf den Fremdkörper wirkt. Wir erweitern das Modell weiter, um auch Dichteunterschiede zwischen dem Fremdkörper und den Bettpartikeln zu berücksichtigen. Das Modell prognostiziert sehr gut das Aufsteigen und Absinken von Fremdkörpern, die auf Fremdkörper wirkende Auftriebskraft, bestimmt durch Simulationen mit der Diskrete-Elemente-Methode (DEM) und den Grenzwert bei welchem der Auftrieb auf Fremdkörper in Scherströmungen verschwindet. Phänomenologisch beobachten wir, dass die Anwesenheit eines Fremdkörpers zu einem Kühleffekt und einer lokalen Abflachung des Schergeschwindigkeitsprofils (geringere Scherrate) führt. Der Kühleffekt nimmt mit der Größe des Fremdkörpers zu und erklärt das Absinken großer Fremdkörper. Andererseits führt die Einführung von kleinen bis mittelgroßen Fremdkörpern, d. h. bis zum Vierfachen der Bettpartikelgröße, zu einer Verringerung des Granulatdrucks im Vergleich zum hydrostatischen Druck, was wiederum das Aufsteigen von kleinen bis mittelgroßen Fremdkörpern erklärt.

Schließlich befassen wir uns mit einer neu entdeckten Rayleigh-Taylor (RT) ähnlichen Fingerinstabilität in binären granularen Medien. Fingerinstabilitäten, die der RT-Instabilität in Flüssigkeiten ähneln, wurden in einem binären granularen System beobachtet, in dem dichte und kleine Partikel auf leichteren und größeren Partikeln geschichtet sind, wenn das System vertikalen Vibrationen und einem fluidisierenden Gasstrom ausgesetzt ist. Anhand von Beobachtungen aus Experimenten und numerischen Modellen untersuchen wir, ob die Theorie, die zur Beschreibung der RT-Instabilität in Flüssigkeiten entwickelt wurde, auch auf binäre granulare Systeme anwendbar ist. Unsere Ergebnisse bestätigen mehrere Schlüsseleigenschaften der RT-Instabilitätstheorie für binäre granulare

Systeme: (i) Die charakteristische Wellenzahl ist zeitlich konstant, (ii) die Amplitude der charakteristischen Wellenzahl wächst zunächst exponentiell und (iii) die Dispersionsbeziehung zwischen den Wellenzahlen k der Grenzflächeninstabilität und den Wachstumsraten $n(k)$ ihrer Amplituden gilt auch für binäre granulare Systeme. Unsere Ergebnisse zeigen, dass Reibung zwischen den Teilchen eine wesentliche Voraussetzung für das Auftreten der RT-Instabilität in granularen Medien ist. In Abwesenheit von Teilchenreibung ähnelt die Grenzflächeninstabilität mehr der Richtmyer-Meshkov-Instabilität. Wir definieren außerdem ein Fließkriterium Y, indem wir das granulare Medium als viskoplastisches Material behandeln; nur für $Y > 15$ treten Fingerinstabilitäten auf. Interessanterweise haben frühere Arbeiten gezeigt, dass Instabilitäten im unteren Erdmantel, ebenfalls ein viskoplastisches Material, auch bei ähnlichen Werten von Y auftreten.

ACKNOWLEDGEMENTS

I would like to express my deepest gratitude to my supervisor, Prof. Christoph Müller, for guiding me through the challenging but interesting research topics in granular systems. His interest in the modelling of segregation in granular materials readily fascinated me. I greatly appreciate his support, guidance, and patience to allow me to learn and stumble ahead during my academic training, not to mention his tireless mentoring to refine my scientific writings. The accomplishments of this thesis were simply not possible without his help.

I am also thankful to LESElab members and other researchers I have met at ETH Zürich creating such a diverse and dynamic academic environment: Qasim, Sena, Andac, Davood, Sung Min, Sergey, Aga, Alex, Alexey, Hui, Manouchehr, Athanasia, Petro, Nora, Yi-Hsuan, Margarita, Giancarlo, Guillaume, Annelies, Maximilian, Evegenia, Marcel, Zixuan, Angelo, David, Matthias, Fei, Elena, Denis, Felix, Alexander, Paula, Alexey, Jian, Mo, Yongqing, Boyuan. Particularly, special thanks must go to my colleagues Ali, Laure and Chris for introducing me to the efficient simulation techniques and preventing me from reinventing the wheel, Nicki, Jens for discussing scientific problems regularly and reading manuscripts, Alexander for introducing me to the MRI setup; Chris for sharing his experimental data and results about the granular Rayleigh-Taylor instability, Guang and Yong for helping me to adapt to the new environment and extensive discussions on a variety topics; Mehrdad, Louis, Fabian and Yannik for bringing some new thoughts, Cristina for managing the administrative tasks. I would also like to thank the good friends I have made, i.e., Ally, Junyi, Jingting Shuqin, Shaopu, Shengqiang, Rui, Meijun, Gang, Yanyan, Bing, Yuanhao, Pu, Yatao, Yafu, Yukai, Chi, Daxin, Lan, Shuo, Ze, Xi, Caifa, Junxiao, Teng, Yafei, Tianyuan, Shiyu, Gengyun, Xiaorong, Qiao. Thank you for the wonderful time we have spent together.

I thank Prof. Dr. Alexander Penn and Prof. Dr. Fernando Hernández Jiménez for accepting to review my dissertation.

I also want to thank Prof. Dawei Tang, Prof. Shi Liu, Prof. Xiaoze Du, Prof. Xinghua Zheng, for their recommendations, as well as the funding of the Chinese Scholarship Council and the Swiss National Science Foundation, allowing me to take the challenge to conduct doctoral research abroad.

Finally, there are no words to stress enough my sincere gratitude to my family for their unconditional support during the past years. I thank my wife Noemy, who always supported me and cared for me in good and bad times. Thank you for giving me such an amazing family and for making my ordinary days extraordinary.

CONTENT

1 INTRODUCTION

Granular media are widely encountered in both nature and industry. Indeed, today granular materials are the second-most used material in industrial processes (de Gennes 1999). Typical processing reactors include fluidized or packed beds, rotating cylinders or hoppers. Besides their industrial relevance rich and complex granular phenomena are observed in nature, such as the motion of sand dunes, rockslides, snow avalanches or galaxy formation. Hence, due to their importance in industry and in the prevention of natural disasters, granular media have attracted significant interest by mathematicians, physicists and engineers aiming to obtain a better understanding of their physics allowing in turn for a more accurate prediction of their behavior.

Although there is some practical understanding of the behavior of granular materials, largely through empiricism, the detailed, underlying physics are still elusive. For example, it is already difficult to classify the state of granular media as it can possess both solid, liquid or gas like properties. An example, where granular material can possess both solid, liquid and gas-like properties, is the pouring of beads onto a pile as shown in Figure 1.1 (Forterre and Pouliquen 2008). Currently, we have no unified theoretical framework to describe a system such as the one shown in Figure 1.1 with a continuum description (Seife 2005). Nevertheless, there has been progress in developing physical models for specific granular systems such as Heckel's law (Heckel 1961), the Jannssen model (Sperl 2006; Janssen 1895), the kinetic theory for granular gases (Haff 1983; Kumaran 2008; Goldhirsch 1999; Ogawa 1978; Savage and Jeffrey 1981; Lun et al. 1984) or local and non-local rheology models (MiDi 2004; Forterre and Pouliquen 2008; da Cruz et al. 2005; Jop, Forterre, and Pouliquen 2006) (Aranson and Tsimring 2001; Bouzid et al. 2013; Derec, Ajdari, and Lequeux 2001; Kamrin and Koval 2012; Pouliquen and Forterre 2009) that capture successfully phenomena such as creeping flow below the yield criterion (Komatsu et al. 2001).

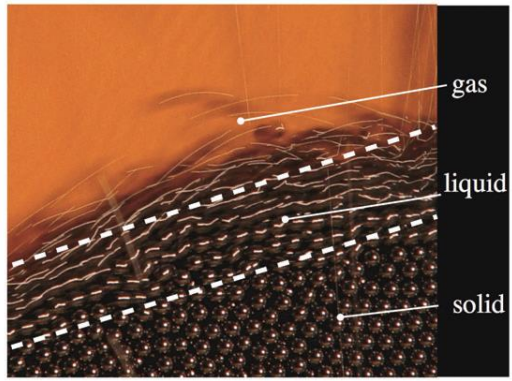

FIG. 1.1 Co-existence of different states in a granular system when pouring beads onto a pile (Forterre and Pouliquen 2008).

The theoretical complexity of granular materials arises from the fact that some "pre-conditions" of classical gases and fluids are not met, such that molecules are very small and elastic as contacts between two granules are dissipative and friction occurs. Furthermore, granular systems are far away from equilibrium and also thermal considerations are often not appropriate as the term $k_B T$ at room temperature is by a factor of 10^{12} lower than the potential energy of a typical sand particle (Jaeger, Nagel, and Behringer 1996). The negligible effect of $k_B T$ also implies that traditional entropy considerations may not be applicable in dynamic granular systems.

Edwards aimed to resolve the limitations of traditional entropy considerations to describe static granular systems (Edwards and Oakeshott 1989; Mehta and Edwards 1990). Instead of internal energy, the volume V is used as the key variable to characterize the macrostate of a static granular assembly. A temperature-like quantity called 'compactivity' is then defined as $X = \partial V / \partial S$, where S is the entropy of the granular system, given by $S(V) = k_E \ln \Omega(V)$, where k_E is a 'Boltzmann-like' constant ($k_E = 1$) and $\Omega(V)$ is the number of possible particle configurations in a given volume V. Edwards's theory relies on two key conjectures analogous to classic thermodynamics, i.e. ergodicity and equi-probability of the microstates, i.e. "*We assume that when N grains occupy a volume V they do so in such a way that all configurations are equally weighted.*" (Edwards 1994). Although it is challenging to justify these conjectures from

first principles, there is evidence that the configurations of a packing are equally probable at the point of unjamming (Martiniani et al. 2017; Baule et al. 2018; Martiniani 2017; Asenjo, Paillusson, and Frenkel 2014; Xu, Frenkel, and Liu 2011). There have been some successful applications of Edward's theory such as quantifying ensemble averaged quantities e.g. the solid fraction at the jamming point (ϕ=0.64) of a random close packing (RCP) (Song et al. 2010), the phase diagram of jammed granular matter (relation between coordinate number and solid fraction) (Song, Wang, and Makse 2008) and the description of a granular system at rest with an equation of state (Ciamarra, Coniglio, and Nicodemi 2006). However, it is worth noting that Edward's theory has been mostly used to predict structural properties (such as solid fraction and coordinate number) and it remains largely unexplored whether it is also capable to describe well the dynamics of granular media. In this regard, there have been efforts by Herrmann to formulate a thermodynamic framework for granular flow (Herrmann 1993). Here, a local steady state that maintained by an energy flux is used as the analog for a local "equilibrium". This framework has been applied to the Brazil nut phenomenon (BNP) (Trujillo and Herrmann 2003). The BNP describes the observation that large intruders rise in a vibrated granular system. Very recently, the theory of Herrmann (Trujillo and Herrmann 2003) was extended to a dense granular shear flow (Liu and Müller 2021). It was found that in such a system an intruder in the size ratio $1 < d_I/d_p < 4$ rises due to variations in the local pressure (i.e. the intruder reduces the local granular pressure). For intruders with $d_I/d_p > 4$, the local pressure disturbance is very small as the system approaches a continuum limit, in which the pressure acting on the intruder equals to the hydrostatic pressure. At the same time the presence of an intruder leads to a cooling effect, i.e. the intruder flattens the local shear rate thus reducing the local granular temperature. This cooling effect increases with intruder size, leading ultimately to the sinking of large intruders. Although, the idea of a thermodynamic model for granular flow has been around for more than three decades we still lack key relationships such as the link between granular pressure and granular temperature, although some progress has been made recently (Kim and Kamrin 2020; Taylor and Brodsky 2017).

Another challenge that is encountered when aiming to formulate a continuum description for granular materials is the absence of scale separation between the particle and system size. As a consequence, properties arising from

ensemble averaging become resolution dependent, i.e., variables such as granular pressure or temperature cannot be assigned directly to a single point in the system. For example, the granular temperature, which is an analogue to the thermodynamic temperature and which is defined as the mean square of the random velocity fluctuation about the mean velocity in a granular flow grows quadratically with the size of the coarse graining volume in dense granular shear flows (Glasser and Goldhirsch 2001; Liu and Müller 2021). This resolution-dependent behaviour is because the changes in velocity over the mean free path $\dot{\gamma}l$ are relatively large compared to the thermal speed $\sqrt{T}$ (here $\dot{\gamma}$ is the shear rate, l is the mean-free path and T is the granular temperature). For example, assuming air at 300 K, 1 atm with a constant shear rate of $\dot{\gamma}=10$ 1/s, a free mean path of $l \sim O(10^{-8}\,\mathrm{m})$, and $T \sim O(10^{4}\,\mathrm{m}^2/\mathrm{s}^2)$, we obtain $\dot{\gamma}l/\sqrt{T} \sim O(10^{-9})$, i.e., the thermal motion is relative large making the properties of air only weakly resolution dependent. However, for granular media using the equation of state $T=C\dot{\gamma}^2 l^2/(1-e^2)$ (Tan and Goldhirsch 1998), where e is the coefficient of restitution, $\dot{\gamma}l/\sqrt{T} \sim \sqrt{(1-e^2)} \sim O(1)$, suggesting that there is no clear scale separation between the macroscopic velocity ($\dot{\gamma}l$) and the microscopic thermal speed $\sqrt{T}$ of the particles unless the particles are approaching perfect elasticity $e \longrightarrow 1$ (Glasser and Goldhirsch 2001). Besides the granular temperature, also the granular pressure/stress have been reported to be resolution-dependent (Weinhart et al. 2013), yet there is evidence that the granular stress/pressure reaches a plateau for a coarse graining radius of $w > d_p$, where d_p is the average particle diameter. Hence, in granular materials the resolution needs to be specified when measuring the value of a variable computationally or experimentally.

Owing to their complexity granular systems can feature many intriguing phenomena, such as radial and axial segregation (Shinbrot and Muzzio 2000), clustering (Olafsen and Urbach 1998), Taylor vortices (Conway, Shinbrot, and Glasser 2004) or fingering (McLaren et al. 2019). Such phenomena can serve as a test-ground for the theoretical modelling of granular materials (Ottino 2006), allowing to identify both the merits and drawbacks of specific models. It is worth noting, that the task to describe granular materials becomes even more complex when dealing with non-spherical particles. Particle shape can have a remarkable influence on e.g. the morphology of a packing (Lu et al. 2016; Conzelmann et al. 2020) or flow dynamics (Müller et al. 2015; Langston

et al. 2004; Sinnott and Cleary 2009; Pereira et al. 2011; Hilton and Cleary 2011). For more details concerning the modelling and application of non-spherical particles the interested reader is referred to specific reviews, e.g. by Lu, Third, and Muller (2015).

While we have focused above largely on modelling aspects of granular materials it is worth noting a few words on experimental techniques to probe the physics of granular matter. As granular materials are visually opaque, traditional optical techniques are often of little use unless the interrogation is limited to the surface of the walls or 2D granular systems. However, over the years, several non-intrusive measurement techniques have been introduced including magnetic resonance imaging (MRI) (Müller et al. 2006; Nakagawa et al. 1993; Penn et al. 2017), X-ray tomography (Seidler et al. 2000) or positron emission particle tracking (PEPT) (Parker et al. 2008). More details about the specific experimental techniques, their advantages and disadvantages can be found in excellent reviews, e.g. (Amon et al. 2017; Stannarius 2017). Generally, and independent of the specific experimental technique it is difficult to obtain experimentally microscopic information (in particular temporally resolved). In this regard, (validated) numerical modelling approaches such as the discrete element method (DEM) (Tsuji, Kawaguchi, and Tanaka 1993; Cundall and Strack 1979) are very attractive and have been used to reproduce a series of granular phenomena such as BNP (Metzger, Remy, and Glasser 2011) or bubbling in fluidized beds (Müller et al. 2008) .

1.2 Outline of thesis

In this doctoral thesis we explore different phenomena in granular media including segregation in both vibrating beds and dense shear flows and a Rayleigh-Taylor-like instability in binary granular materials. The phenomena are studied by numerical modelling approaches such as the discrete element method (DEM) and DEM coupled with computational fluid dynamics (CFD). The structure of the thesis is as follows:

Chapter 2 introduces the discrete element method (DEM) which is used to simulate the granular systems studied here, i.e., inclined granular shear flow, vibrated and fluidized beds.

Chapter 3 introduces the coarse graining (CG) method to map information from the discrete to the continuum level.

Chapter 4 critically assesses the validity of a granular buoyancy model based on a generalized Archimedean formulation of buoyancy. By simulating a convection-free vibrated system (by turning off wall-particle friction), the generalized Archimedean formulation is compared to the buoyancy force measured via a virtual spring or from its hydrostatic definition (pressure gradient). We demonstrate that the buoyancy force obtained though the three different approaches agrees very well, validating the generalization of its Archimedean formulation. Next, convection is introduced to the system. Hence, the lift force is composed of the granular buoyancy force and a drag force. It was shown that using a drag model for the slow velocity regime, the lift force could be predicted accurately though the proposed generalized Archimedean formulation of the buoyancy force. We rationalize the dependence of the lift force on the density of the bed particles and the intruder diameter, and the independence of the lift force on the intruder density and the vibration strength (once exceeding a critical value).

Chapter 5 develops a new lift force model to describe the motion of intruders in dense, granular shear flow. The derivation is an extension of a thermal buoyancy model of Trujillo and Hermann (2003) but takes into account both granular pressure and temperature differences. The model is further extended by considering the density differences between the intruder and the bed particles. The model predicts very well the lift force acting on the intruder and the neutral buoyancy limit of intruders in shear flows. It is shown that the presence of an intruder leads to a cooling effect and a local flattening of the shear velocity profile (lower shear rate). The cooling effect increases with intruder size and explains the sinking of large intruders. On the other hand, the introduction of small to mid-sized intruders, i.e., up to 4 times the bed particle size, leads to a reduction in the granular pressure compared to the hydrostatic pressure, which in turn explains the rising of small to mid-sized intruders.

Chapter 6 explores a newly discovered Rayleigh-Taylor (RT)-like fingering instability in binary granular media. Fingering instabilities akin to the RT instability in fluids have been observed in a binary granular system in which dense and small particles are layered on top of lighter and larger particles, when the system is subjected to vertical vibration and fluidizing gas flow. Using observations from experiments and numerical modelling we explore whether the theory developed to describe the RT instability in fluids is also applicable to binary granular systems. Our results confirm the applicability of multiple key properties of the RT instability theory for binary granular systems. Furthermore, we demonstrate that inter-particle friction is essential for the RT instability to occur in granular media. For zero particle friction the interface instability bears a greater resemblance to the Richtmyer-Meshkov instability. We further define a yield criterion Y for the interface; only for $Y > 15$ fingering occurs.

Finally, Chapter 7 summarizes the conclusion of the thesis, while Chapter 7 proposed some future work.

The discrete element method for the modelling of granular material was originally proposed by Cundall and Strack (1979) and treats each particle as a single entity. The dynamics of each particle are governed by Newton's law of motion:

$$m_i \frac{d\mathbf{u}_{pi}}{dt} = \mathbf{f}_{ti} + \mathbf{f}_{fpi} + m_i \mathbf{g}\,, \tag{2.1}$$

$$I_i \frac{d\mathbf{w}_i}{dt} = \mathbf{T}_i\,, \tag{2.2}$$

where m_i, $\mathbf{u}_{pi}$, $\mathbf{w}_i$, I_i are the mass, velocity, angular velocity and momentum of inertia of particle i, respectively, and $\mathbf{f}_{ti}$, $\mathbf{f}_{fpi}$ $\mathbf{T}_i$ and $\mathbf{g}$ are the particle-particle contact force, the fluid-particle force, the torque and the acceleration due to gravity, respectively.

In our work, the contact forces acting between particles, $\mathbf{f}_{ti}$, are modelled by a soft sphere approach.

2.1 Contact model

Contacting particles lead to small deformations at the area of contact. Numerically, the deformation is simplified by an overlap between contacting particles. The overlap is denoted by δ. The resulting contact force is expressed as a function of the deformation, typically through a spring-dash model. The most widely applied contact model is the linear spring –dashpot (LSD) model.

The LSD model is given by the following equation,

$$\ddot{\delta} + 2\gamma\dot{\delta} + \omega_0^2\delta = 0\,, \tag{2.3}$$

where δ is the overlap, given by $\delta = \max(0, r_i+r_j-d)$ with r_i and r_j being the radii of particle i and j and d is the distance between their centers of gravity, m is the effective mass given by $m = m_i m_j/(m_i+m_j)$, γ is the damping coefficient and k is the spring constant, defined as $k = \omega_0^2 m$, where ω_0 is the frequency of the undamped harmonic oscillator.

In the LSD model, the damping coefficient γ is determined by

$$\gamma = \frac{-\ln e}{\sqrt{\ln^2 e + \pi^2}} \sqrt{k/m}\,, \tag{2.4}$$

where e is the coefficient of restitution. In Eq. 2.4 the coefficient of restitution is considered to be independent of the impact velocity, which is a reasonable simplification for low impact velocities.

An alternative to the LSD is the Hertzian spring-dashpot (HSD) model, which is given by,

$$\ddot{\delta} + \alpha(e)\Omega_0 \delta^{1/4}\dot{\delta} + \Omega_0{}^2 \delta^{3/2} = 0\,, \tag{2.5}$$

where $\Omega_0 = (K/m)^{1/2}$.

The contact force arising from the collision of two particles in the HSD is:

$$F_{\text{Hertz}} = K\delta^{3/2} = \frac{4E_{eff}\sqrt{r_{eff}}}{3}\delta^{3/2}\,, \tag{2.6}$$

where E_{eff} is the effective Young's modulus, i.e. $E_{\text{eff}} = 1/((1-\nu_i^2)/E_i+(1-\nu_j^2)/E_j)$ with E_i, E_j and ν_i, ν_j being the Young's moduli and Poisson's ratios of particle i and particle j, respectively and r_{eff} is the effective radius, defined as $r_{\text{eff}} = r_i r_j/(r_i+r_j)$.

Since $\ddot{\delta} = u(\mathrm{d}u/\mathrm{d}\delta)$ and using $\delta(t) = Ax^n$, Eq. (2.5) can be converted into a similar form as Eq. (2.3) by setting $A = (5/4)^{5/2}$ and $n = 4/5$ (Antypov and Elliott 2011), viz.

$$u\frac{\mathrm{d}u}{\mathrm{d}x} + \frac{2}{\sqrt{5}}a(e)\Omega_0 v + {\Omega_0}^2 x = 0\,. \tag{2.7}$$

Considering that $k = 8/3E_{\mathrm{eff}}r_{\mathrm{eff}}$ and $K = 4/3E_{\mathrm{eff}}{r_{\mathrm{eff}}}^{1/2}$ and ensuring that the dissipation term of the HSD model (Eq. 2.7) is equal to that in the LSD model (Eq. 2.3), i.e., $2\gamma = (2/5^{1/2})\alpha(e)\Omega_0$, K_n and $\alpha(e)$ are required to be (Antypov and Elliott 2011):

$$K_n = k_n(4r_{eff})^{-0.5}, \tag{2.8}$$

$$\alpha(e) = \frac{-\sqrt{5}\ln e}{\sqrt{\ln^2 e + \pi^2}}\,. \tag{2.9}$$

The normal contact force F_n in the LSD and HSD model are then given by:

$$LSD: \quad F_{L,n} = -k_n\delta_n + 2\gamma_n m_{eff}^{1/2}\dot{\delta}_n\,, \tag{2.10}$$

$$HSD: \quad F_{H,n} = -K_n\delta_n^{3/2} + 2\frac{\sqrt{5}}{5}\gamma_n m_{eff}^{1/2}\left(\frac{\delta_n}{4r_{eff}}\right)^{1/4}\dot{\delta}_n\,. \tag{2.11}$$

while the contact forces in the tangential direction F_t are given by:

$$LSD: \quad F_{L,t} = -k_t\delta_t + 2\gamma_t m_{eff}^{1/2}\dot{\delta}_t\,, \tag{2.12}$$

$$HSD: \quad F_{H,t} = -K_t\delta_n^{1/2}\delta_t + 2\frac{\sqrt{5}}{5}\gamma_t m_{eff}^{1/2}\left(\frac{\delta_t}{4r_{eff}}\right)^{1/4}\dot{\delta}_t\,. \tag{2.13}$$

Here, k_t and K_t are the spring stiffness in the tangential direction, γ_t is the damping coefficient in the tangential direction and δ_t is the overlap in the tangential direction. For a Hertzian contact, the relationship between the contact stiffness in the normal and tangential direction is given by Mindlin's theory, i.e. K_t/K_n is ~ 2/3 for most materials. The tangential contact force is limited by Coulomb's law,

$$F_t \leq \mu F_n, \tag{2.14}$$

where μ is the coefficient of friction. To ensure numerical stability, the time step is typically smaller than $2\pi(m/k_n)^{0.5}/10$.

In the following we model a dense shear flow system (Figure 2.2) using both the LSD and HSD models and compare the results with literature data (Silbert et al. 2001; Weinhart et al. 2013) The complete list of the model parameters is given in Table 2.1.

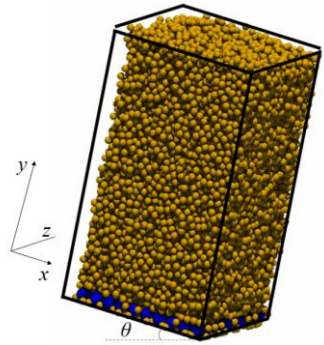

FIG. 2.2 Setup for the inclined shear flow modelled. The yellow colour denotes bed particles and the blue particles denote glued wall particles. Periodic boundary conditions are applied in the x and z directions.

Table 2.1 Parameters used in the simulations

LSD	k_n (N/m)	k_t (N/m)	γ_n (kg$^{1/2}$/s)	γ_t (kg$^{1/2}$/s)	μ	e
	6.41×10^4	$2/7k_n$	62.74	0	0.50	0.88
HSD	K_n (N/m$^{3/2}$)	K_t (N/m$^{3/2}$)	γ_n (kg$^{1/2}$/s)	γ_t (kg$^{1/2}$/s)	μ	e
	1.83×10^7	$2/7K_n$	20.59	0	0.50	0.88

The simulation setup is identical to the system modelled by Silbert et al. 2001. Here, monodispersed particles of diameter d and mass m are placed on an inclined plane (xy) with a tilt angle θ. The bottom of the inclined plane is composed of fixed particles to ensure a rough bottom wall which is critical to stabilize the shear flow. Periodic boundary conditions are applied in the x (flow) and y directions to develop a steady flow down an infinitely long and wide chute. The dimensions of the system are $L_x = 20d$, $L_y = 20d$ and $H = 40d$. The size of the glued particles at the bottom wall is $d_w = 2d$. We focus on comparing the velocity profile as a function of the contact model, as further macroscopic quantities such as the solid fraction and stress are not varying substantially with variation in the contact model (Silbert et al. 2001). We used the open source code LIGGGHTS (Kloss et al. 2012).

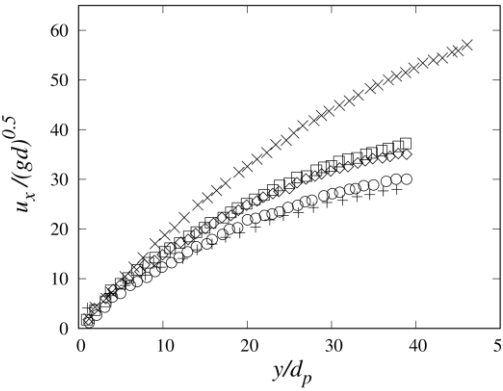

FIG. 2.3 Velocity profile in a dense shear flow along an inclined plane (θ = 26°) using different contact models: (+) LSD data from (Silbert et al. 2001)

(○) LSD data from our work; (×) HSD model from (Silbert et al. 2001). (□) HSD data from our work; (◇) HSD data from di Renzo et al. 2004.

Figure 2.3 plots the velocity profiles of a dense shear flow obtained from numerical simulations using different contact models. There is a good agreement between the LSD model in our simulation and the LSD results of Silbert et al. (2001). However, there are significant differences in the predictions when using a LSD model compared to a HSD model. However, further macroscopic quantities such as the solid fraction or the stress profile do no vary appreciably when using different contact models, which is in agreement with previous reports (Silbert et al. 2001; Weinhart et al. 2013).

2.2 CFD-DEM coupling

To model gas-solid systems we couple DEM to computational fluid dynamics (CFD). Assuming an incompressible fluid phase, the following simplified governing equations hold

$$\frac{\partial}{\partial t}(\varepsilon_f)+\nabla\cdot(\varepsilon_f \mathbf{u}_f)=0\,, \tag{2.15}$$

$$\frac{\partial}{\partial t}(\varepsilon_f \varrho_f \mathbf{u}_f)+\nabla\cdot(\varepsilon_f \rho_f \mathbf{u}_f \mathbf{u}_f)=-\nabla p+\nabla\cdot(\varepsilon_f \tau_f)+\varepsilon_f \varrho_f \mathbf{g}-\mathbf{F}_{fp}\,, \tag{2.16}$$

where ε_f, ρ_f, u_f, τ_f is the void fraction, fluid density, fluid velocity and the fluid viscous stress, respectively. The interaction between the particles and the fluid phase is given via:

$$\mathrm{F}_{fp}=\sum_{i=1}^{m_{ci}}\frac{1}{V_{mc}}\mathbf{f}_{fpi}\,, \tag{2.17}$$

where m_c is the index of the mesh cell; m_{ci} is the index of particle i in the mesh cell of index m_c and V_{mc} is the volume of mesh cell. The force between the fluid and particle i in the mesh cell is given by $\mathbf{f}_{fpi} = -V_{pi}\nabla p + V_{pi}\nabla\cdot\boldsymbol{\tau}_f + \varepsilon_f\mathbf{f}_{di}$, where $\varepsilon_f\mathbf{f}_{di}$ is the fluid drag acting on particle i.

Assuming incompressible fluids, the conservation of mass is simplified to:

$$\nabla\cdot(\varepsilon_f\mathbf{u}_f + \varepsilon_s\mathbf{u}_s) = 0, \tag{2.18}$$

where $\mathbf{u}_s$ is the velocity of the particle phase and ε_s is the volume fraction of the particle phase (with $\varepsilon_s + \varepsilon_f = 1$). Substituting Eq. (2.17), (2.18) into the momentum conservation equation, Eq. (2.16), we obtain:

$$\frac{\partial}{\partial t}(\varepsilon_f\rho_f\mathbf{u}_f) + \nabla\cdot(\varepsilon_f\rho_f\mathbf{u}_f\mathbf{u}_f) = -\varepsilon_f\nabla p + \varepsilon_f\mu_f\nabla^2\mathbf{u}_f - \varepsilon_f\sum_{i=1}^{cn} f_{di}/V_c + \varepsilon_f\rho_f\mathbf{g} \tag{2.19}$$

In this work the drag correlation of Koch-Hill (Koch and Hill 2001) is used. Generally, the drag force term, f_{di}, can be expressed as:

$$\mathbf{f}_{di} = \frac{V_{pi}}{\varepsilon_s}\beta_i(\mathbf{u}_{pi} - \mathbf{u}_{fi}), \tag{2.20}$$

where V_{pi} is the particle volume, $\mathbf{u}_{pi}$ is the particle velocity and $\mathbf{u}_{fi}$ is the fluid velocity at the location of particle i; The correlation coefficient β_i is given by (Koch and Hill 2001) as:

$$\beta_i = \frac{18\mu_f\varepsilon_f{}^2\varepsilon_s}{d_p^2}\left(F_0(\varepsilon_s) + \frac{1}{2}F_3(\varepsilon_s)Re_p\right), \tag{2.21}$$

where Re_p is the particle-based Reynolds number, defined as:

$$Re_p = \frac{\varepsilon_f \rho_f \left| u_{pi} - u_{fi} \right| d_{pi}}{\eta}. \tag{2.22}$$

The functions $F_0(\varepsilon_s)$ and $F_3(\varepsilon_s)$ in Eq. (2.21) are given by:

$$F_0(\varepsilon_s) = \begin{cases} \dfrac{1 + 3\sqrt{\dfrac{\varepsilon_s}{2}} + \dfrac{135}{64}\varepsilon_s \ln(\varepsilon_s) + 16.14\varepsilon_s}{1 + 0.681\varepsilon_s - 8.48\varepsilon_s^2 + 8.16\varepsilon_s^3} & if\ \varepsilon_s < 0.4, \\ \dfrac{10\varepsilon_s}{\varepsilon_f^3} & if\ \ \varepsilon_s \geq 0.4 \end{cases} \tag{2.23}$$

$$F_3(\varepsilon_s) = 0.0673 + 0.212\varepsilon_s + \frac{0.232}{\varepsilon_f^2}. \tag{2.24}$$

The locally-average Navier-Stokes equations, Eq. (2.18) and Eq. (2.19), are solved using the open source solver OpenFOAM (Rusche 2003) while the governing equations for the particle motion, Eq. (2.1) and Eq. (2.2) are solved by LIGGGHTS (LAMMPS improved for general granular and granular heat transfer simulations). The coupling between the fluid and particle phases is performed via the CFDEM®*Coupling* solver (Goniva et al. 2012).

The raw data obtained from DEM simulations provide information on the particle level, such as particle position, velocity and acceleration. For several applications it is necessary to map information from the discrete to the continuum level. This is achieved through coarse graining (CG) and several CG techniques have been developed to obtain continuum data from discrete data (Luding and Alonso-Marroquín 2011; Babic 1997). In this thesis, we use the CG method that has been developed by Goldhirsch 2010.

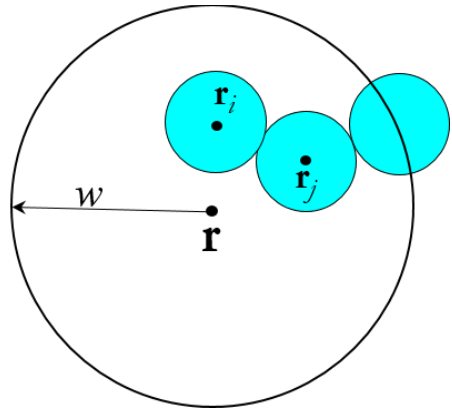

FIG. 3.1. Illustration of a CG volume located at **r**.

In the following the CG method applied here is described in more detail. Let us consider a coarse graining (CG) volume located at **r** with a radius w (Figure 3.1). The CG density at point **r** at time t is given as:

$$\varrho(\mathbf{r},t) = \sum_{i=1}^{N} m_i G(\mathbf{r} - \mathbf{r}_i(t)) \,, \tag{3.1}$$

where $G(\mathbf{r}-\mathbf{r}_i(t))$ is the CG function, e.g., the Heaviside or Gaussian function.

Similarly, the momentum density is defined as:

$$\varrho(\mathbf{r},t)\mathbf{u}(\mathbf{r},t)=\sum_{i=1}^{N} m_i G(\mathbf{r}-\mathbf{r}_i(t))\cdot\mathbf{u}(\mathbf{r}_i,t) \tag{3.2}$$

where **u**(**r**,t) is the CG velocity that is obtained by averaging the velocities of all particles that are located within the CG volume. Combing Eq. (3.2) and (3.1), the CG velocity is obtained as:

$$\mathbf{u}(\mathbf{r},t)=\sum_{i=1}^{N} m_i G(\mathbf{r}-\mathbf{r}_i(t))\cdot\mathbf{u}(\mathbf{r}_i,t)\,/\sum_{i=1}^{N} m_i G(\mathbf{r}-\mathbf{r}_i(t))\,. \tag{3.3}$$

To obtain the CG stresses, we start with the momentum conservation equation, viz:

$$\underbrace{\frac{\partial \varrho u_\alpha(\mathbf{r},t)}{\partial t}}_{A}+\underbrace{\frac{\partial \varrho u_\alpha(\mathbf{r},t)u_\beta(\mathbf{r},t)}{\partial x_\beta}}_{B}=\frac{\partial \sigma_{\alpha\beta}}{\partial x_\beta}+\varrho g_\alpha\,. \tag{3.4}$$

where α and β denote the Cartesian coordinates x, y, z, $\sigma_{\alpha\beta}$ is the stress and g_α is the component of the gravity vector along α. Substituting Eq. (3.2) into the term A in Eq. (3.4) we obtain:

$$A=\underbrace{\sum_{i=1}^{N} m_i G(r-r_i(t))\frac{du_\alpha^i(t)}{dt}}_{C}-\underbrace{\sum_{i=1}^{N} m_i u_\alpha^i(t)u_\beta^i(t)\frac{\partial G(r-r_i(t))}{\partial x_\beta}}_{D}\,. \tag{3.5}$$

allowing us to write the stress containing term as:

$$\frac{\partial \sigma_{\alpha\beta}}{\partial x_\beta}=(C-\rho\mathbf{g}_\alpha)+B+D\,. \tag{3.6}$$

Newton's law of motion gives us

$$m_i \frac{du_\alpha^i}{dt} = m\mathbf{g}_\alpha + \sum_j f_\alpha^{ij}(t), \tag{3.7}$$

and substituting Eq. (3.7) into the first term of Eq. (3.6) yields:

$$C - \rho\mathbf{g}_\alpha = \sum_j f_\alpha^{i,j}(t) G(\mathbf{r} - \mathbf{r}_i(t)). \tag{3.8}$$

Furthermore, the force acting from particle *i* to particle *j* is equal (but acting in the opposite direction) to the force acting from particle *j* to particle *i*, i.e.

$$\sum_j f_\alpha^{i,j}(t) G(\mathbf{r} - \mathbf{r}_i(t)) = -\sum_j f_\alpha^{j,i}(t) G(\mathbf{r} - \mathbf{r}_j(t)). \tag{3.9}$$

Therefore, Eq. (3.8) can be modified yielding:

$$\begin{aligned} C - \rho\mathbf{g}_\alpha &= -\frac{1}{2}\sum_{i,j} f_\alpha^{i,j}(t)\left(G(\mathbf{r} - \mathbf{r}_i(t)) - G(\mathbf{r} - \mathbf{r}_j(t))\right) \\ &= -\frac{1}{2}\sum_{i,j} f_\alpha^{i,j}(t) \int_{s=0}^{1} ds \frac{\partial}{\partial s}\left(G(\mathbf{r} - \mathbf{r}_j(t) + s\mathbf{r}_{ij}(t)\right) \end{aligned}, \tag{3.10}$$

where $\mathbf{r}_{ij}$ is a vector pointing from $\mathbf{r}_i$ to $\mathbf{r}_j$, as illustrated in Figure 3.1. Applying the chain rule we obtain

$$\frac{\partial}{\partial s} G\left(\mathbf{r} - \mathbf{r}_j(t) + s\mathbf{r}_{ij}(t)\right) = r_\beta^{j,j} \frac{\partial}{\partial x_\beta} G\left(\mathbf{r} - \mathbf{r}_j(t) + s\mathbf{r}_{ij}(t)\right), \tag{3.11}$$

and substituting Eq. (3.11) into Eq. (3.10), we obtain

$$C - \rho\mathbf{g}_\alpha = -\frac{1}{2}\sum_{i,j} f_\alpha^{i,j}(t) r_\beta^{i,j} \int_0^1 ds \frac{\partial}{\partial x_\beta}\left(G(\mathbf{r} - \mathbf{r}_j(t) + s\mathbf{r}_{ij}(t)\right). \tag{3.12}$$

Further, the summation of terms *B* and *D* in Eq. (3.6) gives:

$$B+D=\frac{\partial \varrho u_\alpha(\mathbf{r},t)u_\beta(\mathbf{r},t)}{\partial x_\beta}-\sum_i m_i u_\alpha^i(t)u_\beta^i(t)\frac{\partial G(r-r_i(t))}{\partial x_\beta}$$

$$=\frac{\partial}{\partial x_\beta}\left[\begin{array}{l}\sum_i m_i u_\alpha(\mathbf{r},t)u_\beta(\mathbf{r},t)G(\mathbf{r}-\mathbf{r}_i(t))-\\ \sum_i m_i u_\alpha^i(t)u_\beta^i(t)G(\mathbf{r}-\mathbf{r}_i(t))\end{array}\right]. \tag{3.13}$$

Substituting the fluctuation of the velocity of particle *i* with respect to the CG velocity, i.e. $u_\alpha^{i'}(t)=u_\alpha^i(t)-u_\alpha(\mathrm{r},t)$ into Eq. (3.13) allows to simply Eq. (3.13) yielding:

$$B+D=\frac{\partial}{\partial x_\beta}\left(-\sum_i m_i u_\alpha^{i'}(t)u_\beta^{i'}(t)G(\mathbf{r}-\mathbf{r}_i(t))\right). \tag{3.14}$$

If we now substitute Eq. (3.14) and Eq. (3.12) into Eq. (3.6) we obtain:

$$\frac{\partial \sigma_{\alpha\beta}}{\partial x_\beta}=\frac{\partial}{\partial x_\beta}\left[\begin{array}{l}-\frac{1}{2}\sum_{i,j} f_\alpha^{i,j}(t)r_\beta^{i,j}\int_0^1 ds\left(G(\mathbf{r}-\mathbf{r}_j(t)+s\mathbf{r}_{ij}(t)\right)-\\ \sum_i m_i u_\alpha^{i'}(t)u_\beta^{i'}(t)G(\mathbf{r}-\mathbf{r}_i(t))\end{array}\right]. \tag{3.15}$$

Hence, the CG stress is given,

$$\sigma_{\alpha\beta}(\mathbf{r},t) = \overbrace{-\frac{1}{2}\sum_{i,j} f_\alpha^{i,j}(t) r_\beta^{i,j} \int_0^1 ds\left(G(\mathbf{r}-\mathbf{r}_j(t)+s\mathbf{r}_{ij}(t)\right)}^{\sigma_{\alpha\beta}^c} \underbrace{-\sum_i m_i u_\alpha^{i'}(t) u_\beta^{i'}(t) G(\mathbf{r}-\mathbf{r}_i(t))}_{\sigma_{\alpha\beta}^k} \quad . \tag{3.16}$$

The first term of the right-hand side (RHS) of Eq. (3.16) is called the contact stress, $\sigma_{\alpha\beta}^{c}$, which accounts for contributions due to inter-particle contact forces. The second term of the RHS is called the kinetic stress, $\sigma_{\alpha\beta}^{k}$, which originates from fluctuation in the particle velocities.

Using now a given CG function $G(\mathbf{r}-\mathbf{r}_i(t))$, the CG stress can be calculated via Eq. (3.16). Several types of CG functions are routinely used, such as the Heaviside function or the Gaussian function, i.e.:

$$\text{Heaviside function: } G(\mathbf{r}) = \frac{1}{V} H(w_c - |\mathbf{r}|) = \begin{cases} 1/V & \text{,if } |\mathbf{r}| \le w_c \\ 0 & \text{,if } |\mathbf{r}| > w_c \end{cases} \tag{3.17}$$

$$\text{Gaussian function: } G(\mathbf{r}) = \frac{1}{\Theta(w_c)} e^{-(\|\mathbf{r}\|/w_c)^2} \tag{3.18}$$

The integral of the CG function $G(\mathbf{r}-\mathbf{r}_i(t))$ has to fulfil $\int_{R^3} G(r)dr = 1$. This condition holds for the Heaviside function by setting V equal to the CG volume in Eq. (3.17). For the Gaussian function, a cut-off Gaussian function is typically used, i.e., $\Theta(w) = 4\pi w^3 \int_0^1 s^2 e^{-s*s} ds$ to ensure $\int_{R^3} G(r)dr = 1$

To effectively calculate the contact stress in Eq. (3.16) we use the algorithm 3.1.

Algorithm 3.1 : Coarse graining algorithm to determine the CG stress

Input parameters: CG radius w_c and system size.
Output parameters: CG stress tensor of the system
Input data: The position of contacting particles and the inter-particle forces.

1. Read the position of particles i, $\mathbf{r}_i$, and determine the CG volume index $c1$ and the CG volume position $\mathbf{r}_{c1}$. Similarly, determine the CG volume index $c2$ for particle j and the CG volume position $\mathbf{r}_{c2}$
2. 2.1 If $\|\mathbf{r}_{c1}-\mathbf{r}_i\| \leq w_c$, calculate the contact stress (Eq. (3.16)) arising from particles i and j and add it to $\sigma^{c}_{\alpha\beta}(\mathbf{r}_{c1})$

   2.2 If $\mathbf{r}_{c1} \neq \mathbf{r}_{c2}$ and $\|\mathbf{r}_{c2}-\mathbf{r}_j\| \leq w_c$, calculate the contact stress arising from particle i and j and add to $\sigma^{c}_{\alpha\beta}(\mathbf{r}_{c2})$
3. else if $\|\mathbf{r}_{c1}-\mathbf{r}_i\| > w_c$ and $\|\mathbf{r}_{c2}-\mathbf{r}_j\| \leq w_c$, calculate the contact stress and add it to $\sigma^{c}_{\alpha\beta}(\mathbf{r}_{c2})$

To assess how the CG function impacts the calculated CG stress, we use the model shear flow system illustrated in Figure. 2.2. The simulation parameters are identical to the ones listed in Table 2.1. Figure 3.3 confirms that the specific CG function has a very small effect on the determined CG stress (the hydrostatic pressure profile is plotted in Figure 3.3 for comparison). To reduce the computational complexity, the Heaviside was used as the CG function in this thesis.

Further, when plotting the normal contact stress in the x, y and z directions, Figure. 3.4, we observe that the common assumption of an isotropic stress distribution is a good approximation although $\sigma_{yy} \cong \sigma_{xx} > \sigma_{zz}$, which is in agreement with previous reports (Weinhart et al. 2013).

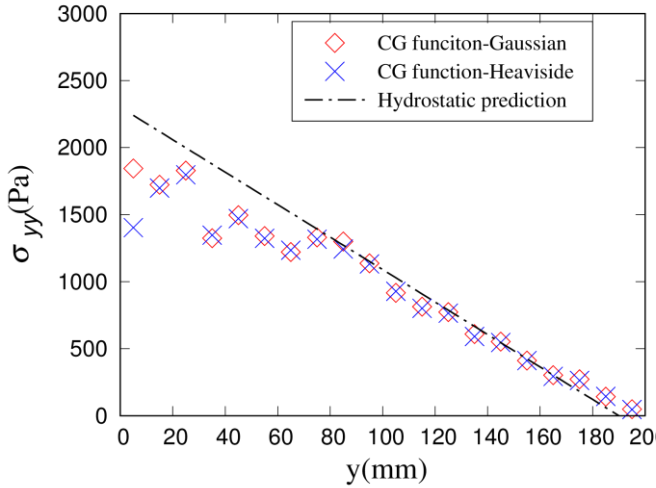

FIG. 3.3. The normal component of the CG stress tensor for a dense granular shear flow using either the Gaussian (◇) or the Heaviside function (×) as the CG function (t = 19 s). The CG radius is w_c = 0.005 m. The dash-dotted line gives the hydrostatic pressure profile: $\sigma_{yy} \cong P = \rho_p \phi g_y (h_c - y)$ where $\rho_p = 2.5\times10^{-6}$ g/mm^3, $\phi = 0.55$, $g_y = g\cos(26°)$ and $h_c = 200$ mm. The simulation setup and the simulation parameters are shown in Figure 2.2 and listed in Table 2.1, respectively.

Concerning the kinetic stress $\sigma^{k}_{\alpha\beta}$ in the modeled dense shear flow system we observe a linear dependence between the kinetic stress and the depth (Figure 4.5). However, its magnitude (~10^{-6} Pa) is much smaller compared to the contact stress (~10^{3} Pa). The negligible contribution of the kinetic stress to the stress tensor originates from the dense nature of the granular system studied, limiting large velocity fluctuations. In contrast, the contribution of the kinetic stress term becomes important in granular gases (Glasser and Goldhirsch 2001).

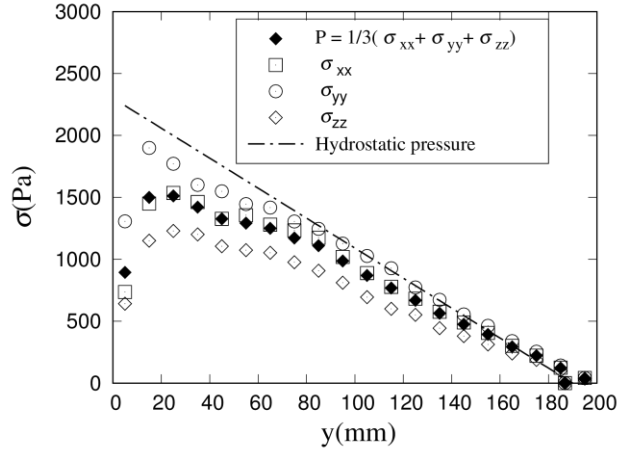

FIG. 3.4. Normal stress components $\sigma_{\alpha\alpha}$ as a function of the position along the y direction using a CG radius of $w_c = 5$ mm. The normal stress in the y-direction can be approximated very well by the hydrodynamic pressure, i.e., $\sigma_{yy} \cong P = \rho_p \phi g_y (h_c - y)$. Deviations from the hydrodynamic pressure near the bottom layer are due to wall effects.

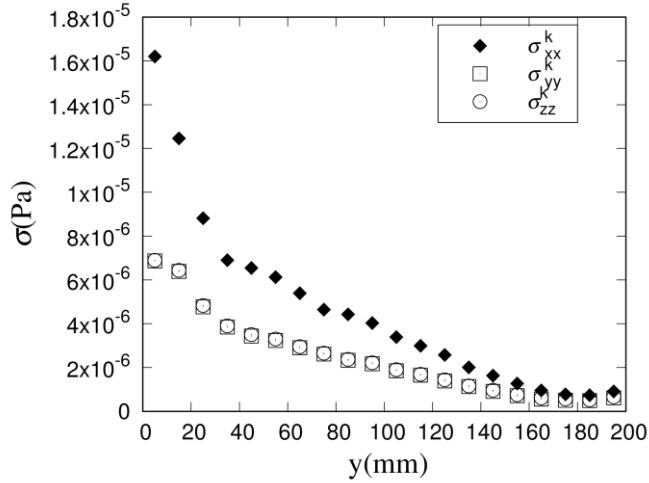

FIG. 3.5. Normal kinetic stress $\sigma^k_{\alpha\alpha}$ in the model dense shear flow studied here using a CG radius of $w_c = 5$ mm. The normal kinetic stress shows largely a

linear relationship in the y-direction. The kinetic stress in the flow direction (x direction) is larger than that in the y and z directions. The magnitude of the kinetic stresses is significantly smaller compared to the contact stresses in the dense granular shear flow system modelled here.

4 Accurate buoyancy and drag force models to predict particle segregation in vibrofluidized

Adapted from: Oshtorjani, M. K., Meng, L., & Müller, C. R. (2021). Accurate buoyancy and drag force models to predict particle segregation in vibrofluidized beds. *Physical Review E*, *103*(6), 062903.

4.1 Abstract

The segregation of large intruders in an agitated granular system is of high practical relevance, yet the accurate modeling of the segregation (lift) force is challenging as a general formulation of a granular equivalent of a buoyancy force remains elusive. Here, we critically assess the validity of a granular buoyancy model using a generalization of the Archimedean formulation that has been proposed very recently for chute flows. The first model system studied is a convection-free vibrated system, allowing us to calculate the buoyancy force through three different approaches, i.e., a generalization of the Archimedean formulation, the spring force of a virtual spring, and through the granular pressure field. The buoyancy forces obtained through these three approaches agree very well, providing strong evidence for the validity of the generalization of the Archimedean formulation of the buoyancy force which only requires an expression for the solid fraction of the intruder, hence allowing for a computationally less demanding calculation of the buoyancy force as coarse graining is avoided. In a second step, convection is introduced as a further complication to the granular system. In such a system, the lift force is composed of granular buoyancy and a drag force. Using a drag model for the slow-velocity regime, the lift force, directly measured through a virtual spring, can be predicted accurately by adding a granular drag force to the generalization of the Archimedean formulation of the granular buoyancy. The developed lift force model allows us to rationalize the dependence of the lift force on the density of the bed particles and the intruder diameter, and the independence of the lift force on the intruder density and the vibration strength (once a critical value is exceeded).

Segregation is commonly observed in granular materials that contain a mixture of particles that differ in size (Duran, Rajchenbach, and Clement 1993; Hill and Fan 2008; Pouliquen, Delour, and Savage 1997; van der Vaart et al. 2015), density (Hong, Quinn, and Luding 2001; Huerta and Ruiz-Suarez 2004), shape (Lu and Muller 2020) or mechanical properties (friction, elasticity) (Gillemot, Somfai, and Borzsonyi 2017; Windows-Yule et al. 2014). A fundamental understanding of the physics behind segregation in granular materials is not only a scientific curiosity (Seife 2005; Lu, Third, and Muller 2015; McLaren et al. 2019), but also of high relevance for practice. In practical applications such as the mixing of pharmaceutical ingredients (Vanarase et al. 2010), the filling (and discharge) of hoppers (Ketterhagen et al. 2007)or the transport of granular media through agitation (e.g. vibration) from one processing unit to the other (Simsek et al. 2008; Hamzeloo, Massinaei, and Mehrshad 2014) size- and density-induced segregation is unavoidable and has to be controlled or at least minimized when designing unit operations or granular conveyer systems. In most industrial applications such as the food or pharmaceutical industries a well-mixed state is desired and indeed critical to ensure the desired product specification, hence an in depth understand of the parameters controlling segregation is critical. Besides the industrial relevance of segregation, it also prevails in dynamic natural phenomena such as debris flow (Ferdowsi et al. 2017). A well-studied segregation phenomenon is the so called "Brazil nut phenomenon" (BNP)(Rosato et al. 1987), which describes the upward motion of an intruder in a vibrating granular bed, where the intruder diameter is larger than the diameter of the bed particles.

Qualitative models

Depending on the vibration strength, the BNP can be rationalized by one of the following two models. The first model is valid for low vibration strengths (typically low or even irregular vibration frequency), the upward migration of the intruder is explained by the arch (or vault) effect, whereby upon an upward movement of the intruder, voids are formed at the bottom part of the intruder. A new, higher, intruder position in the bed is stable if the large intruder is support by at least two particle contacts below its center of gravity (2D case).

Small bed particles are able to easily fill the voids below the intruder leading to a continuous upward motion of the intruder through a series of stable intruder "jumps". This explanation has been termed also percolation model (Duran et al. 1994; Duran, Rajchenbach, and Clement 1993; Jullien, Meakin, and Pavlovitch 1992, 1993; Rosato et al. 1987). In such a segregation regime, a critical minimal size of an intruder compared to the bed particle size, is required to trigger segregation (Jullien, Meakin, and Pavlovitch 1993, 1992; Duran et al. 1994) and the rise velocity of the intruder increases with increasing intruder size (Duran et al. 1994). According to the second model, which is valid under conditions of high vibration strength (typically a high vibration frequency), a convection cell establishes in the vibrating bed. This convection cell carries the intruder upwards in the center of the bed, leading to a rise velocity of the intruder that is independent of the ratio of the intruder size to bed particle size (Andreotti, Forterre, and Pouliquen 2013). The region of downward particle motion at the walls is thin, making it impossible for the large intruder to be convected downwards once it has reached the top surface of the bed (Duran et al. 1994; Knight, Jaeger, and Nagel 1993a). Depending on the type and strength of agitation of a granular bed, the intruder size (Cooke et al. 1996; Duran et al. 1994; Duran, Rajchenbach, and Clement 1993) and/or density (Huerta and Ruiz-Suarez 2004; Shinbrot and Muzzio 1998; Shishodia and Wassgren 2001) are known to affect the tendency for segregation. In general, bigger and lighter intruders segregate more favorably.

Quantitative models

In recent years, attempts have been made to develop not only qualitative, but also quantitative segregation models, which requires a hydrodynamic description of a segregating granular bed. So far, no model has been found which describes a segregation force on an intruder that is generally applicable. Instead, separate models have been developed which are only applicable to either dilute(Jenkins and Yoon 2002; Garzo 2008)or dense granular systems(Lu and Muller 2020; Guillard, Forterre, and Pouliquen 2016; van der Vaart et al. 2015). Additionally, among the models for dense systems one finds different models for either sheared systems, i.e. systems with convective particle motion, or vibrated systems with no inherent convective motion.

In this context, Shishodia and Wassgren (2001) modelled the segregation of intruders in a two-dimensional (2D) vibro-fluidized bed using the discrete element method (DEM), i.e. a Lagrangian modelling approach that is related to molecular dynamics simulations. They considered a shallow bed, i.e. the ratio of the bed height to width was < 1, that contained frictionless particles. A consequence of this dilute vibrated bed was that the vertical granular pressure gradient was constant only over a very small height, with increasing and decreasing pressure gradients with vertical position below and above the center of the bed, respectively. Shishodia and Wassgren (2001) observed that upon vibration the intruder reached an equilibrium position within the bed. At the equilibrium position, the downward directed gravitational force is balanced by a net lift force due to particle-intruder contacts. The vertical position of the equilibrium position of the intruder was found to increase with increasing vibration strength, decreasing density ratio of the intruder to the bed particles and increasing coefficient of restitution. Subsequently, Shishodia and Wassgren (2001) developed a hydrodynamic model of the granular system to predict the equilibrium position of the intruder, whereby a buoyancy force F_b, which balances the intruder weight, arises from the net pressure in the system:

$$F_b = \oint p \cdot \mathbf{n} d\mathbf{s} \,. \tag{4.1}$$

In a 2D granular system, the (granular) pressure is $P = 1/2(\tau_{s,xx}+\tau_{s,yy}+\tau_{c,xx}+\tau_{c,yy})$, where $\tau_{s,xx}$ and $\tau_{s,yy}$ are the streaming normal stresses and $\tau_{c,xx}$ and $\tau_{c,yy}$ are the collisional normal stresses (Campbell and Gong 1986; Shishodia and Wassgren 2001) . In 2D, the streaming normal stresses are given by $\tau_{s,xx}= \varrho_p \phi \langle u'^2 \rangle$ and $\tau_{s,yy} = \varrho_p \phi \langle v'^2 \rangle$, where ϱ_p is the particle density, ϕ is the mean solid fraction and u' and v' are the velocity fluctuations in the horizontal and vertical directions, respectively. Here, $\langle\ \rangle$ denotes a temporal average. The collisional normal stresses are given by $\tau_{c,xx} = \frac{\sum r_p \mathbf{J}\cdot\mathbf{e}_x}{W \Delta y_{bin} \Delta t}$ and $\tau_{c,yy} = \frac{\sum r_p \mathbf{J}\cdot\mathbf{e}_y}{W \Delta y_{bin} \Delta t}$ (Shishodia and Wassgren 2001) , where r_p is the radius of the bed particles**,** $\mathbf{J}$ is the momentum exchange during a collision, W and Δy_{bin} are the width and height of the sampling bin, respectively, and $\mathbf{e}_x$ and $\mathbf{e}_y$ are the unit vectors

along the x and y directions. The summation is performed over all collisions occurring within time Δt in a given bin. Shishodia and Wassgren (2001) postulated that at equilibrium, the pressure force acting on the intruder (i.e., buoyancy) balances the particle weight, yielding (in a 2D system):

$$\frac{dp}{dy} = \frac{-m_I \mathbf{g}}{\pi d_I^2} = -\rho_I \mathbf{g}\,, \tag{4.2}$$

i.e., an intruder that is larger than the bulk particles will rise up to the position where the pressure gradient equals $-m_I g/\ \pi d_I^2$, where m_I and d_I are the mass and diameter of the intruder, respectively. This model relies on the assumption that the presence of an intruder does not affect the pressure field of the system that is established without the presence of an intruder. Using Eq. (4.2) in combination with a given pressure profile in the granular bed, the equilibrium position of an intruder can be calculated. When the mass of the intruder becomes too large (to be supported by the pressure gradient), the intruder sinks to the base plate and oscillates synchronously with the base plate. However, Shishodia and Wassgren (2001) noted that the findings of their model might not be readily extrapolated to deep granular beds due to a large number of non-binary contacts, the possible occurrence of convective patterns and the effects of an interstitial fluid.

Lift force in dense sheared systems

More recently, also the hydrodynamic modeling of segregation in dense shear flows has attracted appreciable interest (Guillard, Forterre, and Pouliquen 2016; Hill and Tan 2014; Tripathi and Khakhar 2013; van der Vaart et al. 2018). For example, Guillard et al. (Guillard, Forterre, and Pouliquen 2016) proposed scaling laws for the segregation force acting on single intruder in 2D, dense shear flows. In their shear flow simulations, the particles were modelled by DEM with the gravitational vector varying from vertical to horizontal directions. The segregation (or lift) force was measured via a virtual spring and was found to be proportional to the pressure gradient and shear stress gradient (i.e., buoyancy-like forces), viz.

$$F_{lift} = -\frac{\pi d_I^{\,2}}{4}\left(\mathcal{F}\frac{\partial p}{\partial y} + \mathcal{G}\frac{\partial |\tau|}{\partial y}\right), \tag{4.3}$$

where $\mathcal{F}$ and $\mathcal{G}$ are empirically derived functions of the friction coefficient, $\mu = |\tau|/p$ and size ratio d_I/d_p. Interestingly the segregation force was found to have a maximum at $d_I/d_p \sim 2$ and switching off gravity resulted in a zero-segregation force owing to a uniform pressure distribution in the bed.

van der Vaart et al. (2018) followed up on the work of Guillard, Forterre, and Pouliquen (2016) aiming to shed more light on the origin of the segregation (lift) force in 3D monodisperse, dense shear flows. Unlike Guillard, Forterre, and Pouliquen (2016), van der Vaart et al. (2018) modelled the segregation force acting on the intruder, F_{lift}, as the sum of a Saffman like lift force and a generalized buoyancy force that depends on the ratio of the diameter of the intruder to the diameter of the bed particles, i.e. $F_{lift} = F_{saff} + F_b$, where F_{lift} is the total lift (segregation) force, F_b is the buoyancy and F_{saff} is the Saffman force. van der Vaart et al. (2018) argued that the granular buoyancy force arises from the hydrostatic pressure acting on the Voronoi surface of the intruder, yielding a more generalized expression of the buoyancy force (van der Vaart et al. 2018), viz:

$$\begin{aligned} F_b &= \oint p\mathbf{n}\cdot d\tilde{\mathbf{S}}_I = \phi\rho_p g\int_{\tilde{V}_I} dV \\ &= \phi\rho_p g\tilde{V}_I = \frac{\phi}{\phi_I}\rho_p g V_I \end{aligned}, \tag{4.4}$$

Where $\widetilde{S}_I$ is the surface of the Voronoi volume of the intruder, $\widetilde{V}_I$ is the Voronoi volume of the intruder, P is the hydrostatic pressure, $\mathbf{n}$ is the outward-directed normal vector to $\widetilde{S}_I$ The Voronoi volume of a particle in a granular system is the volume of a cell that contains all of the space that is closer to the particle considered than any other particle. Eq. (4.4) differs from the classic Archimedian formulation of a buoyancy force in a granular media, i.e., $F_b = \phi\rho_f g V_I$, as it is a function of d_I/d_p (with $F_b = m_I g = F_g$ for $d_I/d_p = 1$). Using DEM simulations, the following empirical equation $\phi_I = (\phi - 1)(d_I/d_p)^c + 1$ ($c = -1.2$ and $\phi = 0.577$) was obtained. Subtracting the

granular buoyancy force from the contact force F_c a granular Saffman-type lift (segregation) force was obtained and expressed as $F_{saff} = -\lambda_x \eta b I_\theta \mu^{-0.5} d_l^2 d_p^{-1} \mathrm{sng}(\dot{\gamma})$, where $\lambda_x = <v_{lx}(t) - v_x(z_l,t)>$ is the velocity lag of the intruder with respect to the bulk downstream flow, $\eta = |\tau|/\dot{\gamma}$ is the granular viscosity, $I_\theta = \dot{\gamma} d/(P/\varrho)^{0.5}$ is the inertial number , $\mu = |\tau|/P$ is the bulk friction coefficient μ, $\dot{\gamma}$ is the local shear rate and a is the fitting parameter.

Buoyancy in dense convection-free systems

In the systems described above (section 4.2) a shear flow has been present. Hence, granular drag and/or forces arising from velocity gradients might affect segregation making in turn the elucidation of the contribution of the buoyancy force on segregation challenging if not even impossible. An ideal system to study segregation would be free of a convective flow pattern. To avoid convection in a vibrated bed, Huerta et al. (2005) proposed an experimental setup to vibrate the lateral walls of the bed such that adjacent walls move out of phase ($\varphi_2 - \varphi_1 = \pi$), ensuring an almost constant bed volume. Indeed, Huerta et al. (2005) could not observe any convective patterns ,which was probed by placing tracer particles. Subsequently, Huerta et al. (2005) measured the lift force (which equals to the buoyancy force in a convection/velocity-free system) acting on the intruder using a dynamometer that was connected with a wire to the intruder. Key observations of the experimental work of Huerta et al. (2005) were (i) the buoyancy force becomes independent of Γ for $\Gamma > \Gamma_{cr} = 5$, and (ii) the buoyancy force follows Archimedes' principle, i.e., buoyancy is proportional to the volume displaced. However, fitting the experimentally determined buoyancy force as a function of the intruder volume V_I gives a positive intercept for $V_I = 0$, which might suggest that a classic Archimedian formulation of the buoyancy force underestimates the buoyancy force as V_I approaches small values. This observation was explained by Huerta et al. (2005) by the argument that when the intruder size approaches the size of the bed particle, the intruder becomes indistinguishable from the bed material and they suggested that buoyancy only occurs for intruders that are "considerably large than the volume of the beads".

Drag force in convective systems

However, in most of the naturally and industrially prevalent granular systems, convection is inherent. Hence, when studying the segregation dynamics of intruders in such systems, the drag force acting in the opposite direction to the (relative) intruder motion has to be considered. Generally, two different drag regimes have been considered, viz. a slow and rapid-velocity regime (Albert et al. 1999; Wieghardt 1975). The motion of an intruder in dense vibrating beds, i.e. the system considered in our work, will typically fall into the slow velocity regime in which the drag force is independent of the relative intruder velocity. Albert et al. give a commonly used drag force correlation for a discrete object with a circular cross sectional area in the slow flow regime (Albert et al. 2001; Albert et al. 1999)as:

$$F_d = \eta g \rho_p (y_b - y) d_I^{\,2} \ , \tag{4.5}$$

where ϱ_p is the density of the bed particles; d_I is the diameter of the intruder; $y_b$is the filling height of the bed; y is the intruder position along the bed height and $\eta = B\sqrt{32\pi^2/27e^2}$, where e is the coefficient of restitution; B is a constant depending on the surface properties, morphology, and packing of the grains. The independence of the drag force on the intruder velocity in the slow velocity regime has been confirmed by Reddy et al. (Reddy, Forterre, and Pouliquen 2011).

A general segregation force

Here we propose a segregation model, which is generally applicable to dense systems, with and without convective motion. To this end, a model system is created where convection can be turned on/off by switching friction between particles and walls on/off. Switching wall friction on introduces an upwards convection in the center of the bed which in turn leads to a drag force on the intruder. By subtracting the buoyancy, which is determined by the generalized buoyancy model, from the lift force, we could obtain the drag force, i.e. $F_d = F_{lift} - F_b$, which suggests that the value of F_d depends on the chosen buoyancy model. By confirming whether the drag force agrees with the granular drag

model Eq. (4.5), we could further verify and extend the applicability of the generalized Archimedean principle in the system under consideration.

The first objective of our work is to probe numerically the validity of a generalized Archimedean formulation, Eq. (4.4), to describe a granular buoyancy force. Eq. (4.4) has been proposed for chute flows and takes into account the solid fraction around an intruder. To this end we use a model system, i.e., a vibrating bed that is free from convection (zero wall friction). The vibrating bed is vibrated horizontally and the validity of Eq. (4.4) is assessed by measuring the magnitude of the buoyance force through a virtual spring force F_s via $F_b = F_s + mg$ and through its definition by integration of the stress tensor on the intruder surface (Eq. (4.1)).

We subsequently expand our study to a system that contains convection (by imposing friction to the side walls) which inevitably introduces also a drag force that acts onto the intruder. The drag force is determined by subtracting the buoyancy force (Eq. (4.4)), from the total lift force i.e. $F_d = F_{lift} - F_b$ and through a granular drag force formulation.

Using a granular drag force formulation, we are able to correctly predict the segregation (lift) acting on an intruder in a granular system and to correctly predict the dependence of the lift force on a variety of system parameters, hence providing a general modelling framework to predict the segregation and buoyancy forces on granular intruders in dense granular systems with and without convection, i.e., sheared and vibrated

4.3 Method

In this work, the system under investigation is a rectangular bed containing 27'000 particles (Fig. (4.1)). To allow a comparisons with the experimental work of Huerta et al. (2005) the following particle mixture is used: 50:50, bi-dispersed mixture of glass beads of radii 1.5 and 2.0 mm (density of 2240 kg/m^3). The length, width and filling height of the container are $x = 107$ mm, $z = 107$ mm and $y = 95$ mm, respectively. The lateral walls of the container are excited sinusoidally in the xz plane. Two walls opposite of each other vibrate by imposing the displacement $x(t) = \pm A_0 \sin(\omega t + \phi_1)$ with A_0 being the

amplitude and $f = \omega_0/(2\pi)$ the frequency of the excitation. The vibration of the other two side walls is given by $z(t) = \pm A_0 \sin(\omega t + \phi_2)$, hence adjacent walls move out of phase by $\phi_2 - \phi_1 = \pi$. Such a vibration leads to an almost constant square area (+/-0.07%) with time, avoiding arguably the formation of convection patterns. Inside the bed, an intruder is placed at the coordinates (0 mm, 50 mm, 0 mm) and the vibration is initiated at t = 0 s. The intruder diameter was varied from 1.67 $\overline{d_p}$ to 12 $\overline{d_p}$ in the simulations, where $\overline{d_p}$ is 3.5 mm, which is the average bed particle diameter of the system.

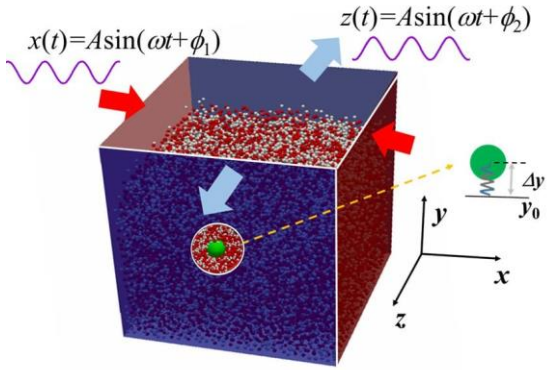

FIG. 4.1. Illustration of the simulated granular system. An intruder is immersed inside the granular bed and connected to a virtual spring. The lift force is determined via the measured spring force, i.e. $\mathbf{F}_{lift} = -(\mathbf{F}_s + \mathbf{F}_g)$, where the spring force is calculated using Hooke's law, $F_s = k\Delta y \mathbf{e}_y$, where k is the spring stiffness of the virtual spring and Δy is the vertical displacement of the intruder compared to its initial positon. The sidewalls are vibrated such that the two walls (red wall) opposite of each other follow the displacement $x(t) = \pm A_0 \sin(\omega t + \phi_1)$ with A_0 being the amplitude and $f = \omega_0/(2\pi)$ the frequency of the excitation. The vibration of the other two side walls (blue wall) is given by $z(t) = \pm A_0 \sin(\omega t + \phi_2)$,, hence adjacent walls move out of phase by $\phi_2 - \phi_1 = \pi$.

The vibration strength, $\Gamma = A_0\omega_0^2/g$ applied in this work ranged from Γ = 2.51 ~ 60 (varied through changes in the frequency while keeping the amplitude fixed at A_0 = 1 mm). The interactions between the particles were modelled via a discrete element method (DEM) (Cundall and Strack 1979) using the open source LIGGGHTS package (Kloss et al. 2012). A spring-dashpot model describes the collisional forces (normal F_{nij} and tangential contact force F_{tij}):

$$\mathbf{F}_{nij} = \sqrt{\delta_{nij}R^*}(k_n\delta_{nij}\mathbf{n}_n - \eta_n\mathbf{v}_{nij}), \tag{4.6}$$

$$\mathbf{F}_{tij} = \sqrt{\delta_{tij}R^*}(-k_t u_{ij}\mathbf{n}_\mathbf{t} - \eta_t\mathbf{v}_{tij}), \tag{4.7}$$

where k_n and k_t are the spring constants in the normal and tangential direction (given by $k_n = 4/3E^*$ and $k_t = 8G^*$, with $E^* = ([1-\nu_i^2]/E_i+[1-\nu_j^2]/E_j)^{-1}$ and $G^*=([2-\nu_i^2]/G_i+[2-\nu_j^2]/G_j)^{-1}$ where E_{ij}, ν_{ij} and G_{ij} are the particle's Young's modulus, the Poisson ratio and the shear modulus, respectively). Further, η_n and η_t are the damping coefficients in the normal $\mathbf{n}_n$ and tangential $\mathbf{n}_t$ directions, respectively. The overlap between two particles in the normal direction is $\delta_{nij} = |\mathbf{u}_i-\mathbf{u}_j|\Delta t$, where $\mathbf{u}_i$ and $\mathbf{u}_j$ are the velocities of the ith and jth particle at t_0 and Δt is the time interval. The tangential displacement of a contact is calculated as, $\delta_{tij} = (\mathbf{u}_{ik} - \mathbf{u}_{jk})\mathbf{n}_n\Delta t - (\boldsymbol{\omega}_{j(k+1)}\mathbf{n}_{k+2} - \boldsymbol{\omega}_{j(k+2)}\mathbf{n}_{k+1})r_i\Delta t - (\boldsymbol{\omega}_{i(k+1)}\mathbf{n}_{k+2} - \boldsymbol{\omega}_{i(k+2)}\mathbf{n}_{k+1})r_j\Delta t$, where k rotates from x to z, r_i and r_j are the radius of the particle i and particle j. respectively, and ω is the angular velocity. The tangential contact force is limited by Coulomb's law, i.e. $|F_{tij}| \leqslant \mu|F_{nij}|$ A summary of the values of the modelling parameters used in this work is given in Table 4.1.

To determine the segregation force acting on the intruder, a virtual spring is used (Guillard, Forterre, and Pouliquen 2016). The virtual spring connects the center of the intruder to its initial position (0 mm, 50 mm, 0 mm) (Fig. 4.1). In the system modeled (convection free), three forces act on the intruder: (i) gravitation, F_g, (ii) the force exerted by the virtual spring F_s and (iii) the lift force arising from the contacts between the bed particles and the intruder (the lift force is commonly also referred to as the segregation force) (van der

Vaart et al. 2018; Guillard, Forterre, and Pouliquen 2016). Hence, at equilibrium the lift force acting on the intruder is balanced by

$$\mathbf{F}_{lift} = \mathbf{F}_c = -(\mathbf{F}_g + \mathbf{F}_s), \tag{4.8}$$

where $\mathbf{F}_c$ is (the sum of) the contact forces acting between the intruder and the surrounding bed particles, $\mathbf{F}_s = k \times (y - y_0)\mathbf{e}_y$ with k being the stiffness of the virtual spring, y is the average vertical position of the intruder for a given setting and y_0 is the initial position of the intruder that is fixed to $y_0 = 50$ mm. As an example, Fig. 4.2 plots the instantaneous vertical position of an intruder as a function of time over 200 s.

From Fig. 4.2 we can observe that the intruder rises quickly and reaches an equilibrium position, around which it oscillates after ~ 20 s. The values of the intruder position reported in the following are the values obtained in this equilibrium state (with simulations typically being performed over 200 s). To assess whether the magnitude of the spring stiffness of the virtual spring affects that numerical results, simulations were repeated for varying values of k As shown in Fig. 4.3 the lift force is independent of the spring stiffness k for 5 N/m < k < 200 N/m, in agreement with a previous report (Guillard, Forterre, and Pouliquen 2016). The inset in Fig. 4.2 plots $\Delta y = y - y_0$ of the intruder, normalized by the intruder diameter, as a function of the normalized spring stiffness of the virtual spring. The slope of this line, multiplied by the diameter of the intruder d_I and the normal stiffness of the inter-particle collisions k_n is equal to the spring force. Owing to the very high linearity, the lift force acting on the intruder can be determined via Eq. (4. 8). In this work a constant spring stiffness of k = 80 N/m was used for the virtual spring.

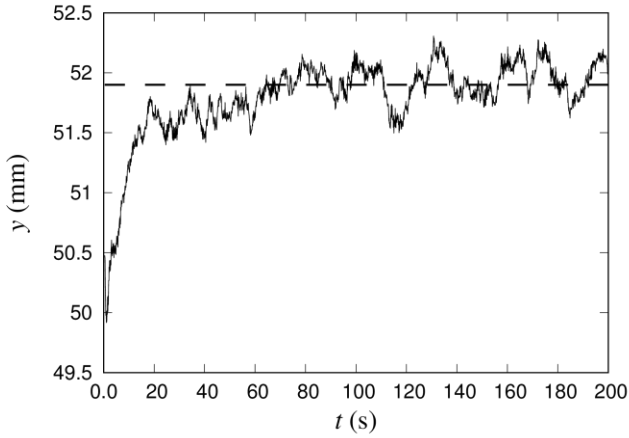

FIG 4.2. Vertical position of an intruder tracked over 200 s. The dashed horizontal line corresponds to the equilibrium position around which the intruder oscillates.

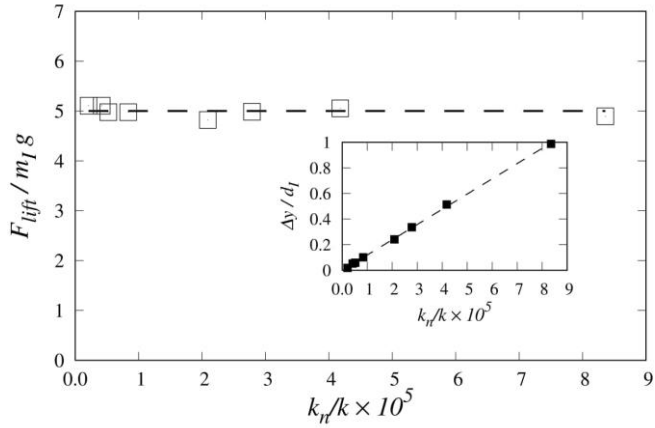

4.

FIG 4.3. Normalized segregation (lift) force as a function of the spring stiffness k normalized by the stiffness of the inter-particle force, i.e., $k_n = 4.18\times10^6$ N/m. Inset: $\Delta y = y - y_0$ of the intruder as a function of the normal spring stiffness of the virtual spring.

We further assessed the sensitivity of the determined segregation force to the amplitude A and the angular frequency ω of the vibration. Fig. 4.4 confirms that the lift force is not sensitive to the amplitude and angular frequency of the vibration for a given vibrational strength Γ.

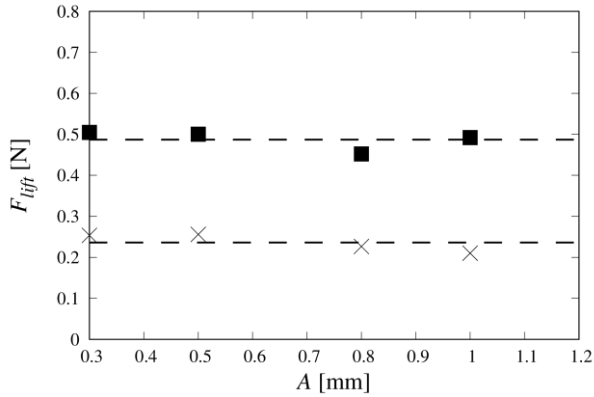

FIG 4.4. Lift force versus vibrational amplitude A, × : Γ = 8.0, d_I / d_p = 5 and ■: : Γ = 20.0, d_I / d_p = 7.

4.4 Results

Prior to assessing the validity of the different granular buoyancy models, we performed a sensitivity analysis of the dependence of the lift force on the dimensionless vibration strength Γ, as a minimal value of Γ is required to fluidize the system (Huerta et al. 2005; Huerta and Ruiz-Suarez 2004). Figure 5 plots the lift force (Eq. (8)) as a function of Γ. Similar to the experimental observation of Huerta et al. (2005), we also observe that the lift force reaches asymptotic values for $\Gamma > 6$ (inset Fig. 4. 5). The reason for a decreasing lift force for $\Gamma < \Gamma_{cr}$ is that under these conditions only the regions close to the walls are fluidized whereas the center of the bed is only poorly fluidized, leading in turn to reduced segregation dynamics. Indeed, when Huerta et al. (2005) inserted two small intruders into a bed that was kept at $\Gamma < \Gamma_{cr}$ (one intruder was placed close to the walls and the other one in the center of the bed) the intruder closer to the wall segregated faster to the top surface.

Overall, the value of $\Gamma_{cr} \sim 6$ as determined in our simulations, is close to the experimental value of $\Gamma_{cr} = 5$ of Huerta et al. (2005). Once the bed is completely fluidized, a further increase in Γ does not have any appreciable effect on the lift force. Indeed, Fig. 4.5 confirms that the magnitude of the lift force does not vary with Γ for $8 < \Gamma < 60$. In addition to the lift force, also the solid fraction in the bed ($\phi = 0.62$) is largely unaffected by Γ when $\Gamma > \Gamma_{cr}$ (Figure. 4.6). Overall, the solid fraction is very homogenous along the height of the bed, except at the bottom, i.e. $y < 0.02$ m and close to the surface, i.e. $y > 0.075$ m, of the bed where smaller values of ϕ are observed.

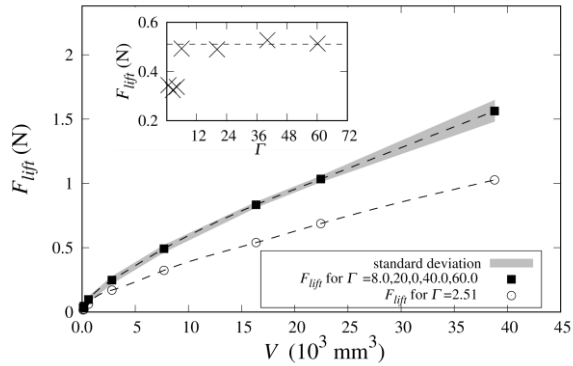

FIG 4.5. Lift force as a function of the volume of the intruder for five different vibration strengths grouped as $\Gamma = 2.51 < \Gamma_{cr}$ and $\Gamma = 8.0,20.0,40.0,60.0 > \Gamma_{cr}$ where $\Gamma_{cr} = 6$ is the critical vibration strength. Inset: Lift force as a function of vibration strength (d_l/d_p) to determine Γ_{cr}.

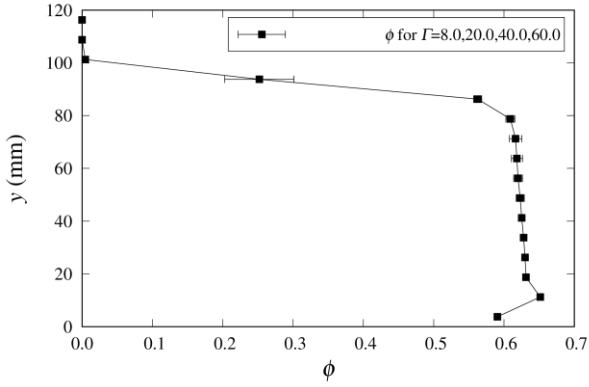

FIG 4.6. Profile of the solid volume fraction ϕ in the bed as a function of the y direction for $8 < \Gamma < 60$.

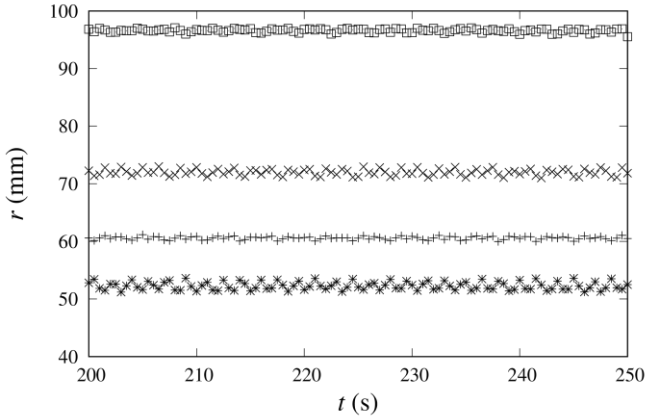

FIG 4.7. Temporal evolution of position $r = (x^2+y^2+z^2)^{0.5}$ of randomly selected particles in the bed, when the friction coefficient for wall-particle collisions is set to zero ($\Gamma = 8.0$).

To probe the validity of the generalized Archimedean formulation of the granular buoyancy force, Eq. (4.4), a system free of convective patterns is critical to exclude the presence of any additional forces, e.g. Saffman-type or drag forces. By setting the friction coefficient for particle-wall contacts to zero, we were able to establish an agitated (fluidized) system without any convection

pattern being present. Tracing some randomly selected particles in the bed for 100 s, we could confirm the absence of any coherent motion in the bed (Fig. 4.7). In the absence of a convective pattern, the lift force F_{lift} is equal to the buoyancy force F_b and can be calculated by subtracting the gravitational force of the intruder from the measured spring force (Eq. (4.8)). The buoyancy force calculated through Eq. (4.8) can then be compared to the prediction of F_b via a generalized Archimedean formulation (Eq. (4.4)) using the Voronoi volume of the intruder $\widetilde{V_I}$. The Voronoi volume of the intruder is illustrated in Fig. 4.8. The solid fraction of the intruder ϕ_I is determined as the ratio of its (particle-based) volume ($V_I = 1/6\pi d_I^3$) and its Voronoi volume. Figure 4.8 shows that when the intruder size approaches the size of the bed particles, ϕ_I approaches the bulk solid fraction of the bed, i.e. $\phi_I = 0.62$. On the other hand for very large intruder sizes, ϕ_I approaches asymptotically to 1. The numerically-derived values of ϕ_I can be fitted well by the following functional form $\phi_I = (\phi - 1)(d_I/d_p)^c + 1$ with $c = -1.2$. Our value of c is slightly different to the value reported by van der Vaart et al. (2018) ($c = -1.35$) who studied, however, sheared systems containing monodispersed particles.

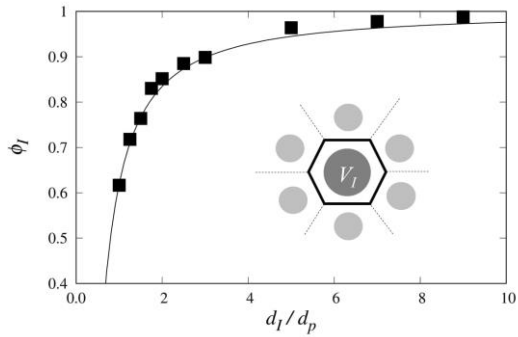

FIG 4.8. Solid volume fraction of the intruder ϕ_I as a function of d_I/d_p for $\Gamma = 8$, $k = 80$ N/m. The closed area around the intruder which is bounded by a bold solid line gives the Voronoi volume $\widetilde{V_I}$ of the intruder.

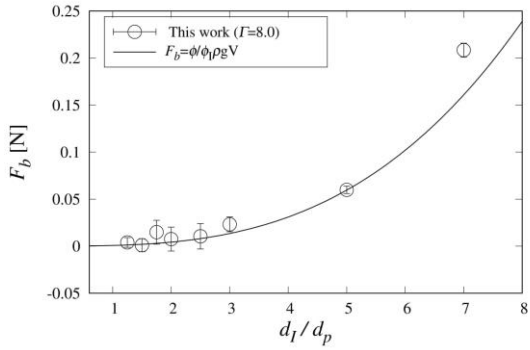

FIG 4.9. Comparison of the generalized Archimedean formulation of the granular buoyancy force (Eq. 4.4) with the buoyancy force determined by the virtual spring force $\mathbf{F}_{lift} = -(\mathbf{F}_s + m_I\mathbf{g})$ in a vibrated bed with $\Gamma = 8.0$.

Figure 4.9 plots a comparison of the buoyancy force determined through the virtual spring (Eq. (4.8)) with the generalized Archimedean formulation of a granular buoyancy force (Eq. (4.4)). The prediction obtained through the generalized Archimedean principle (Eq. (4.4)) and the buoyancy force obtained directly from the DEM simulations through the virtual spring force (Eq. (4.8)) agree very well, while some deviations are observed for high ratios of the intruder diameter to the diameter of the bed particles ($d_I / d_p = 7$). This deviation is most likely due to the fact that for such high aspect ratios the upper part of the intruder ($y_I \cong 76$ mm) is very close to the bed surface, i.e. an area where the solid fraction of the bed is reduced appreciably (see Fig. 4.6). The lower solid fraction near the bed surface reduces the magnitude of the total contact forces on the upper part of the intruder (downwards directed) hence increasing artificially the buoyancy of the intruder.

Besides Eqs. (4.4) and (4.8) the buoyancy force can be determined also through its formal definition i.e. by integrating the pressure field over the (Voronoi) surface of the intruder (Guillard, Forterre, and Pouliquen 2016; Shishodia and Wassgren 2001; van der Vaart et al. 2018), i.e.

$$F_b = \oint pn.e_y d\tilde{S} \,, \tag{4.9}$$

where $\tilde{S}_I$ is the Vornoi surface of the intruder. The coarse-graining (CG) method is used to calculate the (granular) pressure in the vibrated bed

(Goldenberg et al. 2006; Goldhirsch 2010). Here, we consider N particles in a control volume (also termed coarse graining volume) whereby the center of mass of particle i is at $\mathbf{r}_\alpha$ (particle i moves with speed u_i). In a granular media the stress tensor $\sigma_{\alpha\beta}(\mathbf{r},t)$ is composed of the so-called kinetic stress $\sigma^k_{\alpha\beta}(\mathbf{r},t)$ and the collisional stress $\sigma^c_{\alpha\beta}(\mathbf{r},t)$, viz.: $\sigma_{\alpha\beta}(\mathbf{r},t) = \sigma^k_{\alpha\beta}(\mathbf{r},t) + \sigma^c_{\alpha\beta}(\mathbf{r},t)$. The kinetic and collisional stresses are given by, respectively (Andreotti, Forterre, and Pouliquen 2013),

$$\sigma^k_{\alpha\beta}(\mathbf{r},t) = \sum_{i=1}^{N} m_\alpha u'^i_\alpha u'^i_\beta(\mathbf{r},t)\times\Theta[\mathbf{r}-\mathbf{r}_\alpha(t)], \tag{4.10}$$

$$\sigma^c_{\alpha\beta}(\mathbf{r},t) = -\frac{1}{2}\sum_{i,j,i\neq j} f^{ij}_\alpha(t) r^{ij}_\beta(t)\int_0^1 \Theta[\mathbf{r}-\mathbf{r}_i(t)+s\mathbf{r}_{ij}(t)]ds, \tag{4.11}$$

where u'^i_α is the velocity fluctuation of particle i with respected to the average velocity $\bar{U}(r,t)$ of the particles in the coarse graining volume. The vector $\mathbf{r}^{ij} = \mathbf{r}^i - \mathbf{r}^j$ points from the center of particle i to the center of particle j, f^{ij}_α is the contact force acting between particles i and j and Θ is the coarse-graining (CG) function. In this work, we use the Heaviside function $\Theta(\mathbf{r}) = H(w-|\mathbf{r}|)/V$ where $V = 4/3\pi r^3$ is the coarse graining volume and w is the coarse graining radius. The (granular) pressure P is obtained by $P = \mathrm{Tr}(\sigma_{\alpha\alpha})/3$(Andreotti, Forterre, and Pouliquen 2013).

The obtained pressure profiles (identical system but without an intruder) along the vertical (y) and horizontal (x) directions are plotted in Fig. 4.10 (a) and (b) respectively. While the pressure is almost constant along the horizontal direction, Fig. 4.10(b), an almost constant pressure gradient, similar to a classic hydrostatic pressure in a fluid is established in the vertical direction Fig. 4.10(a). However, at the bottom and the surface of the vibrated bed there are some appreciable deviations from a constant pressure gradient, similar to what has been observed in Weinhart et al. (2012). Since the intruder was placed at the center of the bed, these boundary effects did not affect the segregation behavior of the intruder. Using the determined pressure gradient, the buoyancy force can be calculated via:

$$F_b = \int p\cdot\mathbf{n}d\tilde{\mathbf{S}} = \int\left(\frac{\partial p}{\partial x}+\frac{\partial p}{\partial y}+\frac{\partial p}{\partial z}\right)d\tilde{V} \approx \frac{\partial p}{\partial y}\tilde{V}. \tag{4.12}$$

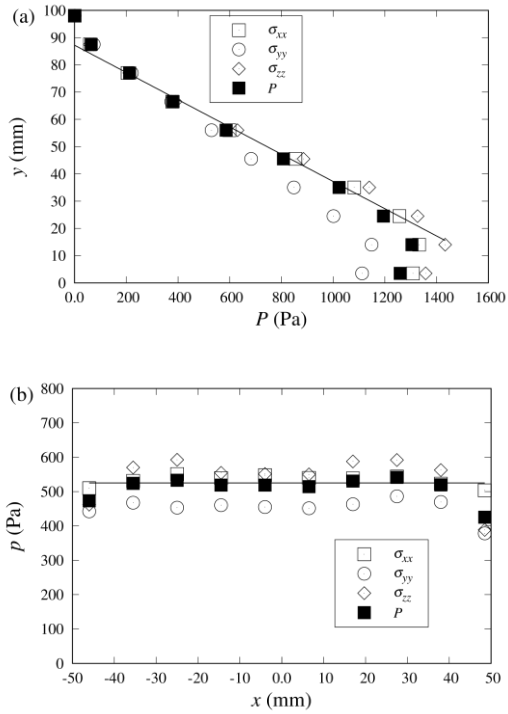

FIG 4.10. (a) Granular pressure profiles in the vibrated bed along the vertical y direction. (b) Granular pressure profiles in the vibrated bed along the horizontal x direction at y = 50 mm.

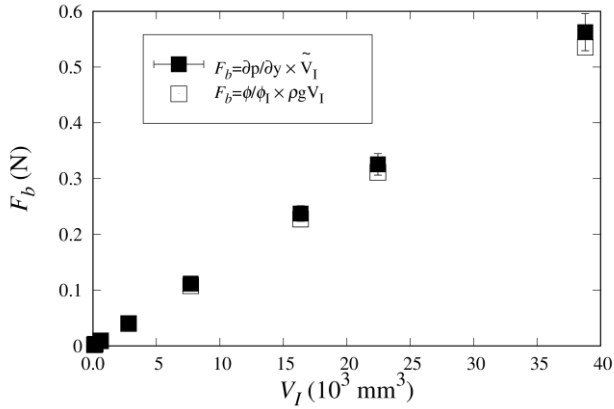

FIG 4.11. Buoyancy force calculated through its hydrostatic definition, Eq. (12), and the generalized Archimedean formulation Eq. (4).

Figure 4.11 plots a comparison between the buoyancy forces computed through the generalized Archimedean formulation, Eq. (4.4) and its hydrostatic definition, Eq. (4.12). The calculated values are very similar, suggesting that using the Voronoi volume as the effective occupied space of the intruder, the hydrostatic definition of the buoyancy force can be applied also to granular systems (using a coarse-graining derived granular pressure). However, the calculation of the buoyancy force though its hydrodynamic definition (Eq. 4.12) is rather cumbersome as it requires coarse graining, while the generalized Archimedean formulation requires only one fitting parameter (for a given system) to calculate accurately the buoyancy force acting on an intruder allowing for an effective computation for practical problems.

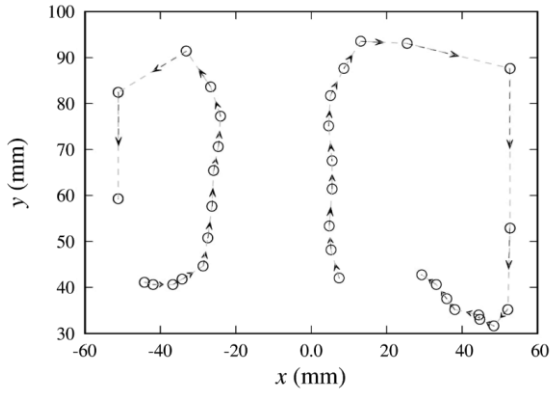

FIG 4.12. Particle trajectories in the *xy* plane starting at $t = 150$ s for $\Gamma = 8.0$. The time interval between two successive trajectory points is equal to 2.5 s. The arrow indicates the moving direction along the time.

So far we have shown that the generalized Archimedean formulation of the buoyancy force is in very good agreement with the calculation through its hydrostatic definition, Eq. (4.12), or its direct numerical measurement via a virtual spring in a convection-free vibrated bed. Now we turn to a more general system in which a convective pattern is present. To formulate a force balance on the intruder an upwards-directed drag force $\mathbf{F}_d$ due to an upwards-directed convection (at the center of the bed) has to be considered, i.e.

$$\mathbf{F}_{lift} = \mathbf{F}_b + \mathbf{F}_d = -(\mathbf{F}_g + \mathbf{F}_s)\,. \tag{4.13}$$

The drag force is obtained by subtracting the buoyancy force from the segregation (lift) force (which is obtained through the virtual spring force Eq. (4.8)). If the generalized Archimedean formulation is also applicable for such convective systems, the granular drag obtained through Eq. (4.13) should match the values obtained through the granular drag model given by Eq. (4.5).

By setting the wall friction coefficient to a non-zero value, a convection pattern is established in the vibrated bed, as the cross sectional area of the bed is not exactly constant over a vibration cycle. To confirm the establishment of a convective patter, randomly selected particles are tracked in the bed. The trajectories are shown in Fig. 4.12 and confirm an upward motion in the center of the bed and a downward motion close to the walls. The lift force in such a

convective system, as determined by Eq. (4.8), far exceeds the buoyancy force calculated through the generalized Archimedean formulation Eq. (4.4) as shown in Figure 4.13. In addition, when normalized by the weight of the intruder the lift force becomes dependent on the intruder size, which distinguishes it from the weight-normalized buoyancy force in a fluid (F_b/m_Ig) which is size independent. As the size ratio of the intruder to the bed particles increases, the weight-normalized, buoyancy force calculated by the generalized Archimedean formulation Eq. (4.4) approaches $F_b/m_Ig = 0.62$ whereby 0.62 is the bulk solid fraction ϕ of the bed, as expected, and $F_b/m_Ig = 1$ for $d_I / d_p = 1$.

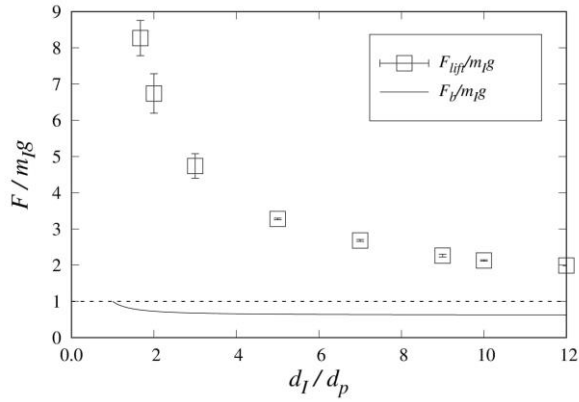

FIG 4.13. (□) Numerically determined (via a virtual spring using Eq. (8)), weight-normalized lift force. The solid line is the weight-normalized buoyancy force F_b/m_Ig determined by the generalized Archimedean formulation, i.e. $F_b = (\phi/\phi_I)\varrho_f g V_I$, where $\phi_I = (\phi - 1)S^c + 1$, with $c = -1.35$ and $\phi = 0.62$ for $\Gamma = 8.0$. The dash line is a reference line which denotes $F/m_Ig = 1$.

We attribute the difference between the virtual-spring derived lift force and the buoyancy force calculated via the generalized Archimedean formulation Eq. (4.4), to the presence of a convective pattern and hence the presence of a drag force that also acts in the vertical direction. When probing the magnitude of the relative velocity between the intruder and the bed particles, an average relative velocity of ~ 0.2 mm/s is determined in the center of the bed, i.e. within the limits of the slow velocity drag regime ($v << 28$ mm/s). In the slow-

velocity regime the drag force is independent of the relative velocity and given by Eq. (4.5) where β is a constant that depends on the restitution coefficient and the shape of the bed particles (Albert et al. 1999). Using the force balance Eq. (4.13), the drag force $\mathbf{F}_d$ can be obtained by subtracting the buoyancy force from the lift force. Subsequently, the granular drag force obtained through Eq. (4.5) can be compared to the drag force determined through Eq. (4.13) and in the case of a good agreement, the lift force acting on an intruder in a convective system can be expressed by:

$$\begin{aligned} F_{lift} &= F_b + F_d \\ &= \frac{\phi}{\phi_I}\rho_p g V_I + \beta\rho_p g(y_b - y)d_I^{\,2}. \end{aligned} \tag{4.14}$$

Indeed, we observe a very good agreement between the drag forces obtained and using a least square fitting method, β was determined as 0.59 (see Figure 4.14).

A conclusion from Eq. (4.14) is that the lift force acting on the intruder is independent of the intruder density, but it depends on the density of the bed particles and the intruder size. To assess the validity of these key observations, we performed additional simulations with a varying intruder density. Figure 4.15 confirms a good agreement between the lift force measured through the virtual spring, i.e. $F_{lift} = F_{spring} + m_I g$ and Eq. (4.14) using $\beta = 0.59$ (β depends on the surface properties of the particles and the shape of the intruder).

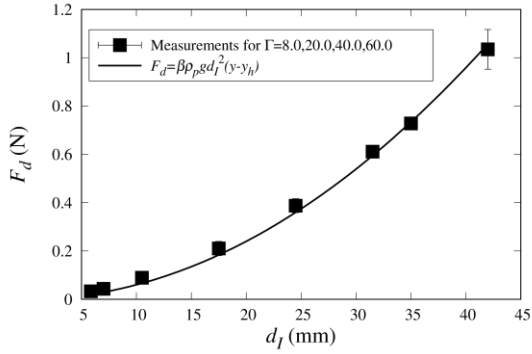

FIG 4.14. (■) Drag force determined by subtracting the buoyancy force from the lift force. The lift force was measured using a virtual spring and is given by Eq. (4.13). The buoyancy force was calculated using the generalized Archimedean formulation, i.e., Eq. (4.4). The solid line gives the granular drag forces determined through $F_d = \beta\rho_p g d_I^2(y-y_h)$ with $\beta = 0.59$.

A further consequence of the formulation of the total lift force following Eq. (4.14) is that in a given system that falls into the slow velocity regime, the lift force is independent of the vibration strength injected by the side wall (Γ increasing from 8 to 60 as shown in Fig. 4.5). This can be rationalized by the fact that for a given intruder size and position within the bed, the buoyancy force is constant as the bulk solid fraction does not vary with increasing vibration strength (Fig. 4.6) and the drag force depends on β which, however, is only a function of the coefficient of restitution and the intruder shape.

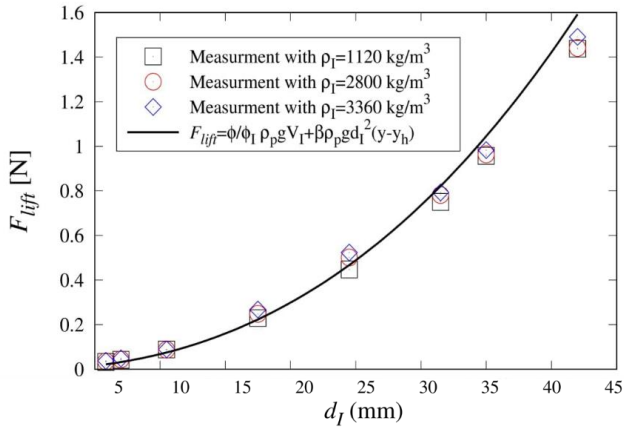

FIG 4.15. Comparison of the lift force predicted by Eq. (4.14) and the lift force obtained numerically by a virtual spring (Eq. 4.8) as a function of the intruder size for different intruder densities ρ_I.

4.4 Conclusion

In this study, we have verified the validity of a generalization of the Archimedean formulation of a granular buoyancy force that has been proposed originally for shear flows for vibro-fluidized systems. To exclude the influence of drag forces, a convection-free system was considered, established through vibrating sidewalls and a friction coefficient of zero for particle-wall contacts. The buoyancy force calculated through the generalized Archimedean formulation, i.e. considering the Voronoi volume of the intruder, agreed very well with the values obtained from its hydrostatic definition (pressure gradient) and its direct measurement through a virtual spring. Subsequently, we have introduced an additional complexity to the system by considering also convection (through a non-zero particle-wall friction coefficient). The segregating (lift) force acting on an intruder in such a system is affected by buoyancy and drag and increases with increasing intruder size, but is independent of the vibration strength Γ (once Γ exceeds 6) and the intruder density. We demonstrate that a lift force model that combines the buoyancy force (expressed through the generalized Archimedean formulation) and a

drag force (velocity-independent in the considered slow-velocity regime) predicts very accurately the value of the lift force obtained through a virtual spring. This model allowed to rationalize the independence of the segregation (lift) force on the intruder density and the vibration strength (once a critical value of $\Gamma_{cr} = 6$ is exceeded). We hope that our work can pave the way to the development of segregation models that allow to quantitatively describe more complex systems, containing e.g., multiple intruders and/or more complex drag force regimes.

LIFT FORCE ACTING ON AN INTRUDER IN DENSE, GRANULAR SHEAR FLOWS

5

Adapted from Liu, M., & Müller, C. R. (2021). Lift force acting on an intruder in dense, granular shear flows. *Physical Review E*, *104*(6), 064903.

5.1 Abstract

We report a new lift force model for intruders in dense, granular shear flows. Our derivation is based on the thermal buoyancy model of Trujillo and Herrmann (2003) , but takes into account both granular temperature and pressure differences in the derivation of the net buoyancy force acting on the intruder. In a second step, the model is extended to take into account also density differences between the intruder and the bed particles. The model predicts very well the rising and sinking of intruders, the lift force acting on intruders as determined by discrete element model (DEM) simulations and the neutral-buoyancy limit of intruders in shear flows. Phenomenologically, we observe a cooling upon the introduction of an intruder into the system. This cooling effect increases with intruder size and explains the sinking of large intruders. On the other hand, the introduction of small to mid-sized intruders, i.e. up to 4 times the bed particle size, leads to a reduction in the granular pressure compared to the hydrostatic pressure, which in turn causes the rising of small to mid-sized intruders.

5.2 Introduction

Since the first report by Brown (1939), segregation effects in granular systems have received widespread interest among both physicists and engineers owing to their high practical relevance. Particles of different sizes (Rosato et al. 1987), densities (Burtally, King, and Swift 2002) and possibly also shapes (Lu and Muller 2020) segregate when excited e.g. via vibration, rotation or gas injection. Segregation is readily encountered in many processing apparatuses such as

rotating cylinders (Hill, Caprihan, and Kakalios 1997), hoppers (Janda et al. 2009) or vibrated beds (Rosato et al. 1987). In industrial applications segregation is typically an undesirable effect as it counteracts mixing. In addition, segregation in granular media is also commonly observed in nature, e.g. rock avalanches and debris flow (Bartelt and McArdell 2009; Crosta, Chen, and Lee 2004). Arguably, model systems in which one or multiple intruders are immersed in a granular bed have been studied most frequently and, in such systems, the so-called "Brazil nut phenomenon" (BNP) has been reported. In the BNP, which is not limited to single intruders, a larger particle rises through a bed of smaller particles under external excitation, typically vibration. Depending on the regularity of the vibrational excitation, the BNP has been explained by percolation (Rosato et al. 1987; Duran, Rajchenbach, and Clément 1993) or convection (Knight, Jaeger, and Nagel 1993b). The percolation model explains the rising of a larger intruder through a bed of smaller particles via a void filling mechanism. During a vibration cycle first a void is formed underneath the intruder. This void is subsequently filled by the small, surrounding bed particles. At the end of a vibration cycle the intruder falls back to a higher rest position. Through a geometric description of the percolation model, Duran, Rajchenbach, and Clément (1993) predicted that the rise velocity of the intruder depends on the size ratio of the intruder to the bed particles. For very regular vibrations a convective flow field is established that carries the intruder upwards until it reaches the surface of the bed. The intruder is trapped at the surface as the region close to the walls where downwards motion occurs is typically smaller than the intruder. In this model, the rise velocity of the intruder is independent of the ratio of the size of the intruder to the bed particles. Although, the two models described above provide some conceptual understanding of segregation in granular media, there is still considerable debate on how to model segregation from a continuum perspective. Such continuum models require formulations of the granular counterparts of drag, buoyancy, and in specific cases the Saffman forces.

Using discrete element method (DEM) simulations, Shishodia and Wassgren (2001) were among the first to establish an expression for the buoyancy force in a granular system. In their 2D vibro-fluidized bed simulations, periodic boundary conditions were employed to eliminate the contribution of convection. In the absence of a convective pattern the intruder was found to

rise to an equilibrium position within the bed (bed position y), instead of rising to the top. Making an analogy to the fluid mechanic description of the buoyancy force, i.e. the product of a pressure gradient and the intruder volume they proposed the following expression for the buoyancy force, F_b:

$$\mathbf{F}_b = \nabla P(y) V_I = -m_I \mathbf{g}\,, \tag{5.1}$$

where $m_I\mathbf{g}$ is the weight of intruder, $\nabla P(y)$ is the pressure gradient and V_I is the intruder volume.

It is worth noting that the 2D granular system investigated by Shishodia and Wassgren (2001) was in the granular gas regime in which binary particle collisions dominate. When considering practically more relevant dense granular systems in which multi-particle collisions and long-lasting contacts dominate, the buoyancy force predicted through Eq. (5.1) underestimates the measured buoyancy force acting on the intruder when the intruder size approaches the size of the bed particles (Huerta et al. 2005).

On the other hand, Trujillo and Herrmann (2003) developed a granular buoyancy model using the kinetic theory of granular gases. The system considered contained a single intruder in a vibrated bed. The driving force acting on the rising intruder was modelled as a thermal-induced buoyancy force, i.e., a density difference arising from differences in the granular temperature of the system with and without the intruder. In their model, a reference state "0" was defined that is characterized by a granular pressure $P_0(\mathbf{r})$ and temperature $T_0(\mathbf{r})$, where $\mathbf{r}$ is the position of the intruder. The reference state assumes a bed without the intruder. Upon introduction of the intruder, the bed transitions to a new state "1" which is characterized by $P_1(\mathbf{r})$ and $T_1(\mathbf{r})$. The temperature difference between the "perturbed" and reference states is given as $\Delta T(\mathbf{r}) = T_1(\mathbf{r}) - T_0(\mathbf{r})$, yielding the following expression for a granular, thermally-induced buoyancy force (Trujillo and Herrmann 2003):

$$F_b = \alpha \Delta T \rho V_I g\,, \tag{5.2}$$

with ρ being the bulk density of the reference state (i.e. $\rho = \rho_p \phi$ with ρ_p being the density of the bed particles and ϕ being the solid fraction of the bed), g is

the acceleration due to gravity and a is the coefficient of thermal expansion, defined as $\alpha = -\frac{1}{n}\left(\frac{\partial n}{\partial T}\right)_P$, where n is the number density of the bed particles. Assuming a to be constant, Trujillo & Herrmann showed that $a = \frac{1}{T_0} C(\phi)$, where $C(\phi)$ depends on the solid fraction with $C(\phi) \rightarrow 1$ for $\phi \rightarrow 0$. The system considered by Trujillo and Herrmann (2003) was a vibro-fluidized bed and a uniform system pressure i.e. $dP \sim 0$ was assumed. However, such a simplification would not be valid in dense, shear systems (*vide infra*).

To summarize, the buoyancy models described in Eq. (5.1) and Eq. (5.2) are been developed for systems that operate in the granular gas regime. However, when considering more "liquid-like", dense granular systems additional effects have to be considered in the buoyancy model. For example, in an experimental study of a dense, vertically vibrated bed (amplitude A = 9.76 mm and frequency f = 9.7 Hz) Shinbrot and Muzzio (1998) observed that intruders (d_I = 152 mm) with a density < $0.5\varrho_p$ sink, whereas heavy intruders (d_I =152 mm) with a density in the range 1.2-1.7ϱ_p rise. This unexpected behaviour has been termed reverse Brazil nut phenomenon (RBNP). As the intruder size was fixed in these two experiments, the buoyancy model described in Eq. (5.1) cannot explain why the heavier intruder rises to the top while the lighter intruder sinks. It has been argued that the interstitial air in beds of small particles (< 800 μm) might contribute to the RBNP (Shinbrot and Muzzio 1998) . To weaken the influence of the interstitial gas in a vibrated bed, Huerta et al. (2005) investigated the BNP in a dense bed containing larger particles (i.e. a mixture of glass beads of 3 and 4 mm in diameter). Huerta et al. (2005) observed that a light intruder rises faster than a heavier intruder of equal size. Unlike in the setup of Shinbrot and Muzzio (1998), the bed of Huerta et al. (2005) was vibrated horizontally with neighbouring sidewalls vibrating with the same amplitude but out of phase (phase shift π), ensuring the cross sectional area of the bed to remain almost constant over a vibration cycle and avoiding in turn the establishment of a convection pattern. Huerta et al. (2005) measured the lift force acting on the intruder by connecting the intruder, placed in the centre of the bed, with a force sensor. The measured lift force $\mathbf{F}_{\text{lift}} = -(\mathbf{F}_s + \mathbf{F}_g)$, where $\mathbf{F}_g$ is the gravitational force of intruder and $\mathbf{F}_s$ is the time averaged value obtained from the force sensor, that can be interpreted as the buoyancy force acting on the intruder. The measured lift force was fitted to a generalized Archimedean formulation of the buoyancy force, viz:

$$F_b = \left|\mathbf{F}_s + \mathbf{F}_g\right| = \rho_p \phi V_I g\,, \tag{5.3}$$

where the "fitting constant" ϕ was very close to the average solid fraction of the bed, i.e. the intruder rises as in a fluid with a density that is equal to the bulk density of the granular media ($\phi\rho_p$). However, the experimental data acquired by Huerta et al. (2005) showed only good agreement with the buoyancy model given by Eq. (5.3) for large ($d_I/d_p > 4$) and very light intruders ($\rho_I/\rho_p = 0.0169$). As the intruder size approached the size of the bed particles, the measured buoyancy force exceeded the predictions of the generalized Archimedean principle given in Eq. (5.3). In a convection-free, vibrated bed in which the intruder is fixed in an equilibrium position and only buoyancy and gravity forces are acting on the intruder, the buoyancy force will become smaller than the bed particle weight for $V_I \to V_p$, i.e. $F_b = \phi\rho_p V_p g < m_p g$ as the solid fraction of the bed $\phi < 1$. Thus, the generalized Archimedean principle expressed in Eq. (5.3), underestimates the buoyancy force acting on a bed particle. This limitation of the buoyancy model given in Eq. (5.3) has also been remarked by van der Vaart et al. (2018).

Although the buoyancy concept was investigated initially in vibrated systems, its applicability to shear flow systems of practical relevance has also been studied. Qualitatively, Savage and Lun (1988) proposed that in dense shear flows segregation is driven by both kinetic sieving and squeeze expulsion. Overall, there is a higher probability of finding a void into which a small particle can fall compared to a void into which a large particle can fall. This size-dependent, gravity induced segregation mechanism has been termed "random fluctuating sieving" or "kinetic sieving". In addition, a force imbalance on a particle leads to the particle being squeezed out of its layer. This mechanism was termed "squeeze expulsion", but it is neither necessarily size dependent nor does it has a preferred direction. However, there is currently no continuum model that describes accurately the motion of segregating intruder(s) in dense, granular shear flows. To gain some insight into these systems, Guillard, Forterre, and Pouliquen (2016) performed 2D, steady-state, shear flow simulation using DEM to quantify the lift force acting on an intruder as a function of the prevailing pressure (and stress) gradient. The size of the intruder was varied from d_p to $10d_p$ while fixing the intruder density to the density of the bed particles. In their simulations, the intruder

was kept at a position of half the height of the bed ($h_c/2$) by connecting it to a virtual spring. The virtual spring imposed an additional (spring) force onto the intruder, i.e. $\mathbf{F}_s = -k_s(y_1 - y_0)\mathbf{e}_y$, where k_s is the spring constant, y_1 is the vertical position of the intruder at a given time and $y_0 = h_c/2$ is the initial position of the intruder, $\mathbf{e}_y$ is the unit vector in the y direction. The virtual spring ensures the intruder to remain at its equilibrium position while allowing its free movement along the direction of the flow. The buoyancy force acting on the intruder was calculated in analogy to Eq. (5.1) and expressed as a function of the spatial gradients of the granular pressure and shear, viz:

$$F_{lift} = -\frac{\pi d_I^{\,2}}{4}\left(\mathcal{F}\left(\mu, d_I/d_p\right)\frac{\partial p}{\partial y} + \mathcal{G}\left(\mu, d_I/d_p\right)\frac{\partial|\tau|}{\partial y}\right), \tag{5.4}$$

where τ is the granular shear stress, P is the granular pressure, and $\mu = |\tau|/P$ is the bulk friction coefficient. Guillard, Forterre, and Pouliquen (2016) proposed the factors $\mathcal{F}$ and $\mathcal{G}$ to be exponential functions of μ and d_I/d_p.

In a subsequent study, van der Vaart et al. (2018) aimed to elucidate whether the lift force acting on an intruder in a shear flow can be expressed as the sum of a granular buoyancy force and a Saffman-type lift force, i.e.

$$F_{lift} = F_b + F_{saff}, \tag{5.5}$$

where $F_{saff} = -a_0 b_0 I_\theta \mu^{0.5}(d_p/d_I - 1) d_I^2 d_p^{-1}\mathrm{sgn}(\dot{\gamma})$ (a_0 and b_0 are fitting constants, $I_\theta = \dot{\gamma} d_p/(P/\varrho_p)^{0.5}$, $\dot{\gamma}$ is the shear rate and μ is the bulk friction coefficient). van der Vaart et al. (2018) considered a full 3D, dense shear flow along an inclined plane with an inclination angle θ with respect to the horizontal direction. Van der Vaart et al. (2015) modified Eq (5.3) to correct for the underestimation of the buoyancy force for $V_I \to V_p$ by replacing the solid fraction of the bed, ϕ, by ϕ/ϕ_I where ϕ_I is the solid fraction of the intruder, yielding,

$$F_b = \rho_p \frac{\phi}{\phi_I} V_I g. \tag{5.6}$$

The solid fraction of the intruder is defined as the ratio of its Voronoi volume, $\widetilde{V}_I$ to its physical volume V_I. The modified buoyancy model Eq. (5.6) has been also recently assessed and validated in a vibro-fluized system (Kiani Oshtorjani, Meng, and Müller 2021). The derivation of the Saffman lift force is limited to conditions where inertia is not dominating the local flow around the intruder, i.e. when the shear rate-based Reynolds number Re $\ll$ 1. Furthermore, it is currently unclear whether the Saffman lift force model also holds for very large intruders which have been found to sink (Thomas 2000).

In the most recent work, Jing et al. (2020) reported a simple buoyancy based model to describe the lift force acting on a single spherical intruder in a dense, granular shear flow. By varying the size and density ratio of the intruder to bed particles, it was found that the lift force F_{lift}, as determined via a virtual spring, i.e., $\mathbf{F}_{\text{lift}} = -(\mathbf{F}_s+\mathbf{F}_g)$, collapses onto an Archimedean-type model, viz:

$$F_b = f(D)\rho_p\phi V_I g\,, \tag{5.7}$$

where $f(D) = (1-c_1\exp(-D/a_1))(1+c_2\exp(-D/a_2))$ is a fitting function with fitting constants $c_1 = 1.43$, $c_2 = 3.55$, $a_1 = 0.92$, $a_2 = 2.94$ and $D = d_I/d_p$. As for $D >> 1$, $f(D) \rightarrow 1$, the observation that with increasing D the lift force approaches the generalized Archimedean principle (Eq. (5.3)) is captured by Eq. (5.7). This trend of the buoyancy force for D >> 1 which can be considered as the continuum limit, can be explained as follow. As the surface area of the intruder increased with D^2 the number of contacts between the intruder and the surrounding bed particles increases rapidly with increasing D, yielding a uniform stress transmission to the intruder for D >> 1 and hence a similar behaviour as an intruder immersed into a fluid. On the other hand, for $D \rightarrow 1$, the stress distribution on the intruder is highly anisotropic leading to a deviation from Eq. (5.3). However, the effect of stress anisotropy on the lift force acting on an intruder remains largely unclear. Nonetheless, despite the empirical derivation of $f(D)$, Eq. (5.7) can be of practical importance allowing to make an *a priori* prediction whether an intruder of a given size and density ratio will sink or rise.

To summarize, recent works have improved significantly our understanding of size-driven segregation of intruders in dense shear flows and its continuum

modelling. However, although several works observe a distortion of the hydrostatic pressure field, in addition to the granular temperature field, upon the addition of the intruder, the model of Trujillo and Herrmann (2003) is limited to disturbances in the temperature field, which is most likely insufficient to describe dense granular systems. Furthermore, while the theoretical models have been shown to predict well the forces acting on intruders for lower ratios of d_I/d_p (e.g. $d_I/d_p < 4$ for van der Vaart et al. (2018)), theoretical models that can also predict accurately the sinking of very large intruders would be advantageous. Hence, in this work we aim to extend the original work of Trujillo and Herrmann (2003) to dense shear flow systems by describing local perturbations in both the pressure and temperature field upon the introduction of an intruder. Compared to existing models for the lift force acting on an intruder, the model proposed here is based on a physical description of the granular system. The proposed model does not only predict quantitatively the lift force acting on the intruder, but also provides insight into the mechanisms at play.

5.3 Method

A. Simulation Method

DEM simulations of the shear flow system considered here were performed using the LIGGGHTS software (Kloss et al. 2012). In DEM, each particle is modelled as a single entity (Lagrangian approach) and the normal, $F_{n,ij}$, and tangential contact forces, $F_{t,ij}$, acting between the contacting particles i and j are modelled by a Hertzian contact model (Tsuji, Tanaka, and Ishida 1992; Antypov and Elliott 2011):

$$F_{n,ij} = -k_n \sqrt{\frac{1}{4R^*}} \delta_{n,ij}^{3/2} + \gamma_{n,ij} \sqrt{m^*} \sqrt[4]{\frac{\delta_{n,ij}}{4R^*}} u_{n,ij}, \tag{5.8}$$

$$F_{t,ij} = -k_t \sqrt{\frac{1}{4R^*}} \delta_{n,ij}^{1/2} \delta_{t,ij} + \gamma_{t,ij} \sqrt{m^*} \sqrt[4]{\frac{\delta_{t,ij}}{4R^*}} u_{t,ij}, \tag{5.9}$$

where k_n and k_t are the spring constants in the normal and tangential direction, respectively. Here, δ_n and δ_t are the particle overlaps in, respectively, the normal and tangential direction, γ_n and γ_t are the damping coefficients in, respectively, the normal and tangential direction, R^* is the effective radius given as $R^* = R_iR_j/(R_i+R_j)$, $m^* = m_im_j/(m_i+m_j)$ and $u_{n,ij}$ and $u_{t,ij}$ are the tangential and normal relative velocities between particles i and j, respectively. The tangential contact force, $F_{t,ij}$, is limited by Coulomb's law, i.e. $F_{t,ij} \leqslant \mu F_{n,ij}$ with μ being the coefficient of friction.

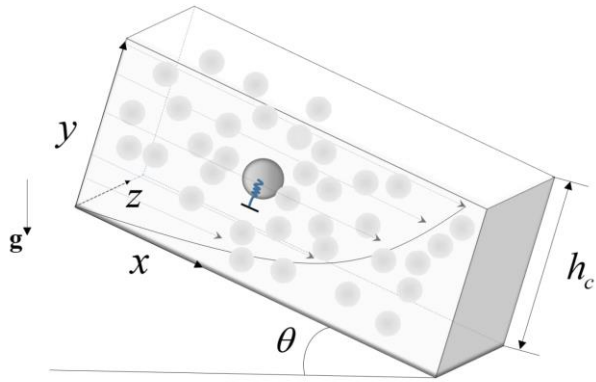

FIG 5.1. Sketch of the granular shear flow system under investigation. An intruder (dark grey) is immersed in the bed at an initial location $y_0 = h_c/2$. The inclination angle is given by θ and h_c is the distance (in the y-direction) from the bottom of the bed to its surface. For simplicity we introduce a local coordinate system. A virtual spring (blue spring) is attached to the intruder. The intruder is able to move freely in the $x\text{-}z$ plane, while it reaches a (dynamic) equilibrium position y_1. The size of the simulation domain is $l_x \times l_z \times h_c = 20d_p \times 20d_p \times 40d_p$.

We have chosen to study inclined plane flow as it is one of the classical setups, having well established flow dynamics (Silbert et al. 2001). Figure 5.1 illustrates the set-up of the simulation domain. The bed of dimensions $l_x \times l_z \times h_c = 20d_p \times 20d_p \times 40d_p$ consists of 16'000 bed particles of diameter d_p. We have confirmed that the computational domain is adequately sized since doubling its size had no effect on the numerical results. The bed particles flow along

an inclined plane due to gravity. The gravitational vector $|g| = 9.81$ m/s^2 can be decomposed into $g_x = g\sin\theta$ and $g_y = g\cos\theta$. Particles with a diameter $d_w = 10$ mm are glued onto the bottom plate to increase the roughness of the bottom wall. In the x and z direction, periodic boundaries were applied to establish a steady-state shear flow. The velocity profiles in the shear flow were varied by adjusting the inclination angle θ. However, as only a narrow range of θ ensures steady-state conditions, the chute angle θ was only varied in the range $24^\circ \leq \theta \leq 28^\circ$ in this work. The incline chute flow is chosen as its well established dynamics. A spherical intruder of diameter d_I was placed inside the bed at a vertical position $y_c = h_c/2 = 20d_p$. The motion of the intruder in the y-direction was constrained by a virtual spring (spring constant 80 N/m). The spring constant has been varied by a factor of four and we have observed a negligible effect on the lift force. The intruder can move freely in the xz plane. The spring force acting on the intruder is determined through its displacement in the y direction, i.e. $\mathbf{F}_s = -k_s(y-y_0)\mathbf{e}_y$. The vertical displacement of the intruder is very small, at most $0.5d_p$ for $d_I/d_p = 8$. The lift force acting on the intruder is then given by $\mathbf{F}_{\text{lift}} = -(\mathbf{F}_s+\mathbf{F}_g)$. The parameters used in the DEM simulation are given in Table 5.1. The reported parameters correspond to the material properties of glass, except for the particle spring constant for which a lower value was chosen to accommodate DEM simulation constraints.

Table 5.1: Parameters used in the DEM simulations

Parameters	Value
k_n (N/m)	6.41×10^4
k_t (N/m)	2/7 k_n (Silbert et al. 2001)
d_p (mm)	5
d_I (mm)	d_p up to ~ $8d_p$
d_w (mm)	10
ϱ_p (kg/m^3)	2500
γ_n ((N/m)$^{1/2}$)	23.01 (Silbert et al. 2001)
γ_t ((N/m)$^{1/2}$)	1/2 γ_n
μ	0.5
e	0.88
Time step (s)	10^{-5}

B. Coarse Graining

To obtain the granular pressure, stress and temperature, coarse graining (CG) of the DEM data was employed(Goldenberg et al. 2006). The granular stress tensor in the coarse graining volume is given by (Andreotti, Forterre, and Pouliquen 2013):

$$\sigma_{\alpha,\beta}(\mathbf{r},t) = -\frac{1}{2}\sum_{i,j} f_{\alpha,ij} r_{\beta,ij} \int_0^1 \Phi\left(r - \mathbf{r}_i + s\mathbf{r}_{ij}\right) ds \\ -\sum_{i=1}^{N} m_i \Phi\left(\mathbf{r} - \mathbf{r}_i\right) u'_{\alpha,i} u'_{\beta,i}, \tag{5.10}$$

where Φ is the coarse graining function, i,j denotes the Cartesian components, $f_{a,ij}$ is the α th component of the contact force vector between particles i and j (see illustration in Figure 5.2) and $r_{\beta,ij}$ is the branch vector connecting the centers of gravity of particles i and j. We use the Heaviside function as the coarse graining function, i.e. $\Phi(\mathbf{R}) = 1/(4/3\pi w^3)\mathrm{H}(w - |\mathbf{R}|)$, where w is the radius of the spherical coarse graining volume, $\mathbf{R} = \mathbf{r} - \mathbf{r}_i$ is the vector pointing from a sampling particle inside the coarse graining volume to the center ($\times$) of the coarse graining volume and $u'_{i,a}$ is the velocity fluctuation of particle i, viz. $u'_{i,a} = u_{i,a} - \overline{u_\alpha}$ where $u_{i,a}$ is the instantaneous velocity of particle i in the a th direction and $\overline{u\alpha}$ is the average velocity in the a th direction of the particles in the coarse graining volume.

The average pressure in the coarse graining volume is given by $P = 1/3(\sigma_{\alpha\alpha} + \sigma_{\beta\beta} + \sigma_{\chi\chi})$. The value of $\sigma_{\alpha,\beta}$ mainly depends on the coarse graining radius w. For example, Figure 5.3(a) shows the dependence of σ_{yy} on the coarse graining radius w. For $w/d_p < 1$, σ_{yy} increases with increasing w/d_p, but reaches an asymptotic value for $w/d_p \geq 1$, in agreement with previous works (Weinhart et al. 2013; Goldenberg et al. 2006). To avoid an over-smoothing of the local stresses we chose $w = \bar{d} = 1/2(d_l + d_p)$, in agreement with previous works

(Weinhart et al. 2016; Tunuguntla, Weinhart, and Thornton 2017; van der Vaart et al. 2018)

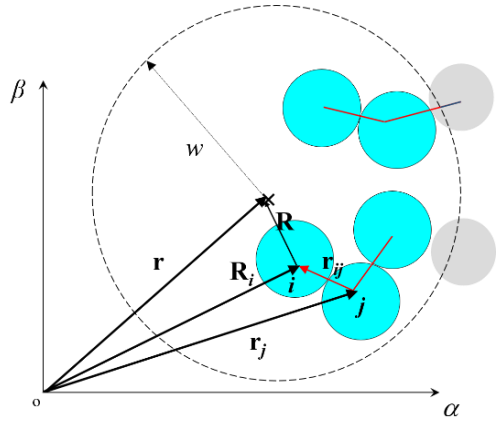

FIG 5.2. Illustration of the coarse graining method. The coarse graining volume is bounded by a spherical space centred at **r** with the coarse graining radius *w*. The branch vector $\mathbf{r}_{ij} = \mathbf{r}_i - \mathbf{r}_j$ is shown as a red arrow that points from particle *j* to particle *i*.

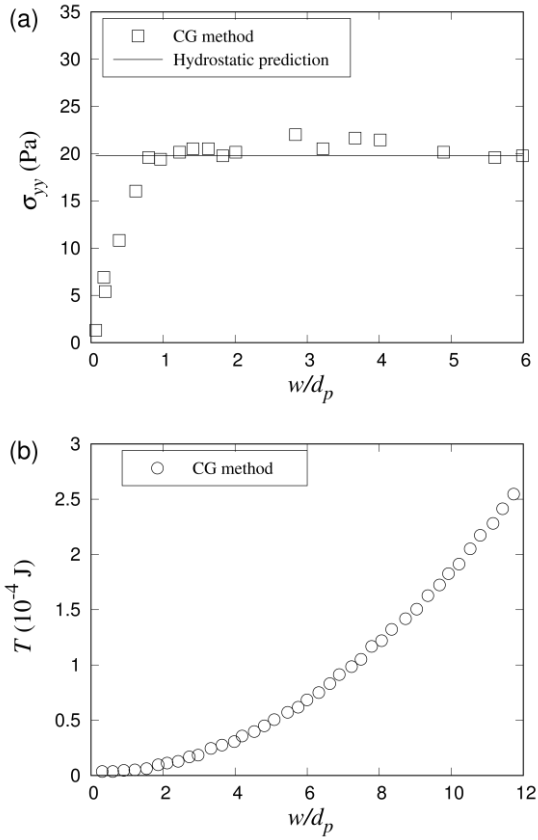

FIG 5.3. Dependence of σ_{yy} and the granular temperature on the normalized coarse graining radius w/d_p: (a) σ_{yy} increases with increasing w/d_p for $w/d_p < 1$. For $w \geq d_p$, σ_{yy} reaches an asymptotic value that is in excellent agreement with its hydrostatic value, i.e. $Nm_pg/(lx \cdot lz)$, where N is the particle number, m_p is the particle mass and $lx \cdot lz$ is the cross-sectional area of the system. (b) The granular temperature increases continuously with increasing coarse graining radius w/d_p.

Turning now to the granular temperature, viz. (Haff 1983; Trujillo and Herrmann 2003)

$$\frac{3}{2}T = \frac{1}{N}\sum_{i=1}^{N}\frac{1}{2}m_i(u_{i,\alpha}^{'2} + u_{j,\beta}^{'2} + u_{i,\chi}^{'2}), \tag{5.11}$$

where α, $\beta$and χ denotes the Cartesian components, $u'_{i,a}$, $u'_{i,\beta}$, $u'_{i,\chi}$ are, respectively, the velocity fluctuations of particle i with regards to the respective average velocity in the coarse graining volume. The magnitude of the granular temperature depends on the coarse graining volume. For example, in the dense granular shear flow system studied here, the granular temperature increases monotonically with increasing coarse graining volume (FIG 5.3. (b)). Recently, a method has been proposed to eliminate the influence of the coarse graining volume on the granular temperature, however, the approach is only suitable for very specific systems such as monodisperse shear flows (Weinhart et al. 2013). However, as this work concentrates on the effect of a differently sized granular intruder on the granular temperature of the system when compared to the intruder-free reference case, this method is not applicable to the system studied here. Generally, there is very little consensus on the "correct" coarse graining radius for the granular temperature and Glasser and Goldhirsch (2001) emphasize to clearly state the coarse graining radius that has been chosen to calculate the granular temperature for a given problem. In the work of Trujillo and Herrmann (2003) a coarse graining radius of $w = L/3$ (L is the width of the vibrating bed) was chosen for the granular temperature calculation to achieve a good agreement between their thermal buoyancy model and the experimental measurements. Here, we have decided to use the coarse graining radius $w = r_1 + d_p$ for the granular temperature, as it is physically reasonable to include the first layer of particles around an intruder into the coarse graining radius.

5.4 Model Description

Herrmann (1993) proposed a thermodynamic formulation for moving granular media that was subsequently adopted to investigate the BNP problem (Trujillo and Herrmann 2003). First, they defined a reference state of a vibro-fluidized bed that is described by a given granular pressure $P_0(\mathbf{r})$ and granular temperature $T_0(\mathbf{r})$. When introducing an intruder into the system, the state at $\mathbf{r}$ changes and is referred to as a perturbed state "1" described by the granular

pressure $P_1(\mathbf{r})$ and granular temperature $T_1(\mathbf{r})$. Trujillo and Herrmann (2003) argued that the perturbed granular system tends to re-establish its reference state, leading to a displacement of the intruder from its initial position $\mathbf{r}$. Neglecting changes in the granular pressure due to the presence of the intruder, Trujillo and Herrmann (2003) proposed a thermal-driven buoyancy force model (Eq. (5.2)) to describe the motion of an intruder in a vibro-fluidized bed.

In the following we derive a granular buoyancy model that takes into account also intruder-induced variations in the pressure field to allow the description of the motion of an intruder in a dense, granular shear flow system.

To quantify the impact of an intruder on the local granular temperature and pressure in a shear flow, we consider the two systems (i.e., the reference and perturbed states) illustrated in Figure 5.4 (b) except that the intruder is replaced by bed particles. In the reference case, the granular temperature and pressure at $\mathbf{r}$ (i.e., the center of the imaginary control volume) are referred to as $T_0(\mathbf{r})$ and $P_0(\mathbf{r})$, respectively. Similarly, in the intruder case the granular temperature and pressure at $\mathbf{r}$, i.e., the position where the intruder is located, are denoted as $T_1(\mathbf{r})$ and $P_1(\mathbf{r})$, respectively. $P_0(\mathbf{r})$, $T_0(\mathbf{r})$, $P_1(\mathbf{r})$ and $T_1(\mathbf{r})$ are determined through coarse graining. The change in the system due to the presence of an intruder (compared to the reference state) is described by $\Delta T(\mathbf{r}) = T_1(\mathbf{r}) - T_0(\mathbf{r})$ and $\Delta P(\mathbf{r}) = P_1(\mathbf{r}) - P_0(\mathbf{r})$. We follow now the argumentation of Trujillo and Herrmann (2003) that the thermodynamic driving force for an intruder to sink or rise (i.e. the lift force acting on the intruder) is related to $\Delta T(\mathbf{r})$ and $\Delta P(\mathbf{r})$. As in our shear flow system periodic boundary conditions are applied in the x and z directions, $P(\mathbf{r})$ and $T(\mathbf{r})$ are independent of x and z for a given y, allowing us to simplify our notation to $P(y)$ and $T(y)$.

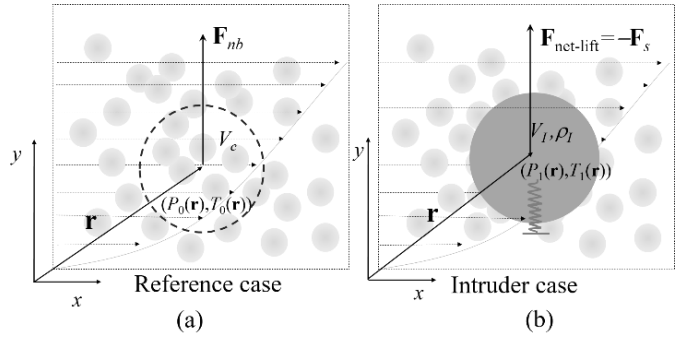

FIG 5.4. Illustration of the reference case and the perturbed state, i.e. the shear flow system with the presence of an intruder. (a) Reference case: Shear flow system without the intruder. The intruder is replaced by an imaginary control volume of size $V_c = V_I$, that is filled with bed particles. The boundary of the imaginary control volume is given by a dashed circle. Here, $P_0(\mathbf{r})$ and $T_0(\mathbf{r})$ denote the reference state at **r.** (b) Perturbed state: Intruder of volume V_I and density ϱ_I is placed at **r** into the shear flow system. $P_1(\mathbf{r})$ and $T_1(\mathbf{r})$ are the granular pressure and temperature at **r** in the perturbed state. $\mathbf{F}_{nb}$ is the net buoyancy force acting on the control volume which arises from the temperature and pressure difference between the reference and intruder states. $\mathbf{F}_{\text{net-lift}}$ is the force acting on the intruder, which is measured by the (virtual) spring force, $\mathbf{F}_{\text{net-lift}} = -\mathbf{F}_s$ and that keeps the intruder in its equilibrium position. Here, "net" implies that the gravitational force has been subtracted.

For an inelastic, hard-sphere system (Figure. 5.4(a)) the granular pressure can be expressed as(Bocquet et al. 2001; Garzó and Dufty 1999):

$$P = nT\left(1+\frac{\pi}{3}(1+e)nd_p^3C(\phi)\right), \tag{5.12}$$

where n is the particle number density, T is the granular temperature, e is the coefficient of restitution, d_p is the diameter of the particles, ϕ is the solid fraction, $C(\phi)$ is the pair correlation function at a contact, i.e., the probability

density to find another particle at a distance d_p from a particle center. For a dilute or moderately dense system (i.e. $nd_p^3 \sim 1$), the expression of Carnahan-Starling holds, i.e. $C(\phi) = (2-\phi)/2(1-\phi)^3$ (Andreotti, Forterre, and Pouliquen 2013) where Carnahan-Starling assumes that binary collisions dominate. This assumption might become inaccurate for denser systems, in which empirical pair correlation functions $C(n)$ that consider multiple particle contacts (as opposed to binary contacts in a granular gas) are required(Jenkins and Berzi 2010; Kumaran 2015). However, for our model the exact form of Eq. (5.12) is not relevant as we only utilize the finding that there is a relationship $P = P(n,T)$ and $P = P(n,T)$ can be re-formulated as:

$$n = n(P,T)\,. \tag{5.13}$$

Taking the total differential yields

$$dn = (\frac{\partial n}{\partial T})dT + (\frac{\partial n}{\partial P})dp = -\alpha n dT + k_p n dP\,, \tag{5.14}$$

where α is the thermal expansion coefficient and k_p is the compressibility coefficient, given by

$$\alpha = -\frac{1}{n}(\frac{\partial n}{\partial T})_P\,, \tag{5.15}$$

and

$$k_p = \frac{1}{n}(\frac{\partial n}{\partial P})_T\,. \tag{5.16}$$

Placing an intruder in the reference shear flow system changes the granular pressure and temperature at position **r** from (T_0, P_0) to (T_1, P_1). Assuming a and k_p to be constant and integrating Eq. (5.14) we obtain

$$n_1 = n_0 e^{-(\alpha\Delta T + k_p \Delta P)}\,, \tag{5.17}$$

where $n_0 = N_0 / V_c$ is the number density in the reference case (N_0 is the number of particles in the imaginary control volume V_c). The density of the control volume can be expressed as $\varrho_0 = (N_0 m_p)/V_c = n_0 m_p$, where m_p is the mass of a bed particle. Using the equivalent expression for ϱ_1, i.e., $\varrho_1 = n_1 m_p$, we can rewrite Eq. (5.17) yielding:

$$\rho_1 = \rho_0 e^{(-\alpha \Delta T + k_p \Delta P)}. \tag{5.18}$$

Hence, transitioning from state "0" to "1" leads not only to a change in the granular temperature and pressure (ΔT and ΔP) at position **r**, but also to a change in density i.e., $\Delta\varrho = (\varrho_0 - \varrho_1)$. We now make the further assumption that the bulk density outside the control volume region (Figure 5.4 (a)) is unaffected by the pressure/temperature perturbation (i.e., it is ϱ_0). Following Archimedean's principle, we define the net buoyancy force acting on the imaginary control volume in Figure 5.4(a) as:

$$F_{nb} = (\rho_0 - \rho_1) V_I g_y. \tag{5.19}$$

As our derivation starts from Eq. (5.12), which only holds for monodisperse particle systems, the net buoyancy force given in Eq. (5.19) that is acting on the imaginary control volume in Figure 5.4(a) is not expected to be the exact equivalent of the lift force acting on the intruder, but it is expected that there exists a strong correlation between F_{nb} and $F_{\text{net-lift}}$ which will be demonstrated in the following.

Substituting Eq. (5.18) in Eq. (5.19), and replacing ϱ_0 with $\varrho_p \phi$ we obtain the following expression for the net buoyancy force:

$$F_{nb} = (1 - e^{-\alpha \Delta T + k_p \Delta P}) \rho_p \phi V_I g_y. \tag{5.20}$$

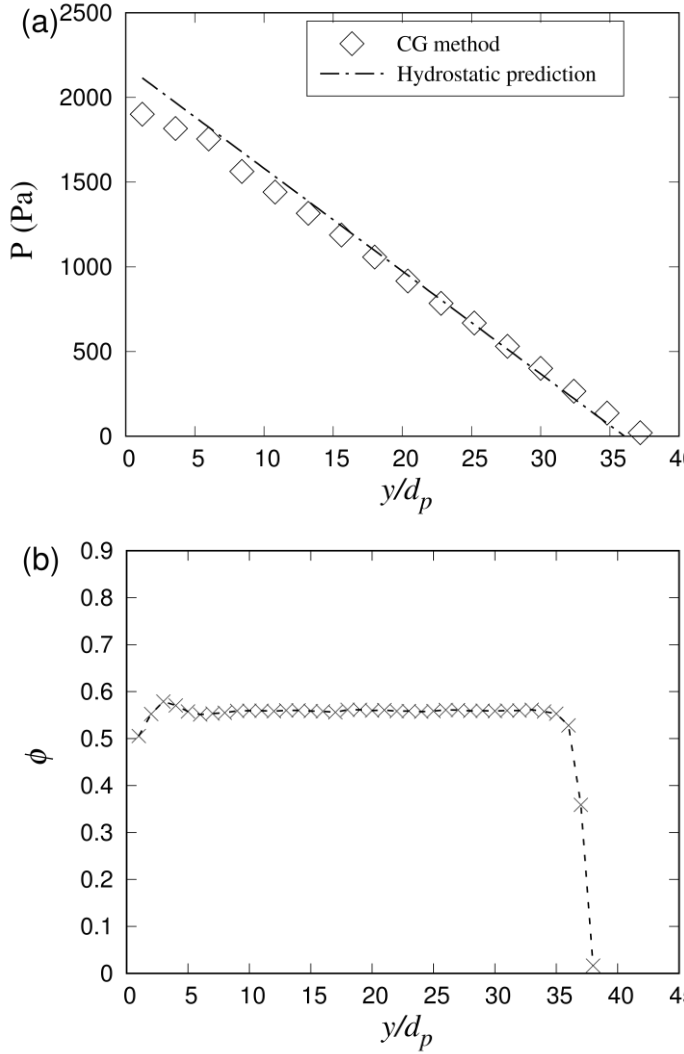

(Continue to the next page)

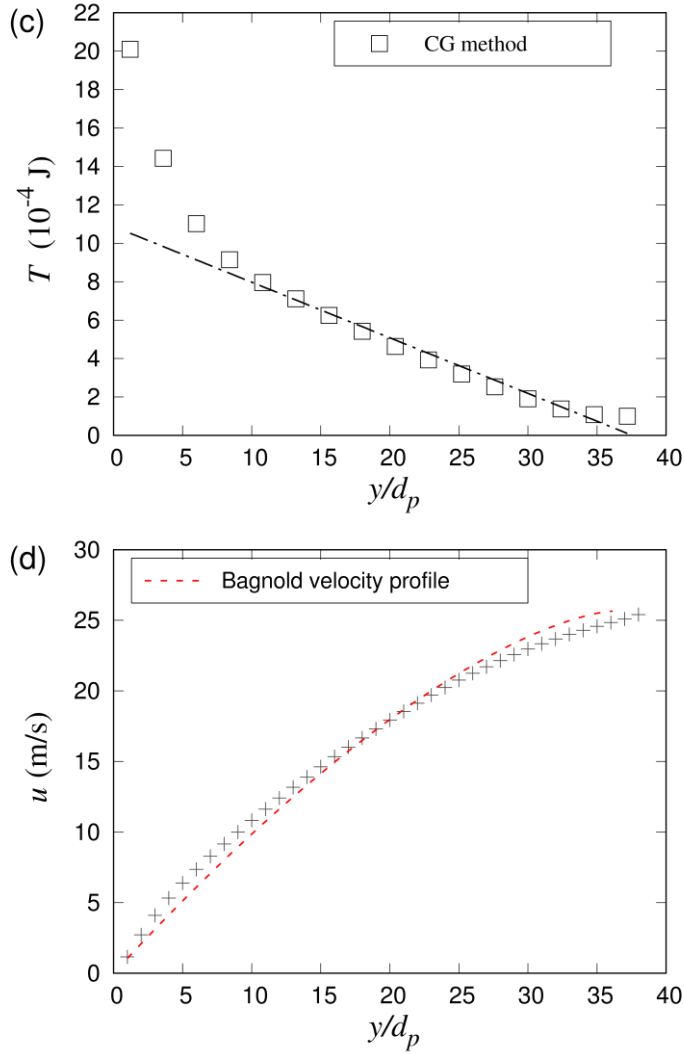

FIG 5.5 (a)Granular pressure along the y direction: (◇) granular pressure as determined by coarse graining (CG), (−·−) hydrostatic pressure i.e. $P_y = \rho_p \phi g_y (h_c - y)$ (Eq. (5. 21)) with $\phi = 0.55$; (b) Solid fraction along the y direction. The solid fraction is nearly constant across the bed ($\phi = 0.55$) except in the regions close to the surface and bottom (distances of approximately $5d_p$); (c) (□) granular temperature (Eq. (5. 11)) as determined by CG, (− · −) linear

fit of the CG data, suggesting a linearity between T and y (Eq. (5. 23)) in the core region of the dense granular shear flow. (d) Velocity in the x direction as a function of y/d_p. (+) DEM data and (---) Bagnold velocity profile (Bagnold 1954), i.e. $u(y) = 2/3\, I\theta \sqrt{P/(\varrho_p d_p)}\, h_c(1-(1-(y/h_c))^{1.5})$, where $I\theta = \dot{\gamma} d_p/(P/\varrho_p)^{0.5}$ (e.g. in this work $I\theta = 0.17$ for $\theta = 25^{\circ}$), P is the pressure at the bottom of the system and h_c is the height of the shear flow system. All data are extracted from a shear flow system with an inclination angle $\theta = 25^{\circ}$.

Further, in a steady-state, dense, granular shear flow, the granular pressure at a given height y is given by (Louge 2003; Jenkins and Yoon 2002)

$$P(y) = \frac{\partial P}{\partial y}(y - h_c) = \rho_p \phi g_y (h_c - y), \tag{5.21}$$

where h_c is the height of the flowing layer. The linear relationship between P and y is confirmed in (a). Substituting now $\phi = nV_p$ in Eq (5.21) and combining it with Eq. (5.16), we obtain the compressibility coefficient:

$$k_p = \frac{1}{n}\frac{1}{m_p g_y (h_c - y)} = \frac{1}{P}. \tag{5.22}$$

In a steady-state, dense, shear flow system, the solid fraction (and hence also the number density) is constant in the core region (Weinhart et al. 2016; Louge 2003; Jenkins 2006) as demonstrated in Figure 5.5(b). Following Eq. (5.12), i.e. $P = nTf(e,\phi)$, the granular temperature is also expected to vary linearly with y in regions where n and ϕ are constant. This behavior is confirmed in Figure 5.5(c). It is worth noting that both the granular pressure and temperature, Figures 5.5(a) and (c), as determined by coarse graining deviate from their linear dependencies with y close to the bottom wall (i.e., at $y < 5d_p$).

This wall-induced deviation is in agreement with previous reports, e.g. Weinhart et al. (2012). However, in our work the intruder is placed well away from the bottom plate and hence, the linear relationship of both the granular pressure and temperature with y is assumed to hold. Thus, combining Eq. (5.12) and (5.21) yields:

$$T = \frac{P}{nf(e,\phi)} = \frac{\rho_p \phi g_y (h_c - y)}{nf(e,\phi)}. \tag{5.23}$$

As n, e, ϕ are constant along y (and away from the boundaries) we obtain:

$$\frac{\partial T}{\partial y} = \frac{1}{nf(e,\phi)} \frac{\partial P}{\partial y} = -\frac{\rho_p \phi g_y}{nf(e,\phi)}. \tag{5.24}$$

Rearranging Eq. (5.24) and combining it with Eq. (5.23) yields:

$$\frac{\partial P}{\partial T} = \frac{\partial P}{\partial y} \Big/ \frac{\partial T}{\partial y} = nf(e,\phi). \tag{5.25}$$

In addition from Trujillo and Herrmann (2003) we have:

$$\frac{\alpha}{k_p} = \left(\partial P \big/ \partial T \right)_n. \tag{5.26}$$

Combining Eqs. (5.22), (5.23) and (5.26) gives:

$$\alpha = k_p \left(\partial P \big/ \partial T \right)_n = \frac{1}{P} nf(e,\phi) = \frac{1}{T}. \tag{5.27}$$

Here, following Trujillo and Herrmann (2003), we have assumed that k_p and α are constant when integrating Eq. (5.14). Hence, setting $k_p = 1/P_0$ and $\alpha = 1/T_0$, we obtain the following expression for the net buoyancy force acting on the control volume V_c in the reference case (Figure 5.4(a)):

$$F_{nb} = \left(1 - e^{-\frac{\Delta T}{T_0} + \frac{\Delta P}{P_0}} \right) \rho_P \phi g_y V_1. \tag{5.28}$$

A. The lift force model

In the following, we first establish the correlation between the net lift force $\mathbf{F}_{\text{net-lift}} = -\mathbf{F}_s$ acting on the intruder (i.e., F_s is the spring force that prevents the intruder in the DEM simulations from migrating to the top of the shear flow system) and the derived net buoyancy force acting on the imaginary control volume in Figure 5.4(a), i.e., Eq. (5.28). FIG plots the normalized net lift force on intruder, $F_{\text{net-lift}}/m_I g_y$, over the normalized net buoyancy force, $F_{\text{nb}}/m_I g_y$, for a series of DEM simulations in which the inclination angle and the size ratio d_I/d_p was varied. From Figure. 5.6 we obtain a linear correlation between $F_{\text{net-lift}}$ and F_{bn}, i.e.

$$F_{net-lift} = F_s = \frac{1}{a} F_{nb}, \tag{5.29}$$

with a = 0.55±0.035. The bulk solid fraction of our shear flow system is ϕ = 0.55, hence $\phi/a \cong 1$. Substituting Eq. (5.28) into Eq. (5.29):

$$F_{net-lift} = \left(1 - e^{-\frac{\Delta T}{T_0} + \frac{\Delta P}{P_0}} \right) \rho_P g_y V_I . \tag{5.30}$$

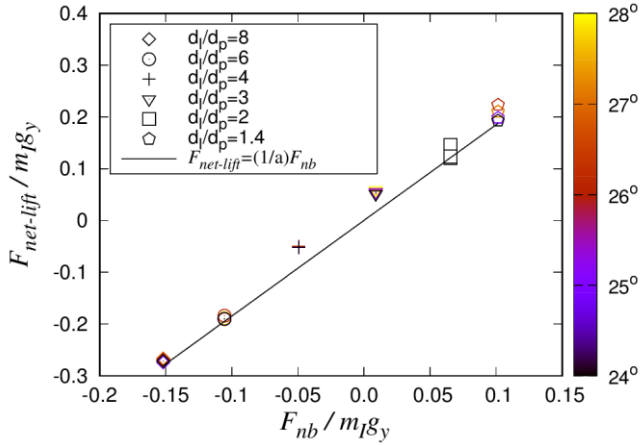

FIG 5.6. Linear relationship between the net buoyancy force, F_{nb}, as given by Eq. (5. 28) and the net lift force $F_{net\text{-}lift}$. Each data point represents a DEM simulation of a different d_I/d_p ratio (denoted by the marker symbol) and inclination angle ($\theta = 24°,25°,26°,27°,28°$ denoted by the colour scheme). The density ratio $\varrho_I/\varrho_p = 1$ was used in the simulations.

Figure 5.6 shows that the inclination angle has only a very minor influence on the magnitude of the spring force, in agreement with previous reports (Guillard, Forterre, and Pouliquen 2016; van der Vaart et al. 2018; Jing et al. 2020). On the other hand, the size ratio d_I/d_p affects the buoyancy force and hence also the spring force, appreciably, i.e. with increasing d_I/d_p the normalized buoyancy force (and the spring force) decrease. To compare our buoyancy model to previously proposed models, we calculate a lift force $\mathbf{F}_{\text{lift}} = -(\mathbf{F}_{net\text{-}lift}+\mathbf{F}_g) = -(\mathbf{F}_{bn}/a+\mathbf{F}_g)$, The lift force is the sum of all forces that act in the opposite direction of gravity on the intruder (e.g. Saffman and buoyancy forces). For our buoyancy model, the lift force in the specific shear system studied here, is given by:

$$
\begin{aligned}
F_{lift} &= \left| -(\mathbf{F}_{net-lift} + \mathbf{F}_g) \right| \\
&= \left(1 - e^{-\frac{\Delta T}{T_0} + \frac{\Delta P}{P_0}} \right) \rho_p g_y V_I + \rho_p g_y V_I \,. \\
&= \left(2 - e^{-\frac{\Delta T}{T_0} + \frac{\Delta P}{P_0}} \right) \rho_p g_y V_I
\end{aligned}
\tag{5.31}
$$

Normalizing the lift force by the gravitational force of the intruder ($\rho_p = \rho_I$) yields:

$$
\frac{F_{lift}}{\rho_I g_y V_I} = 2 - e^{-\frac{\Delta T}{T_0} + \frac{\Delta P}{P_0}} \,. \tag{5.32}
$$

In the following we performed a series of DEM simulations with varying ratios of d_I / d_p and determined the lift force acting on the intruder through $\mathbf{F}_{\text{lift}} = -(\mathbf{F}_s + \mathbf{F}_g)$. The differences in the granular pressure and temperature between the reference and the intruder cases, as required for our buoyancy model Eq. (5.32), were obtained from the Lagrangian DEM data through coarse graining.

Figure 5.7 plots the lift force determined by the virtual spring, the newly proposed buoyancy model (Eq. (5.32)), the Saffman-based lift force model (Eq. (5.5)) and the Archimedean-type buoyancy model given by Eq. (5.7). Concerning the general trend of the lift force, starting from $d_I/d_p = 1$ where $F_{\text{lift}}/(\rho_I V_I g_y) = 1$, the normalized lift force reaches a maximum at $d_I/d_p \sim 1.5$. The existence of a maximum in the (normalized) lift force with d_I / d_p has been observed previously. For example, Guillard, Forterre, and Pouliquen (2016) observed a maximum in the lift force at $d_I/d_p \sim 2$ in a 2D plane driven shear flow. Similarly van der Vaart et al. (2018) and Jing et al. (2020) observed a maximum in the lift force at $d_I / d_p = 1.5$ in a 3D shear chute flow. The reason for the maximum in the lift force is currently unclear, but further below we provide a tentative explanation. For intruder sizes $d_I / d_p > 4$, $F_{\text{lift}} / (\rho_I V_I g_y) < 1$, i.e. the intruder sinks. In several experimental works the sinking of large

intruders ($d_I/d_p > 5$ for $\varrho_I/\varrho_p = 1$) has been observed e.g. in rotating cylinders (Felix and Thomas 2004; Thomas 2000).

Our lift force model, Eq. (5.32), predicts the lift force determined by a virtual spring very accurately, while the Archimedean-type buoyancy model (Eq. (5.7) of Jing et al. (2020) captures the overall trend well but tends to over-predict the DEM data for $d_I/d_p < 6$. The difference between our modeling results and the buoyancy model of Jing *et al.* 2020 is likely because the empirical buoyancy model of Jing *et al.* 2020 is based on a perfect linear shear system (different to the Bagnold velocity profile obtained in this work). In addition, Fig. 5.7 includes the lift force data of inclined plane shear flow simulations (Hertzian contact model) (Jing et al. 2021) which show overall a good agreement with our simulation data. Also the van der Vaart et al. (van der Vaart et al. 2018) model, Eq. (5.5), captures very well the overall shape of the lift-force dependency on d_I/d_p, but also tends to over-predicts the DEM data. We speculate that the difference between the simulation results of van der Vaart et al. 2018 (Hertzian contact model) and our simulation data (linear spring model) are due to the different contact models applied. Indeed, differences in predicted velocity profiles, solid fraction, etc. due to differences in contact models haven been reported (Silbert et al. 2001). When adjusting the fitting parameters of the model of van der Vaart et al. (2018) to $a_0 = 0.24$ and $b_0 = 93$, a very good agreement with our DEM data is obtained, as illustrated by the dashed line in Figure. 5.7.

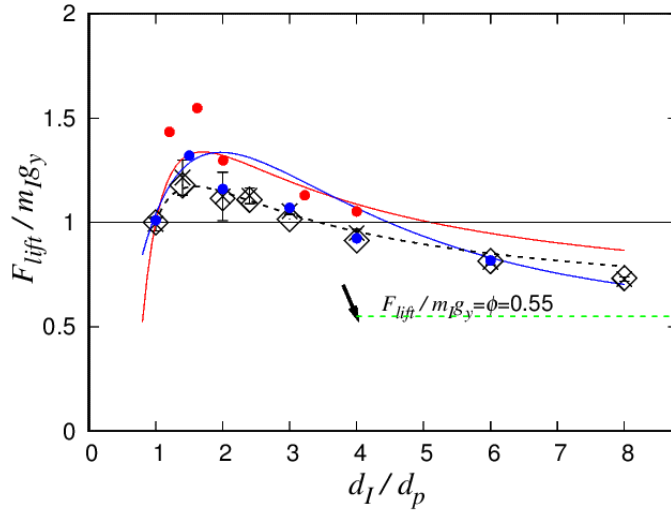

FIG 5.7. Normalized lift force as a function of the size ratio d_I/d_p with $\varrho_I/\varrho_p = 1$: (×) Lift force acting on the intruder as determined directly from the DEM simulations via a virtual spring. The error bars give the standard deviation obtained from five simulations (each 50 s simulation time in the steady state), (◇) lift force as determined by the proposed buoyancy model i.e. Eq. (5.32), (—) predictions of the buoyancy model of Jing et al. (2020), i.e. Eq. (5.7), (●) inclined shear flow simulation results (Hertzian contact model) of Jing et al. (2021), (—) Saffman force-based lift force model $F_{\text{lift}} = F_{\text{saft}}+F_b = -a_0 b_0 I_\theta \mu^{-0.5}(d_p/d_I-1)d_I^2 d_p^{-1} s(\dot{\gamma})+(\phi/\phi_I)\varrho_p g_y V_I$ using $a_0 = 0.24$ and $b_0 = 130.0$ as the fitting parameter as given by van der Vaart et al. (2018), (●) inclined plane flow simulation results (linear spring-dash contact model) of van der Vaart et al. (2018). The black dash line is a prediction of Eq. (5.5) that uses a_0=0.24 and b_0=93 as obtained from our simulation data. The solid, horizontal black line is a guiding reference for $F_{\text{lift}}/(\varrho_I V_I g_y) = 1$, i.e. below this reference line an intruder sinks, while values above the reference line indicate a rising intruder. (----) Normalized lift force in the continuum limit ($d_I/d_p >> 1$), i.e. $F_{\text{lift}}/(\varrho_I V_I g_y) \rightarrow \phi \sim 0.55$. In the DEM simulations the inclination angle was varied in the range $\theta = [24°, 28°]$, with $\rho_I/\rho_p = 1$.

To assess also the dependence of the lift force acting on the intruder on the vertical position of the intruder, the position of the intruder was varied from

$y_{min} = 7d_p$ to $y_{max} = 34d_p$. According to the velocity profile in the shear flow system under investigation, Figure 5.5(d), the shear rates vary between 186.0 s^{-1} (at $y = 7d_p$) and 55.5 s^{-1} (at $y = 34d_p$). Figure 5.8 shows that the lift force acting on the intruder is not sensitive to the vertical position at which the intruder is placed, suggesting that the lift force acting on the intruder is not sensitive to the shear rate, in agreement with previous observations (Jing et al. 2020; van der Vaart et al. 2018; Guillard, Forterre, and Pouliquen 2016).

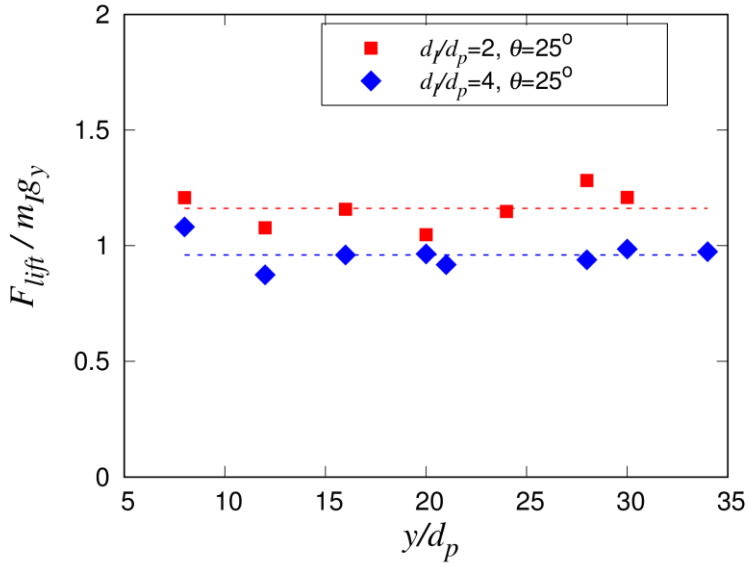

FIG 5.8. Lift force acting on the intruder determined directly from the virtual spring as a function of intruder position in the y direction (varied from $y_{min} = 7d_p$ to $y_{max} = 34d_p$). From the velocity profile given in (d) the shear rates vary from 186.0 s^{-1} (at $y = 7d_p$) to 55.5 s^{-1} (at $y = 34d_p$).

B. Cooling Effect of the Intruder

To elucidate the contributions of the variations of the pressure and temperature field upon addition of intruder on the lift force, Figure 5.9 plots $\Delta T/T_0$ and $\Delta P/P_0$ as a function of d_I/d_p. We observe that $\Delta T/T_0$ is negative, i.e. the introduction of an intruder leads to a local cooling of the granular temperature. As the ratio d_I/d_p increases the cooling effect becomes stronger. In the following we provide a tentative explanation for the cooling effect of the intruder in dense, shear flows. Concerning the granular system at hand, the major contribution to the granular temperature arises from velocity fluctuations along the shear direction x, i.e. $T_x \sim 10^{-5}$ J, $T_y, T_z \sim 10^{-6}$ J for $d_I/d_p = 8$. Hence in the following we focus on the velocity along the x direction. In the reference case, Figure 5.10(a), assuming a constant shear rate $\dot{\gamma}_0$ in a coarse graining (CG) volume, the granular temperature can be written as, $T_0 \approx \sum_{y=y_0-w}^{y_0+w} (1/(3N)) m_p[(\dot{\gamma}_0(y-y_0)+u_0)-u_0]^2$, where u_0 is the average particle velocity in the CG volume (dashed circle in Figure 5.10(a)), N is the number of particles in the coarse graining volume, m_p is the mass of the bed particles and y_0 is vertical position of the centre of the CG volume. As $\sum_{y=y_0-w}^{y_0+w} (1/N)\ [\dot{\gamma}_0^2(y-y_0)^2] = \dot{\gamma}_0^2\langle(y-y_0)^2\rangle$, T_0 can be re-written as, $T_0 \approx (1/3)\ \dot{\gamma}_0^2 m_p \langle(y-y_0)^2\rangle$, where $\langle\ \rangle$ denotes the average operation in the CG volume (located at y_0 with radius w). From Figure 5.3(b) we observe that the granular temperature indeed grows quadratically with w, i.e., $T_0 \sim \dot{\gamma}_0^2\, w^2$. Hence, two main factors affect the magnitude of granular temperature: (i) the size of the CG volume i.e., w (Figure 5.3(b)) and (ii) the magnitude of the shear rate.

Introducing an intruder into the shear system (Figure 5.10(b)) affects the average velocity in the coarse graining volume (new average velocity u_1). Similarly, to the reference case (assuming again a constant shear rate in the coarse graining volume) we can write the granular temperature in the intruder case as $T_1 = (1/3)\ \dot{\gamma}_1^2 m_p \langle(y-y_0)^2\rangle$. Figure 5.10 plots the velocity of particles (in the shear direction x) for the reference and the intruder case, including fits for the shear rate assuming a constant shear rate in the coarse graining volume. For the reference and the intruder case, shear rates of $\dot{\gamma}_0 = 59.5$ s^{-1} and $\dot{\gamma}_1 = 37.1$ s^{-1} (at $y = 100$ mm) are obtained, respectively. The shear rate in the intruder case is significantly lower than in the reference case, resulting in a lower granular temperature (cooling) in the intruder case. Overall, it appears that the presence of an intruder leads to a reduced particle velocity at its top

and a higher particle velocity at its bottom when compared to the reference case.

As a consequence, we observe that the intruder flattens the velocity profile in the CG volume which results in an overall cooling effect and hence a negative value of $\Delta T/T_0$ in particular for large intruders. The cooling effect of large intruders as observed in our dense, shear flow system is to some extend in contradiction to the work of Trujillo and Herrmann (2003) in which the intruder behaves like a heating source in a granular gas. Yet, the system studied in Trujillo and Herrmann (2003) is very different to our system, as it considers a dilute granular gas system under strong vibrations. In the system of Trujillo and Herrmann (2003) binary collision dominate (with a long free path length), whereas in our system multiple and enduring contacts prevail.

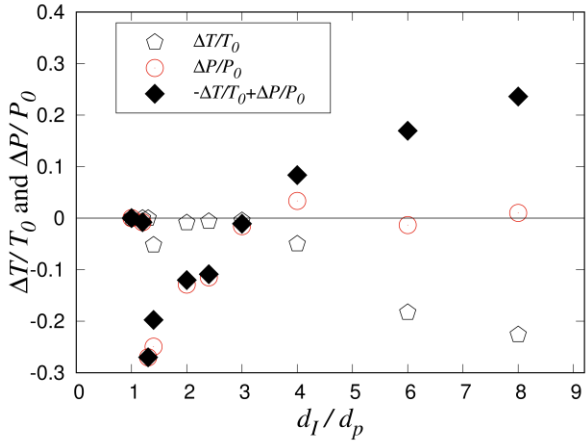

FIG 5.9. Variation of $\Delta P/P_0$ ($\Delta P = P_1 - P_0$) and $\Delta T/T_0$ ($\Delta T = T_1 - T_0$) as a function of d_I/d_p. Both the granular pressure and temperature are determined through coarse graining of the DEM data (simulation performed with an inclination angle $\theta = 25^\circ$ and $\varrho_I/\varrho_p = 1$). P_0 is the hydrostatic pressure, could be determined by coarse graining or analytically ($P_0 = \rho_p g_y (h_c - y_0)$ with $y_0 = 100$ mm).

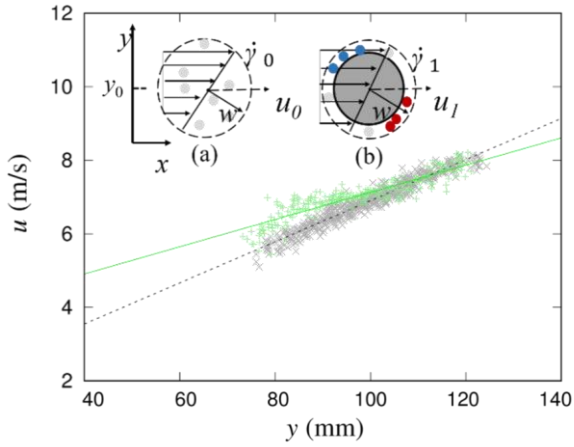

FIG 5.10. Velocity (in the shear direction x) of individual particles at $t = 399$ s that are located in the coarse graining volume centered at $y_0 = 100$ mm. The black dashed circle denotes the CG volume of radius $w = r_1 + d_p$ where $r_1 = 8d_p$. (×) Particle velocities in the reference case (insert Figure (a)) with (----) being the fitting assuming a constant shear rate in the CG volume, i.e. $\dot{\gamma}_0 = 59.5\ s^{-1}$ (+) Particle velocities in the intruder case (insert Figure (b)) with (—) being the constant shear rate fitting, i.e. $\dot{\gamma}_1 = 37.1\ s^{-1}$ in the CG volume. System parameters are $d_1/d_p = 8$, $\rho_1/\rho_p = 1$ and $\theta = 28^{\circ}$. Inset (a): Coarse graining (CG) volume of the reference case. The CG volume is a spherical space of radius w. Here, u_0 denotes the average velocity of the particles that are in the CG volume and $\dot{\gamma}_0$ is the shear rate in the CG volume. Inset (b): CG volume of the intruder case, the dark grey area denotes the intruder, $\dot{\gamma}_1$ is the shear rate in the CG volume and u_1 is the average velocity of the particles in the CG volume. The blue particles at the top of the intruder indicate a reduced velocity compared to the reference case while the red particles at the bottom of the intruder denote faster particles compared to the reference case.

C. The Continuum Limit

From Figure 5.9 we observe that for $d_1/d_p > 4$, $\Delta P/P_0 \to 0$. This asymptotic behaviour of $\Delta P/P_0$ is an indication that for $d_1/d_p \gg 1$ the system approaches

a continuum limit, i.e. the lift force acting on the intruder approaches the value given by an Archimedean type description of the buoyancy force, i.e. $F_b = \phi \varrho_p g_y V_I$, or $F_b / \varrho_p g_y V_I \rightarrow \phi$ (Figure 5.7). This trend has also been reported by Jing et al. (2020) and van der Vaart et al. (2018). In the continuum limit, i.e. $d_I/d_p \gg 1$ the intruder behaves as if being immersed in a fluid with density $\varrho_p \phi$. (Jing et al. 2020) argued that for $d_I/d_p \gg 1$ a large number of bed particles are surrounding (and hence in contact) with the intruder, leading to a high number of particle collisions and in turn a uniform stress transmission (similar to a continuum fluid). Therefore, for large values of d_I/d_p, $\Delta P = P_1 - P_0$ approaches zero (as confirmed in Figure 5.9).

To explore in more depth, the change in P when an intruder in the size range $1.5 < d_I/d_p < 4$ is introduced into the system, we calculated the pressure at the location of the intruder over 100 s and plot its distribution as a function of d_I/d_p in Figure 5.11. For $d_I/d_p = 1.5$, the modal value of the pressure is 800 Pa (mean value 987 Pa) is significantly smaller than the hydrostatic pressure of 1153 Pa. The difference between the mean value of the pressure distribution and the hydrostatic pressure is reflected in the positive pressure contribution to the upward-directed lift force acting on intruders with $d_I/d_p < 4$. In addition, the large deviation between the modal and hydrostatic pressure is likely the reason for the large fluctuations in the DEM-determined values of the lift force for smaller sizes ratios of d_I/d_p (Figure 5.7). Such fluctuations in DEM-determined lift forces have been reported previously (Jing et al. 2020; van der Vaart et al. 2018; Guillard, Forterre, and Pouliquen 2016). For $d_I/d_p = 4$, the pressure distribution becomes more symmetric with the modal ($P_{\text{modal}} = 1210$ Pa), mean ($P_{\text{mean}} = 1230$ Pa) and hydrostatic ($P_0 = 1153$ Pa) pressures being very close to each other (Figure 5.11(d), explaining both the small lift force and the small fluctuations in the DEM-determined lift force for $d_I/d_p \geq 4$ (Figures 5.7 and 5.9). The smaller fluctuations in the DEM-determined lift force for larger values of d_I/d_p are in agreement with previous works (Jing et al. 2020; van der Vaart et al. 2018; Guillard, Forterre, and Pouliquen 2016).

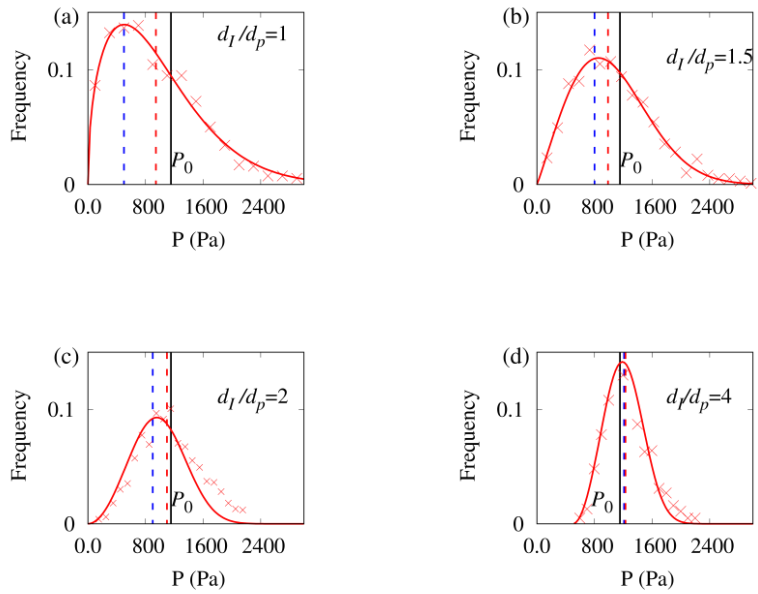

FIG 5.11. The distribution of the pressure at the location of the intruder, P(**r**(*t*), *t*), as a function of the size ratio: (a) $d_I/d_p = 1$, (b) $d_I/d_p = 1.5$, (c) $d_I/d_p = 2$, and (d) $d_I/d_p = 4$. The set-up used an inclination angle of $\theta = 24°$ with $\rho_I/\rho_p = 1$. Pressure data were sampled over 100 s in steps of 0.1 s. The hydrostatic pressure $P_0 = 1153$ Pa is denoted by the black, solid vertical line, given by $P_0 = \rho_p g_y(h_c - y_0)$ with $h_c = 0.192$ m and $y_0 = 0.1$ m. The mean pressure value is denoted by the red, dashed vertical line. The modal pressure value is denoted by the blue, dashed vertical line: (a) $P_{modal} = 500$ Pa, $P_{mean} = 944$ Pa (b) $P_{modal} = 800$ Pa, $P_{mean} = 987$ Pa (c) $P_{modal} = 900$ Pa, $P_{mean} = 1097$ Pa (d) $P_{modal} = 1210$ Pa, $P_{mean} = 1230$ Pa

D. The Effect of Density Differences on segregation

So far we have only considered cases in which the density of the intruder and the bed particles are equal. From Eq. (5.31), when scaling the lift force with the intruder weight ($\varrho_I g_y V_I$) the following relationship is obtained for $\varrho_p \neq \varrho_I$,

$$\frac{F_{lift}}{\rho_I g_y V_I} = \left(2 - e^{-\frac{\Delta T}{T_0} + \frac{\Delta P}{P_0}}\right) \frac{\rho_p}{\rho_I}, \tag{5.33}$$

When $F_{\text{lift}}/(\varrho_I V_I g_y) < 1$ the intruder sinks and for >1 the intruder rises. Similar to the model of Jing et al. (2020), also Eq. (5.33) shows a decoupling of the effects of the intruder size and density ratios. Figure 5.12 plots $F_{\text{lift}}/(m_I g_y)$ as a function of ϱ_p/ϱ_I for $d_I/d_p = 2$ and 4. Similar results to those in Fig. 5.12 also occur for $d_I/d_p = 1$, further confirming the model. The linear trend predicted by the lift force model, Eq. (5.33), agrees very well with the DEM data and with experimental observations that show that light intruders migrate upward while heavier intruders sink (Thomas 2000; Felix and Thomas 2004), which have been further presented in Figure 5.13.

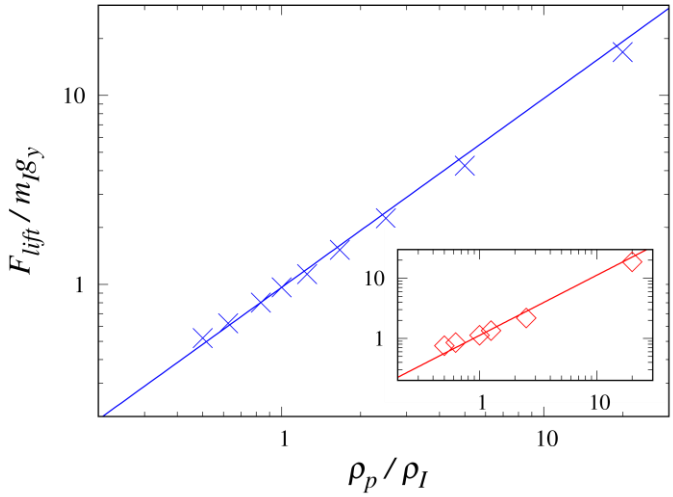

FIG 5.12. The normalized lift force as a function of the density ratio ϱ_p/ϱ_I for different intruder sizes (×) $d_I/d_p = 4$. (◇) $d_I/d_p = 2$. The blue and red straight lines are Eq. (5.33).

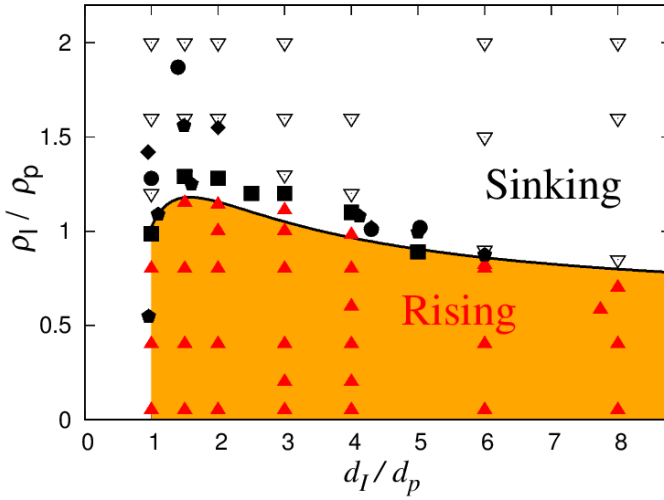

FIG 5.13. Neutral buoyancy limit of a single intruder in a dense, granular shear flow as function of d_I/d_p and ϱ_I/ϱ_p. The black solid curve denotes the neutral buoyancy limit given by $\left(2 - e^{-\frac{\Delta T}{T_0}+\frac{\Delta P}{P_0}}\right) \frac{\rho_p}{\rho_I} = 1$. DEM data using an inclination angle of $\theta = 25^\circ$. ▽ intruder sinks, ▲ intruder rises. The solid black symbol are neutral buoyancy limits obtained in (■) plane shear driven flow (Jing et al. 2020), (●) heap flow, (◆) chute flow and (⬟) rotating drums (Felix and Thomas 2004).

From Eq. (5.33) it is also possible to extract the neutral buoyancy limit, which is given by $\left(2 - e^{-\frac{\Delta T}{T_0}+\frac{\Delta P}{P_0}}\right)\frac{\rho_p}{\rho_I} = 1$ and plotted in Figure 5.13. It is worth noting that the experimental data (solid black symbol) are extracted from multiple intruder systems. For some systems, the neutral buoyancy limit deviates from that of the single intruder simulation results, particularly for size ratios between 1 to 3. It is not surprising, however, that the intruder concentration effects the segregation process, e.g. (Duan et al. 2021).

In this work, we propose a new lift force model for intruders in dense, granular shear flows by extending the work of Trujillo and Herrmann (2003). The lift force is interpreted as a buoyancy force whereby the density difference arises both from granular temperature and granular pressure contributions. We observe that the presence of an intruder leads to a cooling effect and a local flattening of the shear velocity profile (lower shear rate). For large intruders, i.e., $d_I/d_p > 4$, the local pressure disturbance (and hence contribution to the lift force) is very small as the system approaches a continuum limit, in which the pressure acting on the intruder equals to the hydrostatic pressure of the system. On the other hand, for $1< d_I/d_p < 4$ the local granular pressure at the location of the intruder is lower than the hydrostatic pressure leading in turn to a positive lift force. The cooling effect due to the presence of an intruder increases with intruder size, leading ultimately to the sinking of large intruders. The modified model predicts DEM-determined lift forces very well and allows the description of a neutral buoyancy limit.

FINGERING INSTABILITIES IN BINARY GRANULAR SYSTEMS

6

Adapted from Liu. M., Conzelmann. N, Girardin. L, Dickhardt. F, McLaren. C, Metzger. J., Müller. C.(2022). Fingering instabilities in binary granular systems. (submitted)

6.1 Abstract

Fingering instabilities akin to the Rayleigh-Taylor (RT) instability in fluids have been observed in a binary granular system consisting of dense and small particles layered on top of lighter and larger particles, when the system is subjected to vertical vibration and fluidizing gas flow. Using observations from experiments and numerical modelling we explore whether the theory developed to describe the Rayleigh-Taylor (RT) instability in fluids is also applicable to binary granular systems. Our results confirm the applicability of the classic RT instability theory for binary granular systems demonstrating that several key features are observed in both types of systems, viz: (i) The characteristic wavenumber of the instability is constant with time, (ii) the amplitude of the characteristic wavenumber initially grows exponentially and (iii) the dispersion relation between the wavenumbers k of the interface instability and the growth rates $n(k)$ of their amplitudes holds in both fluid-fluid and binary granular systems. Our results also demonstrate that inter-particle friction is essential for the RT instability to occur in granular media. For zero particle friction the interface instability bears a greater resembles to the Richtmyer-Meshkov instability. We further define a yield criterion Y for the interface by treating the granular medium as a viscoplastic material; only for $Y > 15$ fingering occurs. Interestingly, previous work has shown that instabilities in the Earth's lower mantle, another viscoplastic material, also occur for similar values of Y.

Rayleigh-Taylor (RT) instabilities arise at the interface between two fluids of different densities; for example, when a fluid with a higher density is layered on top of a fluid of a lower density in a gravitational field. Any perturbation of the (flat) interface induces a local pressure gradient (acting in the normal direction to the interface) leading to a growth of the perturbation, which manifests itself as fingers intruding upwards and downwards into the fluid layers (Taylor 1950). While the RT instability is a classical phenomenon in fluid mechanics, more recently it has been reported also in granular systems such as granular suspensions (Chevalier et al. 2006; Voltz, Pesch, and Rehberg 2002), gas-particle mixtures (Johnsen et al. 2006; Vinningland et al. 2007), or particle-particle mixtures (McLaren et al. 2019). Beyond these laboratory systems, RT instabilities are also observed in geological settings, such as plumes rising upwards in the Earth's mantle (Davaille, Carrez, and Cordier 2018), river bed erosion (Julien 2018) or the formation of salt domes (Nettleton 1934)

For fluid-particle systems in which the forces acting on the particles are dominated by fluid-particle interactions (e.g. drag) while particle inertia is negligible, a hydrodynamic description of the formation of RT-like instabilities has been proposed (Noetinger 1989; Lange et al. 1998) and experimentally verified (Voltz, Pesch, and Rehberg 2002; Wysocki et al. 2009). Typically, in these models the particle-fluid mixture is treated as an immiscible fluid phase with a uniform solid fraction (placed on top of a layer of a pure fluid). Linear stability analysis has shown that the initial growth of the interface in fluid-particle systems can indeed be described by the dispersion relation which was developed originally for the RT instability in fluid-fluid systems (Chandrasekhar 2013). The dispersion relation provides a relationship between the interface perturbations, characterized by a series of wavenumbers k, and their respective growth rates $n(k)$. According to Taylor's instability theory, perturbations of the interface grow exponentially with time (Taylor 1950). A good quantitative agreement between such a linear stability analysis and experimental measurements has been observed for a glycerin-particle system in a Hele-Shaw-like cell where a glycerin-particle suspension was at the bottom while a glycerin layer was placed on top (Voltz, Pesch, and Rehberg

2002). By inverting the Hele-Shaw cell, the suspension sinks under gravity while glycerin rises up, exhibiting classic fingering structures.

Finger-instabilities have also been observed in a radial Hele-Shaw-like cell in which a fluid penetrates into a single-phase granular medium (Sandnes et al. 2007; Cheng et al. 2008; Huang et al. 2012). However, in such a configuration the fluid fingers side-branch rather than split at the tip as it is commonly observed for fingering in Newtonian fluids (Bensimon et al. 1986). This side-branching of the viscous fingers is considered as a granular equivalent of the classic Saffman-Taylor instability in the zero-surface-tension limit. The Saffman-Taylor instability occurs when injecting a viscous fluid into a more viscous one. A quantitative analysis of experiments has shown however that the scaling of the growth of fingers in a granular medium is distinct from the scaling in fluid-fluid systems; in granular systems the finger width W_{finger} follows the scaling $W_{finger} \sim U_i^{1/2}$ (Cheng et al. 2008), while in conventional Newtonian fluids $W_{finger} \sim U_i^{-1/2}$ is observed, where U_i is the local interfacial growth velocity, i.e. the velocity with which fingers grow radially (identified by tracing the outermost boundary of the fingers). This very distinct scaling behaviour is believed to be a consequence of the different dissipation mechanism in granular materials, viz. friction-induced dissipation, as opposed to viscous damping in fluids. (Aranson and Tsimring 2006; Conway, Shinbrot, and Glasser 2004; Jaeger, Nagel, and Behringer 1996)

In granular media interface instabilities have also been observed when a layer of a dense granular material (instead of a liquid) is placed above a layer of air (Vinningland et al. 2007). Here, fingering patterns emerge as the granular material falls under gravity. This has been reported, e.g. by Vinningland et al. (2007) who tracked polystyrene particles falling in a Hele-Shaw cell. Vinningland et al. (2007) determined the interface wavenumbers k and the corresponding growth rates. Their findings show that the amplitude of the dominant wavenumber does not grow exponentially over time, suggesting the instability is not in the linear regime predicted by the classical Taylor theory (Taylor 1950). This difference in growth rate might be explained by the large density difference between the particles and air ($\rho_{\text{particle}} \cong 1000\rho_{\text{air}}$) making particle inertia the dominating effect. Hence, it is conceivable that the RT instability theories developed for fluid-fluid systems maybe have limitations in

describing RT-like instabilities in granular systems in which particle inertia dominates over the forces due to fluid-particle interactions.

Very recently, an additional RT-like instability was reported in particle-particle systems that are agitated by both vibration and a fluidizing gas (McLaren et al. 2019). Using two sets of particles with matching minimum fluidizing velocity U_{mf} (but different diameters and densities) McLaren et al. (2019) could ensure that both particle sets experience equal fluid-particle interaction forces. As U_{mf} scales with $U_{mf} \propto d_i^{1/2}\rho_i$, where d_i is the diameter of the particle and ρ_i is the particle density, the lighter particles (subscript $i = L$) had a diameter of d_L = 1.70 mm and a density of ρ_L = 2500 kg/m^3, while the heavier particles (subscript $i = H$) had a diameter of d_H = 1.105 mm and a density of ρ_H = 6000 kg/m^3. The system was initialized by placing the heavy particles on top of a layer of light particles. Upon agitation by combined vibration and gas fluidization, the light particles penetrated upwards through the layer of denser particles exhibiting finger-like structures. Although the fingering-structures in the granular material mimic the structures that are commonly observed in conventional fluids, it was argued that the physics controlling the granular RT-like instability must be different involving a locally preferred gas channelling through the fingers of light particles and particle-particle contact forces pushing downwards the heavier particles. However, as McLaren et al. (2019) have finely tuned the fluidization properties of the particle sets such that the fluid drag forces balance the weight of the particles and hence particle inertia is very likely to play a minor role, classic hydrodynamic RT instability theory might be applicable to such binary granular systems.

Therefore, the objective of this work is to conduct a quantitative analysis of the growth of fingers in a binary granular system allowing us to investigate its scaling behaviour and to assess whether it can be described by the classical RT theory developed for fluids. By complementing experiments with computational fluid dynamics coupled with the discrete element modelling (CFD-DEM) simulations we are able to probe the parameters that control the formation and growth of fingers in granular media and provide further insight into the underlying mechanism controlling this particular RT-like instability.

A. Numerical Methodology

In the present work, CFD-DEM simulations were performed using the CFDEM®*Coupling* framework (Goniva et al. 2012). In the DEM part, particles are modelled as individual, freely moving entities with each particle i having a certain mass m_i, velocity $\mathbf{u}_{pi}$ and angular velocity $\boldsymbol{\omega}_i$. Forces acting on the particles lead to changes in their trajectories as described by Newton's second law of motion:

$$m_i \frac{d\mathbf{u}_{pi}}{dt} = \mathbf{f}_{ti} + \mathbf{f}_{fpi} + m_i \mathbf{g}\,, \tag{6.1}$$

and

$$I_i \frac{d\boldsymbol{\omega}_i}{dt} = \mathbf{T}_i\,, \tag{6.2}$$

where $\mathbf{f}_{ti}$ and $\mathbf{f}_{fpi}$ are the particle-particle contact force and the fluid-particle force, respectively, $\mathbf{g}$ is the gravitational acceleration, I_i is the moment of inertia of particle i and $\boldsymbol{T}_i$ is the torque acting on particle i. The contact force between two contacting particles, $\mathbf{f}_{ti}$, is modelled via a Hertzian contact model using the following material properties: Youngs's modulus E = 5 MPa, Poisson ratio ν = 0.2, coefficient of restitution e = 0.30, and inter-particle friction coefficient μ_p = 0.3.

For the CFD part, the fluid phase is modelled by the locally averaged Navier-Stokes equations using a finite volume scheme:

$$\frac{\partial}{\partial t}(\varepsilon_f \rho_f) + \nabla \cdot (\varepsilon_f \rho_f \mathbf{u}_f) = 0\,, \tag{6.3}$$

and

$$\frac{\partial}{\partial t}(\varepsilon_f \rho_f \mathbf{u}_f) + \nabla \cdot (\varepsilon_f \rho_f \mathbf{u}_f \mathbf{u}_f) = -\nabla p + \nabla \cdot (\varepsilon_f \boldsymbol{\tau}_f) + \varepsilon_f \rho_f \mathbf{g} - \mathbf{F}_{fp}, \qquad (6.4)$$

where ε_f, ρ_f, $\mathbf{u}_f$, and $\boldsymbol{\tau}_f$ are the void fraction, the fluid density, the fluid velocity and the viscous stress of the fluid, respectively. The term $\boldsymbol{F}_{fp}$ describes the momentum exchange between the particle and fluid phases and is given by:

$$\mathbf{F}_{fp} = \sum_{i=1}^{mc_i} \frac{1}{V_{mc}} \mathbf{f}_{fpi}, \qquad (6.5)$$

where mc is the index of a given fluid cell, mc_i is the index of each particle in a given fluid cell mc and V_{mc} is the volume of the cell. The fluid force acting on each particle in the fluid cell is given as,

$$\mathbf{F}_{fp} = -V_{pi} \nabla p + V_{pi} \nabla \cdot \boldsymbol{\tau}_f + \varepsilon_f \mathbf{f}_{di}, \qquad (6.6)$$

where $\varepsilon_f \mathbf{f}_{di}$ is the fluid drag acting on particle i. To model $\mathbf{f}_{di}$, the Koch-Hill correlation is used (Hill, Koch, and Ladd 2001).

B. Simulation setup

The simulation setup illustrated in Figure 6.1 mirrors the experimental setup reported by McLaren et al. (2019), i.e., using the same particle densities and sizes. The numerical simulations are initialized by placing a layer of heavier (ρ_H = 6000 kg/m^3) particles of smaller diameter (d_H = 1.16 mm) on top of lighter (ρ_L = 2500 kg/m^3), but larger (d_L = 1.70 mm) particles. For both types of particles some degree of polydispersity ($\pm 0.1 d_{H/L}$) is introduced to avoid crystallization. The width of the system l_x = 200 mm is identical to the experimental setup of McLaren et al. (2019), while the filling height is reduced to l_z = 200 mm for computational efficiency. The transverse thickness of the bed (y direction) is 10 mm. The particle bed is agitated by a combination of an upward-directed gas flow (air) with an uniform inlet velocity U = 1.13 m/s (density ρ_{air} = 1.2 kg/m^3 and viscosity η_{air} = 1.8·10^{-5} Pa·s) and a vertical vibration with $z(t) = A\sin(2\pi f t)$, where A = 1 mm and f = 10 Hz.

The particle-wall interaction is modelled similarly to the particle-particle contacts (Hertzian contact model) whereby the wall is treated as a particle with an infinite radius. The pressure at the outlet (top) is fixed to $1.2 \cdot 10^5$ Pa and the size of a fluid cells is $5 \times 5 \times 5$ mm^3). The DEM time step size is 10^{-5} s, the CFD time step size is $5 \cdot 10^{-4}$ s and the CFD-DEM coupling interval is $5 \cdot 10^{-4}$ s.

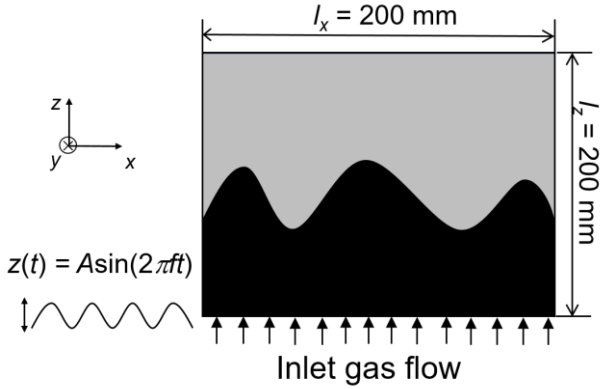

FIG 6.1. Illustration of the the simulated system. The gray colour represents the heavy particles (diameter d_H = 1.16 mm and density ρ_H = 6000 kg/m^3) while the black colour denotes the light particles with d_L = 1.70 mm and ρ_L = 2500 kg/m^3. The container is vibrated vertically with $z(t) = A\sin(2\pi f t)$, where A = 1 mm and f = 10 Hz. A uniform upwards-directed gas flow (air) is injected at the bottom of the container with a velocity U = 1.13 m/s (density ρ_{air} = 1.2 kg/m^3 and viscosity $\eta_{air} = 1.8 \cdot 10^{-5}$ Pa·s).

C. Experimental setup

The numerical simulations are complemented by experiments that are acquired in a setup identical to the one reported by McLaren et al. (2019). The particle bed is contained in a container made of acrylic glass with a width of 200 mm, height 500 mm and transverse thickness 10 mm (pseudo-2D bed). The experiment is initialized by filling the container first with a layer of light (ρ_L = 2500 kg/m^3), large diameter particles (d_L = 1.73±0.06 mm) followed by a layer of heavy (ρ_H = 6000 kg/m^3), but smaller particles (d_H =

1.17±0.06 mm). The thickness of each layer is 200 mm. The two types of particles are purchased from Sigmund Lindner GmbH and have the same properties as the particles used in the numerical simulations, i.e., a coefficient of restitution of 0.66 and a coefficient of friction of 0.4. During an experiment, humidified air is injected through a distributor placed at the bottom of the container (20 holes of diameter 1.1 mm) to fluidize the particles. The superficial air velocity was U = 1.55 m/s (controlled via a Bronkhorst mass flow controller F-203AV). In addition, a vertical vibration is introduced via an electrodynamic shaker (Labworks Inc., ET-139) using a vibration strength of $\Gamma = A\omega^2/g = 0.45$ with ω = 188 rad/s.

D. Data analysis

In the experiments the interface between the two types of particles is recorded by high-speed camera imaging. Similarly, the predictions of the numerical simulations are visualized using the software ParaView to produce grey-scale images of the interface between the two types of particles. From these images the interface (red line in Figure 6.2) is identified by converting first the grey-scale image into a binary image by thresholding. The interface identification is insensitive to varying the thresholding value as doing so would only change individual pixels which in turn only affects high wavenumbers that are outside of the relevant range for granular fingering. At a given location in x, the interface position $z(x)$ is determined as the position in the z-direction at which the pixel value change from 1 (white) to 0 (black) (Voltz, Pesch, and Rehberg 2002).

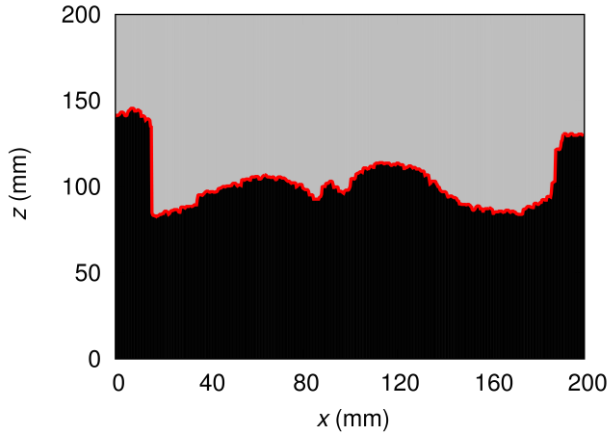

FIG 6.2: Snapshot of a numerical simulation at $\Delta t = 6.4$ s. For this simulation a layer of heavy ($\rho H = 6000$ kg/m3) particles with a small diameter ($dH = 1.16$ mm) is placed on top of lighter ($\rho L = 2500$ kg/m3) but larger ($dL = 1.70$ mm) particles. The initial filling height for both layers is 100 mm. The system width is 200 mm and the transverse depth is 10 mm. The red curve denotes the interface between the heavy (gray) and light (black) particles identified through the algorithm proposed by Voltz, Pesch, and Rehberg (2002)

The function $z(x)$ is subsequently Fourier transformed

$$Z(k) = \sum_{n=0}^{N-1} z(x_n) e^{-i2\pi nk/N}, \tag{6.7}$$

where $z(x_n)$ is the vertical position of the interface at the horizontal position x_n. The magnitude of the Fourier coefficient $Z(k)$ gives the amplitude of the k-th mode (wavenumber k). Typically, the 10 pixels next to the side walls are disregarded for the analysis.

FIG 6.3 (Continue to the next page)

FIG 6.3. Snapshots of the formation of granular fingers as observed in numerical simulations (a) and experiments (b) at various time steps Δt. In the numerical simulations the container is of width l_x = 200 mm with an initial filling height of l_z = 200 mm. The dimensions of the experimental setup are l_x = 200 mm and l_z = 400 mm. The transverse thickness in both the experiment and simulation is l_y = 10 mm. The heavier and smaller particles (d_H = 1.16 mm, ρ_H = 6000 kg/m^3) appear as grey (simulations) or white (experiments), while the lighter and larger particles (d_L = 1.7 mm, ρ_L = 2500 kg/m^3) are black.

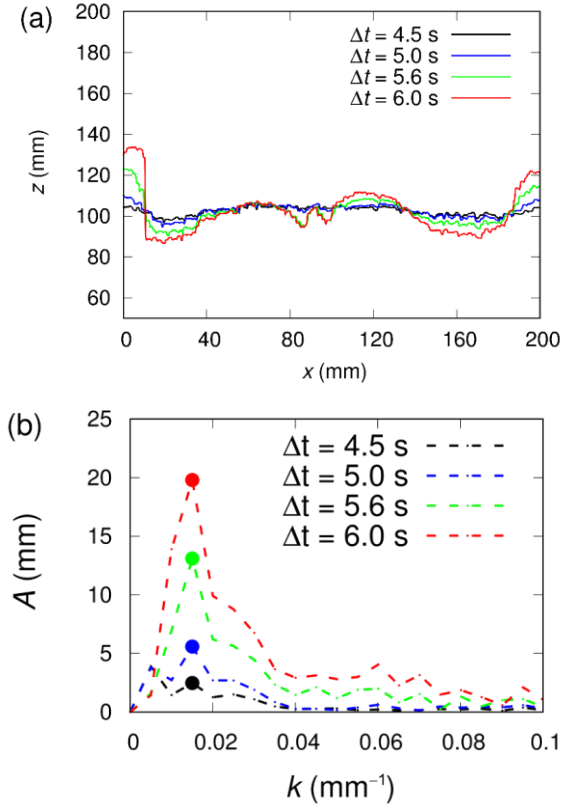

FIG 6.4. (a) The geometry of the interface between the light and heavy particles as a function of time as obtained from numerical simulations. (b)

Fourier transform of the interface plotted in (a), where k is the wavenumber, and A is the corresponding amplitude. The wavenumber with the fastest growing amplitude, i.e., the dominant wavenumber is marked by solid circles. The dominant wavenumber (k_c = 0.015 mm^{-1}) is the characteristic wavenumber of the fingering instability.

6.4 Results and discussion

Figure 6.3 plots snapshots of the shape of the interface between the light and heavy particles in both the experiments and numerical simulations for certain times. Qualitatively the experimental observations and the numerical results agree well, however, a quantitative comparison between the experimental and numerical results from simple image analysis is not possible. Hence, for a quantitative comparison, we extract the function of the interface $z(x)$ (Figure 6.4(a)) and perform a Fourier transform. Figure 6.4(b) shows the amplitudes of the wavenumbers k = 0.01–0.1 mm^{-1} at selected time steps. By tracking the amplitude over time, we obtain a growth rate $n(k)$ that can be approximated by an exponential expression (vide infra). The characteristic (i.e. dominant) wavenumber k_c of the fingering instability is the wavenumber with the fastest growing amplitude A. For the setup shown in Figure 6.4 with k_c = 0.015 mm^{-1} (characteristic wavelength $\lambda_c = 1/k_c$ = 66.7 mm), the characteristic wavenumber is coincidentally also the wavenumber with the highest amplitude A. In the binary granular system studied here, one wavenumber remains characteristic with time. Such a behaviour has been reported also for the classical fluid-fluid and liquid-particle systems (Voltz, Pesch, and Rehberg 2002), while for gas-particle systems the characteristic wavenumber is not necessarily constant with time, but instead was observed to generally increase with time (attributed to the branching of the fingers) (Vinningland et al. 2007).

Next, we study the growth rate of the fingering instability by plotting the amplitude of the characteristic wavenumber (k_c = 0.015 mm^{-1}) as a function of time. Figure 6.5 plots both the results of the numerical simulations and the experiments (inset). Figure 6.5 shows that a sufficiently long time (~3 s) is required until an appreciable growth in amplitude occurs. Once sufficiently

large perturbations have been formed, fingers emerge and grow with an exponential growth rate. Fitting an exponential function to this initial growth period, i.e. $A(k) = A_0 e^{(n(k)t)}$, yields growth rates of $n_E(k_c) = 1.75 \pm 0.04$ s^{-1} from the experimental data and $n_S(k_c) = 1.67 \pm 0.05$ s^{-1} from the numerical simulations, showing very good agreement between experiments and simulations. According to Taylor's theory (Taylor 1950), exponential growth only occurs for very small perturbations ($A < 0.4\lambda$). Therefore, only the growth period in which $A < 0.4\lambda_c$ was considered for the fitting, i.e., $\Delta t = 3$–6 s.

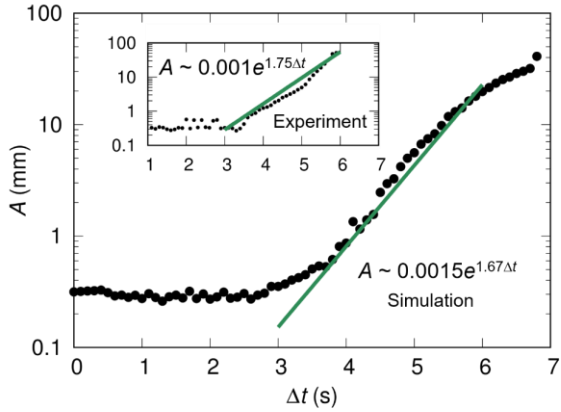

FIG 6.5. Growth of the amplitude A of the characteristic wavenumber k_c = 0.015 mm^{-1} as a function of time as obtained from numerical modelling and experiments (inset). The green lines are exponential fits during the initial growth period.

A. Rayleigh-Taylor instability theory

Our experimental and numerical modelling data have shown that there are some striking similarities with regards to the finger morphology and growth rate between the fingering instability in binary granular systems and their classic fluid counterpart. In the following we investigate if the dispersion relation between the wavenumber k and its respective growth rate $n(k)$ as derived for conventional fluid-fluid systems is equally applicable to binary granular systems. The dispersion relation is a result of the linear RT instability

theory which was first reported by Harrison (1908) and subsequently developed further by Chandrasekhar (2013), and Bellman and Pennington (1954). The linear RT instability theory models the growing perturbations of an initially cosine shaped, unstable interface between a denser fluid on top of a less dense fluid using hydrodynamic arguments. To derive the dispersion relation for a binary granular system, it is assumed that both granular media are viscous and incompressible and surface tension is neglected. The full derivation of the implicit dispersion relation for a binary granular system, which is based on the work by Bellman and Pennington (1954), is given in Appendix 6A. Here only the final form of the dispersion relation is given as:

$$\left[-gf(\varrho_H-\varrho_L)K+\phi(\varrho_L+\varrho_H)n(K)^2\right]M+4n(K)K=0\,, \tag{6.8}$$

where M is given by

$$M=\frac{1}{\eta_H K+(\eta_L^2K^2+\phi\varrho_L n(K)\eta_L)^{1/2}}+\frac{1}{\eta_L K+(\eta_H^2K^2+\phi\varrho_H n(K)\eta_H)^{1/2}}\,. \tag{6.9}$$

Here K is the angular wavenumber, $K=2\pi k$, and ϕ is the bulk solid fraction. η_L and η_H are the viscosity of the light and heavy granular medium, respectively. However, the viscosity of granular materials is not a constant, but dependents on the local state of the system (i.e., it is controlled by the local pressure, solid fraction and shear rate (Chen et al. 2021; Colafigli et al. 2009)). Since the characteristic wavelength of the granular system at hand is known, i.e., λ_c = 66.7 mm, we can derive an explicit equation for the granular viscosity from the dispersion relation when assuming that both granular media have the same viscosity, i.e., $\eta_L = \eta_H$. To derive an equation for the viscosity, Bellman and Pennington (1954) propose to simplify Eq. (6.8) by assuming that the growth rates of high wavenumbers are limited by viscosity and the growth rate decreases with increasing wavenumber, i.e. $\rho n(k) \ll \eta k^2$. This simplification yields:

$$n^2(K)+2\frac{\eta_H+\eta_L}{\phi\varrho_H+\phi\varrho_L}K^2n(K)-gK\frac{\phi\varrho_H-\phi\varrho_L}{\phi\varrho_H+\phi\varrho_L}=0\,. \tag{6.10}$$

Since the amplitude of the characteristic wavenumber has the highest growth rate, the characteristic wavenumber can be found by differentiating Eq. (10) with respect to K and setting $dn(K)/dK = 0$:

$$K_c = \frac{(\phi\varrho_H + \phi\varrho_L)\,g}{4n(K_c)(\eta_H + \eta_L)}. \tag{6.11}$$

Substituting Eq. (6.11) into Eq. (6.10), the characteristic wavelength $\lambda_c = 2\pi/K_c$ is given as (Pan, Joseph, and Glowinski 2001):

$$\lambda_c = 2\pi\left(\frac{8(\eta_H + \eta_L)^2}{\phi^2(\varrho_H^2 - \varrho_L^2)g}\right)^{1/3} \tag{6.12}$$

To calculate the granular viscosity from Eq. (6.12), the bulk solid fraction ϕ is required. The bulk solid fraction can be obtained from the numerical simulations via coarse graining (described in detail in Appendix 6B). Coarse-graining yields $\phi = 0.6 \pm 0.03$. Using $\phi = 0.6$ in Eq. (6.12), we obtain a granular viscosity of $\eta = 1.95$ Pa·s. This value is close to the value of 1.25 Pa·s, that is predicted by a viscosity model for sheared and fluidized granular systems (Colafigli et al. 2009), i.e. using the correlation $\eta_{eff} = \eta_{air}\exp(k_0 + k_1\dot{\gamma} + k_2\phi)$, where $k_0 = 2$, $k_1 = -1.78$, $k_2 = 20.20$, $\eta_{air} = 1.8\cdot10^{-5}$ Pa·s and approximating the shear rate by the growth rate of the characteristic wavenumber, i.e. $n(k) = 1.67\ s^{-1}$. Having estimated now the granular viscosity we can plot the dispersion relationship between $n(k)$ and k for the binary granular system studied here by numerically solving Eq. (6.8). The results are given in Figure 6.6, and we observe that classical RT theory predicts generally very well the growth rate of the interface amplitude $A(k)$ as a function of the wavenumber k (using both experimental and numerical data), although there is some over prediction of the numerical and experimental data, for higher wavenumbers (possibly due to the fact that the shear rate was approximated by the growth rate of the characteristic wavenumber).

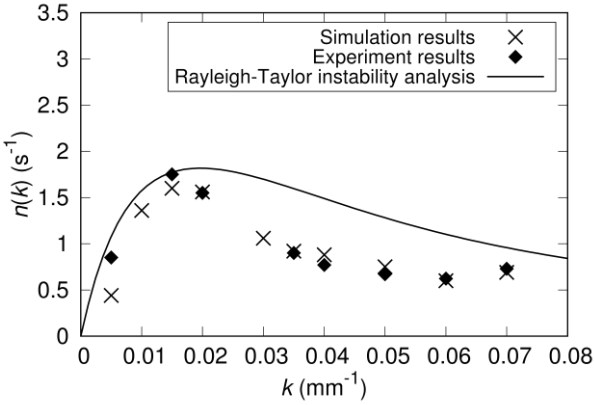

FIG 6.6. The dispersion relation, i.e., the growth rate $n(k)$ as a function of the wavenumber k as predicted by RT theory [Eq. (6.8)] (solid line) and the respective data obtained from numerical simulations (×) and experiments (◇).

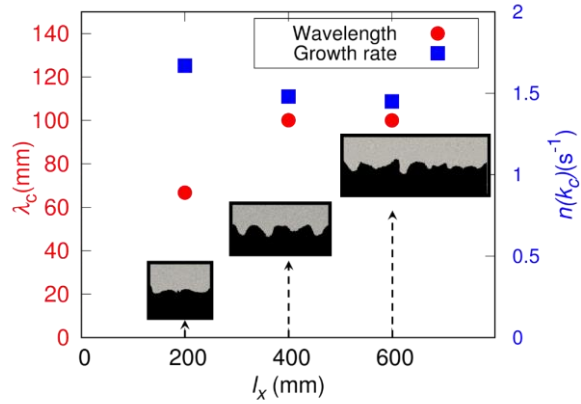

FIG 6.7. The characteristic wavelength (■) and its growth rate (●) as a function of system width l_x.

B. Role of system size

Figure 6.3 shows that fingers appear typically at both side walls, probably due to relatively large perturbations of the granular packing near the side walls (i.e., large gradients in solid fraction in the vicinity of the side walls). This

observation triggers the question of the effect of system size on the dynamics of granular fingering. To address this question, we have simulated systems of increasing widths, i.e., with l_0 = 200, 400 and 600 mm, while keeping the filling height constant at l_z = 200 mm. The characteristic wavelengths and corresponding growth rates obtained in these three systems are plotted in Figure 6.7. For the smallest system, i.e. l_x = 200 mm, the characteristic wavelength is lower, viz. λ_c = 66.7 mm than for the two wider systems. However, the characteristic wavelength reaches an asymptotic value of . $\lambda_c \sim$ 100 mm for $l_x \geq$ 400 mm. Inversely, the growth rate of the characteristic wavelength is higher for the smallest system size, i.e., $n(k_c)$ = 1.67 s^{-1} for l_x = 200 mm, but again reaches an asymptotic value of $n(k_c)$ = 1.45 s^{-1} for $l_x \geq$ 400 mm. These results suggest that for systems with a width $l_x \geq$ 400 mm the characteristic wavelength and growth rates become independent of system size.

C. Role of inter-particle friction

Previous research has suggested that particle friction, through its influence on the effective viscosity of the granular medium, affects the formation and dynamics of granular fingering (Pan, Joseph, and Glowinski 2001; McLaren et al. 2019; Jop, Forterre, and Pouliquen 2006). To probe its influence in more detail, we performed additional simulations with varying coefficients of particle friction μ_p and coefficients of restitution e. In these simulations the system width was set to l_x = 400 mm to eliminate any effect of the system size, while maintaining the computational efficiency of relatively small systems.

Figure 6.8(a) plots the initial growth rate of the characteristic wavenumber as a function of μ_p. For $\mu_p \geq 0.1$ the growth rate of the characteristic wavenumber reaches an asymptotic value of $n(k_c)$ = 1.45 s^{-1}, while for lower coefficients of friction the growth rate of the characteristic wavenumber increases strongly, reaching $n(k_c)$ = 5.3 s^{-1} for μ_p = 0. An increase of the growth rate of the characteristic wavenumber with decreasing μ_p is predicted also by classic RT theory (effective viscosity of dense granular media decrease with decreasing μ_p (Jop, Forterre, and Pouliquen 2006)). However, as plotted in Figure 6.8(b) the magnitude of the growth rate of the characteristic wavenumber for $\mu_p \rightarrow$ 0 ($n(k_c)$ = 5.3 s^{-1}) is very high; indeed, for $k \leq$ 0.02 mm^{-1} (k_c = 0.005 mm^{-1}) the

growth rates in a frictionless granular medium as determined from numerical simulations (◇ in Figured 6.8(b)), exceed the upper bound of the dispersion relation using classic, non-viscous RT theory (dashed line). On the other hand, the prediction of the classic RT theory (dash-dotted line) for a system with μ_p = 0.3 (η_{eff} = 1.95 Pa·s) agrees very well with the results of the numerical simulations (○ in Figured 6.8(b)). Based on our results of granular systems with varying coefficients of friction it appears that granular systems with $\mu_p \leq$ 0.1 are not predicted well by classic RT theory. The different behaviour of such systems is visualized in more detail in Figure 6.9(a–d). In Figure 6.9(a), i.e., μ_p = 0, we observe spikes at the fingers, while such spikes are absent in both classic RT fingers and in granular fingers for $\mu_p \geq$ 0.1 (Figure 6.9(d)). Such spike features, as observed for μ_p = 0, resemble structures that have been observed in the hydrodynamic Richtmyer-Meshkov (RM) instability (Richtmyer 1960). The RM instability occurs when a light fluid is accelerated into a heavy fluid by a shockwave or impulsive flow, which amplifies any perturbation of the interface due to the reflection of the shock wave at the interface.

Although the granular system that is studied here is not driven by impulsive flow, for the case μ = 0 we observe the upwards motion of void bands through the interface that could generate shock-like effects (Figure 6.9(e)). Importantly, the formation of such void bands is largely suppressed for $\mu_p \geq$ 0.1 (see Appendix 6C), since the injected vibrational energy is dissipated quickly through inter-particle friction. For $\mu_p <$ 0.1 void bands form at the bottom of the system and move upwards. Somewhat surprisingly, at the location of a finger, the void band is interrupted, while the void band exists at the left- and right-hand side of the finger (Δt = 1.0 s in Figure 6.9(e)). It appears that the spike-like features at the fingers arise due to particles being lifted up by the passing void band. Owing to the absence of friction, the finger is also growing faster in the lateral dimension compared to the dynamics of the fingers in the frictional cases (Figure 6.9(b–d)). Although there is some geometric similarity between the frictionless case and structures observed in RM instabilities, fingers still show an exponential growth rate in the frictionless case, while a linear growth rate would be expected for the RM instability. Interestingly, also for a gas-particle RM instability in which an explosive gas penetrates into a radial, granular Hele-Shaw cell, an exponential

finger growth has been reported (Xue et al. 2020) and it was also argued that high voidage due to dilation plays a key role in the observed RM instability.

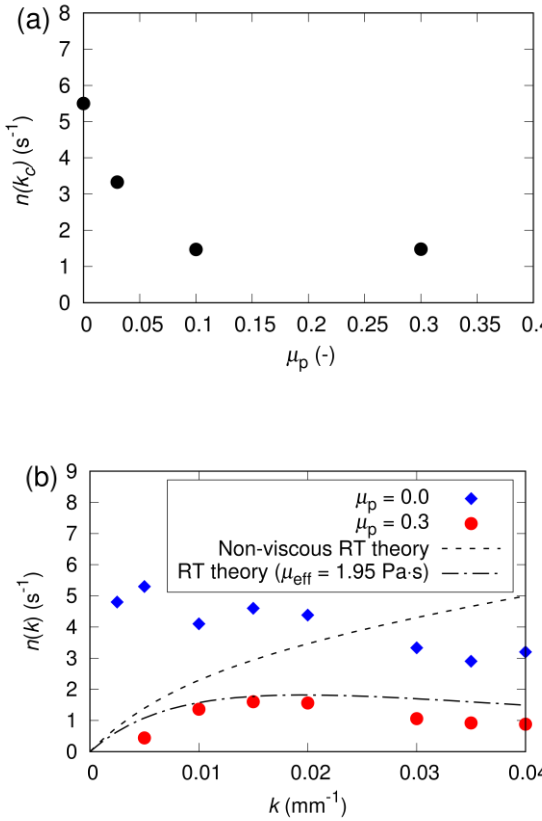

FIG 6.8. (a) Growth rate $n(k_c)$ of the characteristic wavenumber as a function of the coefficient of friction μ_p. (b) Dispersion relation between the growth rate, $n(k)$ and the wavenumber k. The markers plot data obtained from numerical simulations for $\mu_p = 0.0$ and $\mu_p = 0.3$. The corresponding granular viscosity for $\mu_p = 0.3$ is $\eta = 1.95$ Pa·s (using Eq. (6.12)). (– · –) Prediction of the classic RT theory for $\eta_{eff} = 1.95$ Pa·s. For $\mu_p = 0.0$ the system does not exhibit any RT-like instability, therefore Eq. (6.12) cannot be used to estimate

the granular viscosity. However, classic RT theory for non-viscous fluids (η_{eff} = 0 Pa·s) gives a theoretical upper bound for $n(k)$ which is given by (- - -).

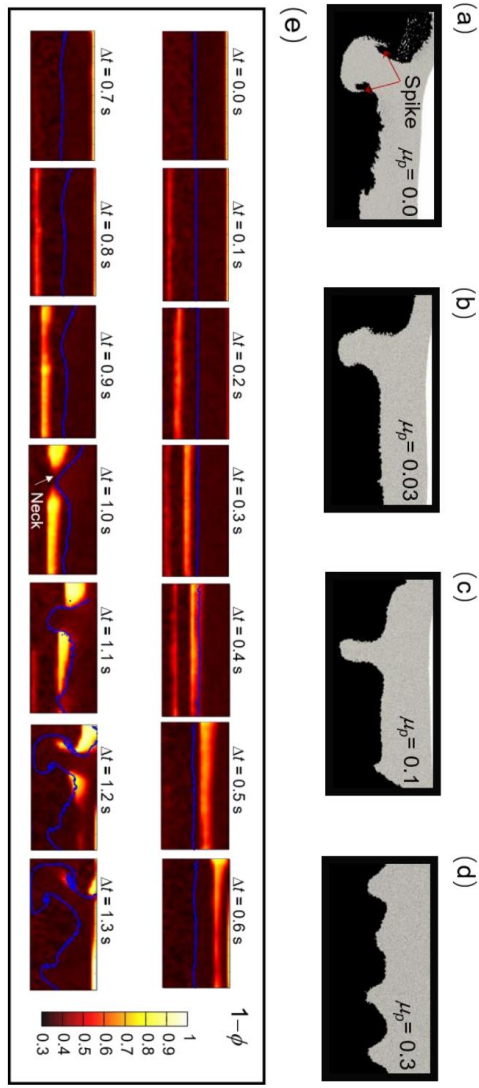

FIG 6.9(Continue to the next page)

Figure 6.9: (a), (b), (c), (d) Shape of the interface for varying coefficients of friction μ_p. (e) Time series visualizing the void fraction $(1-\phi)$ in a layered granular system using $\mu_p = 0$. The size of the numerical domain was $l_x \times l_y \times l_z = 400 \times 10 \times 200\ \text{mm}^3$. The blue line denotes the interface between the heavy and light particle layers.

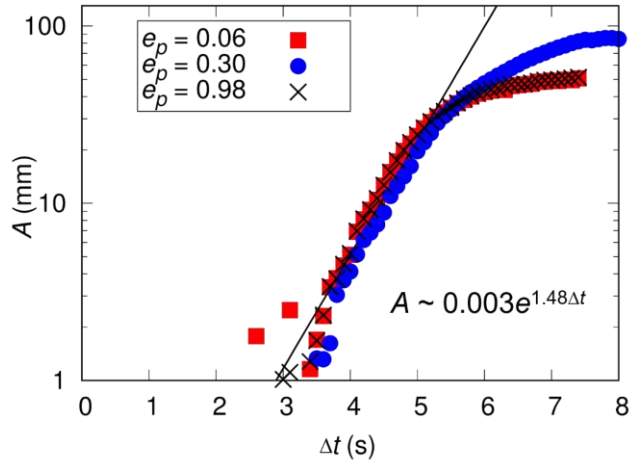

FIG 6.10. Influence of the coefficient of restitution e_p on the growth rate of the characteristic wavenumber. The solid line plots a (fitted) growth rate of 1.48 s^{-1}.

Unlike the coefficient of friction, the coefficient of restitution e_p is found to have a negligible effect on the dynamics of granular fingering. Simulating three granular systems with varying e_p, i.e., e_p = 0.06, 0.3, 0.98, we observe very similar initial growth dynamics as shown in Figure 6.10.

D. Yield criterion for granular RT instability

In the previous section it was discussed how the growth of perturbations at the interface of two layers of granular materials of different densities depend on inter-particle friction. However, Figures 6.3–6.5 also show that there is a

considerable time lag between the start of the agitation of the system and finger formation and growth to occur, suggesting that an initial resistance, i.e., a yield criterion, has to be overcome for fingers to form. The granular system considered here falls into the category of a dense granular system/flow owing to its high solid fraction of ~0.6. Similar to toothpaste, foam, etc., dense granular flows exhibit a viscoplastic-like behaviour, i.e., there exists a critical shear stress below which flow is not maintained and the rheology depends on the shear rate. A model that aims to describe the complex rheology of dense granular systems is the $\mu(I)$ model (Jop, Forterre, and Pouliquen 2006), whereby the inertial number I is a function of the particle size d, the particle density ρ_p, the shear rate $\dot{\gamma}$ and pressure P, viz. (da Cruz et al. 2005):

$$I = \frac{\dot{\gamma} d}{\sqrt{P / \rho_p}}. \tag{6.13}$$

The shear stress τ is expressed as a function of I as

$$\tau = \mu(I) P, \tag{6.14}$$

where $\mu(I)$ is bulk friction (different from the inter-particle friction) and given through an empirical friction law as (Jop, Forterre, and Pouliquen 2006, 2005):

$$\mu(I) = \mu_s + (\mu_2 - \mu_s) / (I_0 / I + 1). \tag{6.15}$$

Here, μ_s is a critical friction coefficient at zero shear rate which depends on the particle properties such as the coefficient of inter-particle friction and particle shape. The critical friction is $\mu_s \approx 0.38$ for spherical particle systems, based simulation and experimental results (Andreotti, Forterre, and Pouliquen 2013). In the following, $\mu_s = 0.38$ will be used for simplicity. The $\mu(I)$-rheology model is illustrated in Figure 6.11 and compared to a typical viscoplastic rheology model for fluids (see insert in Figure 6.11) which is described by:

$$\tau = \tau_y + \tau_s \dot{\gamma}^n (\dot{\gamma} / \dot{\gamma}_s)^n \tag{6.16}$$

where τ_y is the yield stress and n is the flow index. Similar to the yield stress in a viscoplastic fluid (dashed line in the insert in Figure 6.11), the yield stress for a dense granular system is given by:

$$\tau_y = \mu_s P . \tag{6.17}$$

Hence, the yield stress originates from the granular pressure P and is not an intrinsic property of a granular material (Trulsson et al. 2015). Furthermore, the yield criterion, Eq. (6.17), describes a yield transition from a static system. However, the present system is not static as the individual particles are agitated by vertical vibration and a fluidizing gas flow, yet the relative motion between heavy and light particles before fingering occurs is small, allowing to assume of a pseudo-static system. Furthermore, the following discussion is limited to $\mu_p \geq 0.1$ such that void bands are absent.

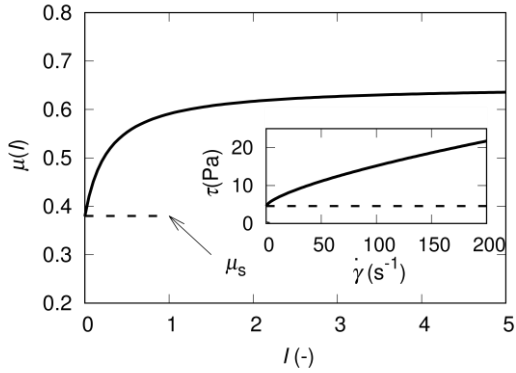

FIG 6.11. $\mu(I)$ local rheology model for a dense granular system given by Eq. (6.15); Insert: Herschel-Bulkley rheology model for an oil-based drilling fluid, i.e., a typical viscoplastic fluid (Saasen and Ytrehus 2018).

As buoyancy is the driving force for the granular RT instability, a yield parameter Y can be established as:

$$Y = \frac{(\varrho_H - \varrho_L)\phi g \lambda_c}{\tau_y}, \tag{6.18}$$

where λ_c is the characteristic wavelength of the granular RT instability, ϕ is the solid fraction of the bulk and ρ_H and ρ_L are densities of the heavy and light particle, respectively. The yield stress τ_y is given by Eq. (6.17), which requires information on the granular pressure P at the interface. The granular pressure at the interface can be determined from the inter-particle contact forces using coarse-graining (described in Appendix 6B). The pressure profile as a function of the vertical position z is initially hydrostatic, but very rapidly a pressure profile develops that leads to an instability at the interface, i.e., the higher granular pressure in the heavier particle layer pushes down onto a lower granular pressure in the layer containing the lighter particles (see Appendix 6D). Taking the granular pressure at the interface, i.e. $P(z = 100$ mm), we can calculate the yield parameter Y as given in Eq. (6.18). Figure 6.12 plots Y over time for systems of varying l_x and e_p, while the coefficient of inter-particle friction was fixed to $\mu_p = 0.3$. To determine the onset of exponential finger growth we calculate the intersection of a horizontal line fitted to the initial period where the amplitude of the characteristic wavenumber does not change (see Figure 6.5) and the exponential fit to the growth period (green line in Figure 6.5). In Figure 6.12 black symbols denote points in time in which no exponential finger growth was observed, while red symbols denote exponential finger growth. The results plotted in Figure 6.12 suggest a critical yield parameter of $Y_C = 15.7$ for RT-like finger instabilities to occur. Interestingly, this critical value of $Y_C = 15.7$ obtained here is very close to the value of $Y_C = 15 \pm 3.6$ that has been established for thermal plumes in the Earth's lower mantle to occur (which can also be classified as a visco-plastic material) (Davaille, Carrez, and Cordier 2018; Massmeyer et al. 2013). Similar to Eq. (6.18), also the yield parameter for a thermal plume is defined as the ratio of the buoyancy driven shear stress to the yield stress. Although the apparent similarities between the finger instabilities in granular materials as observed in this work and the rise of thermal plumes in the Earth's lower mantle suggest that the critical yield parameter value of $Y_C = 15$ might be a

more general scaling constant for the occurrence of fingering phenomena in viscoplastic fluids, further research is necessary to validate this hypothesis.

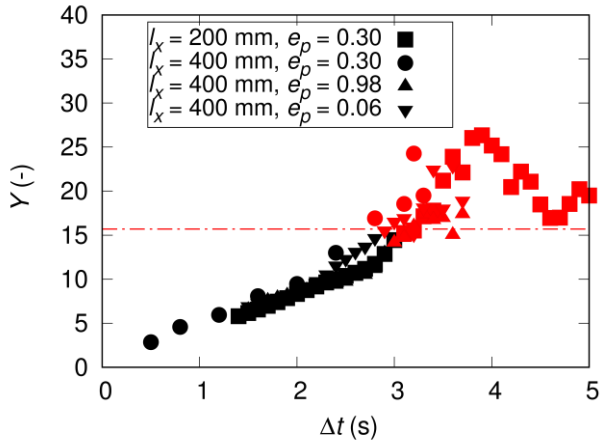

FIG 6.12. The yield parameter Y as a function of time. The onset of exponential finger growth is calculated as the intersection of a horizontal line fitted to the initial period when the amplitude of the characteristic wavenumber does not vary with time with an exponential fit to the growth period (see Figure 6.5). Black colour symbols indicate Δt for which no finger grow is observed, while red symbols denote Δt in which RT-like, exponential finger growth proceeds. The red dash-dotted line gives the critical yield parameter Y_C = 15.7±1.98. The data plotted are obtained from a series of systems with varying widths, l_x, and varying coefficients of restitution, e_p: (□) l_x = 200 mm, e_p = 0.30; (○) l_x = 400 mm, e_p = 0.30; (▽) l_x = 400 mm, e_p = 0.98; (△) l_x = 400 mm, e_p = 0.06; (○) l_x = 400 mm, e_p = 0.30. The coefficient of friction was fixed to μ_p = 0.3 in all simulations.

6.5 Conclusion

The present work investigates binary granular systems in which a granular medium of dense and small particles is layered on top of a granular medium of light and large particles. Finger instabilities akin to the hydrodynamic

Rayleigh-Taylor (RT) instability, emerge at the interface between the two granular media when agitated by a combination of vertical vibration and a fluidizing gas flow (McLaren et al. 2019). The results presented here confirm that classic RT instability theory can be used to describe the behaviour of fingering in dissipative binary granular systems (i.e., inter-particle friction coefficient $\mu_p \geq 0.1$) as:

- The characteristic wavenumber is constant over time.
- The initial growth rate of the characteristic wavenumber is exponential.
- The dispersion relation for the growth rate $n(k)$ as a function of the wavenumber k follows a very similar behaviour in the fluid and granular systems.

For $\mu_p < 0.1$ the system behaviour changes leading to the formation of spike-like features in the fingers which do not resemble a typical RT behaviour, but instead show some similarity to a Richtmyer-Meshkov-type instability. Our results also suggest that by treating the binary granular material ($\mu_p \geq 0.1$) as a viscoplastic material, we can define a yield criterion Y to predict the onset of fingering. If the yield criterion is below a critical value of $Y_c \approx 15$ fingering is not observed, while for $Y > 15$ fingers emerge and grow exponentially. A critical value of $Y_c \approx 15$ has also been found for other viscoplastic materials, such as the Earth's lower mantle in which thermal plumes rise for $Y > 15$ (Davaille, Carrez, and Cordier 2018; Massmeyer et al. 2013). This suggests that $Y_c = 15$ might be a general scaling constant for the emergence of instabilities in viscoplastic materials. However, further research is required to confirm this hypothesis.

Appendix 6A: Derivation of the dispersion relation

To derive an equation for the dispersion relation in binary granular systems we follow the approach of Bellman and Pennington (1954). As the transverse thickness (y direction) is very small compared to the other two dimensions,

the system can be considered 2D with a heavy granular medium on top of a light granular medium. The initial unperturbed interface is located at $z = 0$. In addition, surface tension can be neglected in granular systems. The goal is to find an equation

$$\frac{\partial u}{\partial x} + \frac{\partial v}{\partial z} = 0\,, \tag{6A1}$$

$$\frac{\partial u}{\partial t} = -\frac{1}{\varrho}\frac{\partial p}{\partial x} + \frac{\eta}{\varrho}\nabla^2 u\,, \tag{6A2}$$

$$\frac{\partial v}{\partial t} = -\frac{1}{\rho}\frac{\partial p}{\partial z} - g + \frac{\eta}{\varrho}\nabla^2 v\,, \tag{6A3}$$

where η is the dynamic viscosity, ρ is the density, and u and v are the velocity in the horizontal and vertical direction, respectively. By introducing the potential functions Θ and Ψ, the solutions for Eq. (6A1–6A3) can be obtained as:

$$u = -\frac{\partial \Theta}{\partial x} - \frac{\partial \psi}{\partial z}\,, \tag{6A4}$$

and

$$v = \frac{\partial \psi}{\partial x} - \frac{\partial \Theta}{\partial z}\,. \tag{6A5}$$

The pressure is given by the Bernoulli equation,

$$p = p_0 - g z(x,t) - \frac{\partial \Theta}{\partial t}\,. \tag{6A6}$$

where p_0 is the mean pressure at the (unperturbed) interface. Substituting Eq. (6A4) and (6A5) into Eq. (6A1–6A3) yields:

$$\Delta\Theta = 0\,, \tag{6A7}$$

$$\frac{\partial\Psi}{\partial t} = \frac{\eta}{\varrho}\Delta\Psi\,. \tag{6A8}$$

Solutions for the potential functions Θ and Ψ which satisfy (6A7) and (6A8) are given by Lamb (1924); the solutions for the heavy and light granular medium are denoted by subscript H and L, viz.:

$$\begin{bmatrix}\Theta_H\\ \Theta_L\end{bmatrix} = \begin{bmatrix}Ae^{-Kz+nt}\cos(Kx)\\ Ce^{Kz+nt}\cos(Kx)\end{bmatrix}, \tag{6A9}$$

$$\begin{bmatrix}\psi_H\\ \psi_L\end{bmatrix} = \begin{bmatrix}Be^{-m_H z+nt}\sin(Kx)\\ De^{-m_L z+nt}\sin(Kx)\end{bmatrix}, \tag{6A10}$$

where ${m_H}^2 = K^2 + \frac{n\phi\varrho_H}{\eta_H}$, ${m_L}^2 = K^2 + \frac{n\phi\varrho_L}{\eta_L}$ and n is the growth rate of a given wavenumber k ($K = 2\pi k$). The pressure in both granular media is:

$$\begin{bmatrix}p_H\\ p_L\end{bmatrix} = \begin{bmatrix}p_0 - gz(x,t)\phi\varrho_H - \phi\varrho_H\dfrac{\partial\Theta_H}{\partial t}\\[2ex] p_0 - gz(x,t)\phi\varrho_L - \phi\varrho_L\dfrac{\partial\Theta_L}{\partial t}\end{bmatrix}\,. \tag{6A11}$$

The boundary conditions at the interface between the two media are:

$$u_H = u_L,\ v_H = v_L\,, \tag{6A12}$$

$$-p_H + 2\eta_H\frac{\partial v_H}{\partial z} = -p_L + 2\eta_L\frac{\partial v_L}{\partial z}\,, \tag{6A13}$$

$$\eta_H\left(\frac{\partial v_H}{\partial x}+\frac{\partial u_H}{\partial z}\right)=\eta_L\left(\frac{\partial v_L}{\partial x}+\frac{\partial u_L}{\partial z}\right). \tag{6A14}$$

The vertical velocity of the interface v is obtained by taking the partial differential of $z(x,t)$ with respect to t yielding:

$$v-\frac{\partial z}{\partial x}u-\frac{\partial z}{\partial t}=0. \tag{6A15}$$

Assuming that the initial perturbation has a small amplitude compared to its wavelength, the nonlinear term $(\partial z/\partial x)u$ in Eq. (6A15) can be neglected:

$$\frac{\partial z}{\partial t}=v. \tag{6A16}$$

Since $v = v_H = v_L$, see Eq. (6A12), we can calculate v by substituting Eq. (6A9) and Eq. (6A10) into Eq. (6A5) and integrate over t to obtain $z(x, t)$ as:

$$z=K(A+B)n^{-1}e^{nt}\cos Kx. \tag{6A17}$$

In this equation the constants A and B are still unknown. The constants A and B (and C, D) are determined by substituting Eq. (6A9) and (A10) into Eq. (6A4) and (6A5) and the resulting equation into the boundary conditions given by Eq. (6A12–6A14). This yields a system of four equations that are linear in A, B, C and D (curious readers find the system in Bellman and Pennington (1954) as equation (2.20)). A non-trivial solution for the system of equations exists if the determinant of the coefficient matrix of the four linear equations is zero, which yields the implicit dispersion relation:

$$\begin{aligned}&\left[-\beta+\phi(\varrho_H+\varrho_L)n^2\right]\left[(\eta_H K+\eta_L m_L)+(\eta_L K+\eta_H m_H)\right]+\\&4nK\left(\eta_H K+\eta_L m_L\right)\left(\eta_L K+\eta_H m_H\right)=0\end{aligned}. \tag{6A18}$$

If β is positive, there will be at least one root of n that has a positive real part, i.e., the interface is unstable, and any perturbation of the interface grows in amplitude. As expected, this is the case if $\varrho_H > \varrho_L$.

In a final step we rewrite the implicit dispersion relation given by Eq. (6A18) using the definitions for m_H and m_L to obtain:

$$\left[-gf(\varrho_H-\varrho_L)K+\phi(\varrho_L+\varrho_H)n(K)^2\right]M+4n(K)K=0\,, \qquad (6A19)$$

Where M is

$$M=\frac{1}{\eta_H K+(\eta_L^2K^2+\phi\varrho_L n(K)\eta_L)^{1/2}} + \frac{1}{\eta_L K+(\eta_H^2K^2+\phi\varrho_H n(K)\eta_H)^{1/2}}\,. \qquad (6A20)$$

Appendix 6B: Coarse-graining method

Here we use coarse-graining (CG) as described in Goldhirsch (2010) to obtain the granular pressure. To this end, we define a CG volume, which is bounded by a sphere located at $\mathbf{r}$ with radius w. The CG density at $\mathbf{r}$ is defined as,

$$\varrho(\mathbf{r},t)=\sum_{i=1}^{N} m_i G(\mathbf{r}-\mathbf{r}_i(t))\,, \qquad (6B1)$$

where the sum is taken over the particles located in the CG volume and $G(\mathbf{r}-\mathbf{r}_i(t))$ is the CG function. Here, we have chosen the Heaviside function $G(\mathbf{r})=H(w-\|\mathbf{r}\|)/V$ as the CG function, where V is the volume of the CG sphere. The solid fraction is calculated as,

$$\phi=\varrho(\mathbf{r},t)/\varrho_p\,, \qquad (6B2)$$

where ϱ_p is the particle density. The CG moment density is given as,

$$\varrho(\mathbf{r},t)\mathbf{u}(\mathbf{r},t)=\sum_{i=1}^{N} m_i G(\mathbf{r}-\mathbf{r}_i(t))\cdot\mathbf{u}(\mathbf{r}_i,t)\,, \tag{6B3}$$

and the CG velocity is calculated via

$$\mathbf{u}(\mathbf{r},t)=\sum_{i=1}^{N} m_i G(\mathbf{r}-\mathbf{r}_i(t))\cdot\mathbf{u}(\mathbf{r}_i,t)\,/\,\varrho(\mathbf{r},t)\,. \tag{6B4}$$

The CG stress tensor is derived based on the momentum conservation equation as:

$$\begin{aligned}\sigma_{\alpha\beta}(\mathbf{r},t)=&-\frac{1}{2}\sum_{i,j}\mathbf{f}_a^{i,j}(t)\mathbf{r}_\beta^{i,j}\int_0^1 ds\left(G(\mathbf{r}-\mathbf{r}_j(t)+s\mathbf{r}_{ij}(t)\right)\\&-\sum_{\mathrm{i}} m_i u_a^{i'}(t)u_\beta^{i'}(t)G(\mathbf{r}-\mathbf{r}_i(t))\end{aligned}\,, \tag{6B5}$$

where α, β denote the Cartesian coordinates x, y, z, $\mathbf{f}_a^{i,j}$ is the α-th component of the inter-particle contact force of the contacting particles i and j, $\mathbf{r}_\beta^{i,j}$ is the vector that points from the position of particle i to particle j and $u_a^{i'}$ is the fluctuation of the velocity of particle i with respect to the CG velocity $u(\mathbf{r},t)$. The granular pressure is given by the trace of the stress tensor, i.e., $P = 1/3(\sigma_{xx}+\sigma_{yy}+\sigma_{zz})$.

Appendix 6C: Void fraction for $\mu_p \geq 0.1$

In Figure 6.10(d) we observe the rise of void bands through a binary granular system when using a low inter-particle friction coefficient, i.e., $\mu_p < 0.1$. Formation of these void bands is largely supressed for $\mu_p \geq 0.1$ which is visualized in Figure 6C1.

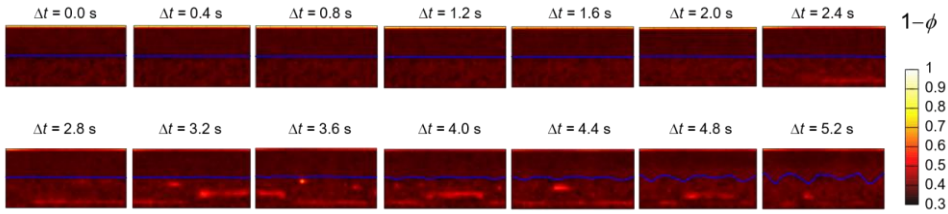

FIG 6C1. Time series of the void fraction ($1-\phi$) in a numerical system using an inter-particle friction coefficient of $\mu_p = 0.3$. The blue line denotes the interface between the heavy and light granular medium.

Appendix 6D: Granular pressure profile

Figure 6D1 plots the granular pressure (averaged along the x and y directions) in the system as a function of height (z direction) for different times Δt. The pressure profile is initially hydrostatic ($\Delta t = 0.2$ s), very rapidly a pressure profile develops that leads to an instability at the interface ($z \sim 100$ mm), i.e. a higher granular pressure in the heavier particle layer ($z > 100$ mm) pushes down onto a lower granular pressure in the lighter particle layer ($z < 100$ mm).

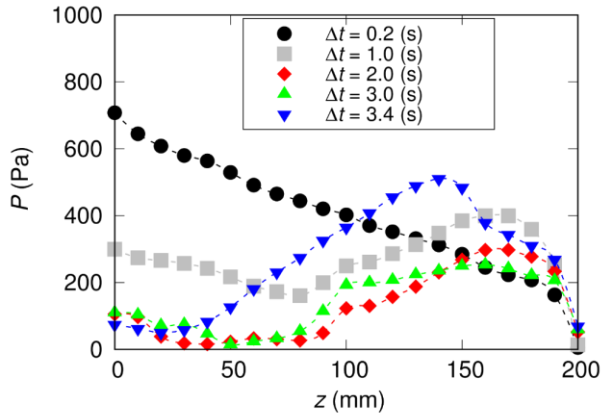

FIG 6D1. Granular pressure P as a function of the height (z) for different instants in time Δt.

CONCLUSIONS AND OUTLOOK 7

7.1 Conclusions

This thesis has explored two important phenomena in granular materials, i.e., segregation and stability of granular interfaces. Using a series of different modelling approaches, the lift force acting on intruders, granular buoyancy and a fingering instability has been described successfully. The following conclusions were drawn from this work.

We were able to verify the validity of a generalization of the Archimedean formulation of the granular buoyancy force that has been proposed originally for shear flows for vibro-fluidized systems. To exclude the influence of drag forces, a convection-free system was considered. Such as system was established through vibrating sidewalls and a friction coefficient of zero for particle-wall contacts. The buoyancy force calculated through the generalized Archimedean formulation, i.e., considering the Voronoi volume of the intruder, agreed very well with the values obtained from its hydrostatic definition (pressure gradient) and its direct measurement through a virtual spring. The complexity of the model system explored was subsequently increased by including also convection (through a non-zero particle-wall friction coefficient). The segregating (lift) force acting on an intruder in such a system is affected by buoyancy and drag and increases with increasing intruder size, but it is independent of the vibration strength Γ (for $\Gamma > 6$) and the intruder density. We demonstrate that a lift force model that combines buoyancy (expressed through the generalized Archimedean formulation) and a drag force (velocity-independent in the considered slow-velocity regime) predicts very accurately the magnitude of the lift force obtained through a virtual spring. This model allowed us to rationalize the independence of the segregation (lift) force on the intruder density and the vibration strength (once a critical value of $\Gamma_{cr} = 6$ is exceeded).

In addition we have proposed a new lift force model for intruders in dense, granular shear flows by extending the work of Trujillo and Herrmann (2003). We interpret the lift force as a buoyancy force whereby the density difference arises both from granular temperature and granular pressure disturbances induced by intruder. We observe that the presence of an intruder leads to a cooling effect and a local flattening of the shear velocity profile (lower shear rate). For large intruders, i.e., $d_I/d_p > 4$, the local pressure disturbance (and hence contribution to the lift force) is very small as the system approaches a continuum limit, in which the pressure acting on the intruder equals to the hydrostatic pressure of the system. On the other hand, for $1 < d_I/d_p < 4$ the local granular pressure at the location of the intruder is lower than the hydrostatic pressure leading in turn to a positive lift force. The cooling effect due to the presence of an intruder increases with intruder size, leading ultimately to the sinking of large intruders. The modified model predicts the DEM-determined lift forces very well and allows the description of a neutral buoyancy limit.

Finally, we investigated binary granular systems in which a granular medium of dense and small particles is layered on top of a granular medium of light and large particles. Finger instabilities akin to the hydrodynamic Rayleigh-Taylor (RT) instability emerge at the interface between the two granular media when agitated by a combination of vertical vibration and a fluidizing gas flow. The results presented here confirm that classic RT instability theory can be used to describe the behavior of fingering in dissipative binary granular systems (i.e. inter-particle friction coefficient $\mu_p \geq 0.1$) in that: (i) The characteristic wavenumber is constant over time; (ii) the initial growth rate of the characteristic wavenumber is exponential and (iii) the dispersion relation for the growth rate $n(k)$ as a function of wavenumber k follows a very similar behavior. For $\mu_p < 0.1$ the system behavior changes leading to the formation of spike-like features in the fingers which do not resemble a typical RT behavior, but instead show some similarity to a Richtmyer-Meshkov-type instability. Our results also suggest that by treating the binary granular material ($\mu_p \geq 0.1$) as a viscoplastic material, we can define a yield criterion Y to predict the onset of fingering. If the yield criterion is below a critical value of $Y_c \approx 15$ fingering is not observed, while for $Y > 15$ fingers emerge and grow exponentially. A critical value of $Y_c \approx 15$ has also been found for other

viscoplastic materials, such as the Earth's lower mantle in which thermal plumes rise for $Y > 15$ (Davaille, Carrez, and Cordier 2018; Massmeyer et al. 2013). This suggests that $Y_c = 15$ might be a general scaling constant for the emergence of instabilities in viscoplastic materials. However, further research is required to confirm this hypothesis.

Our work has shed some light on segregation and the stability of interfaces in granular materials. Based on the results obtained here, the following future works are proposed.

Segregation

In chapter 4 a continuum perspective to model segregation is introduced. In general, granular systems also contain convective patterns, which require the segregating force to also include a drag force component. Several works have revealed that in granular media the drag force acting on an intruder is independent of the velocity of the intruder for slowly moving intruders (quasi-static regime in which friction and gravity dominate) (Albert et al. 2001). For rapidly moving intruders (inertial regime) the drag force was found to scale with the velocity of the intruder squared (Faug 2015). While there has been extensive research on the drag force acting on intruders in static granular systems, the drag force is under-explored in flowing granular systems and it has to be assessed how the relative velocity of the intruder and granular media can be described most accurately (van der Vaart et al. 2018; Tripathi and Khakhar 2011). Eventually, the predictive nature of a drag force model for intruders moving in a dynamic granular system has to be assessed in a system containing a freely moving intruder, i.e. without it being connected to a virtual spring (Staron 2018)

This work has focus on the segregation of a single intruder, which is a well describable, model system. However, an important question is whether the models obtained here are also valid for systems that contain multiple intruders and whether there is an intruder concentration at which certain assumptions break down. It is expected that a high concentration of intruders will affect the segregation flux. Indeed, it has been reported that intruders segregate faster in systems of a higher intruder concentration compared to systems with a lower intruder concentration (Gajjar and Gray 2014; Jones et al. 2018). While previous studies have assumed that there is a linear dependence between the lift force and the intruder concentration (Gray and Thornton 2005), recent works have indicated that this assumption might not be correct. For example,

for intruder (d_I/d_p = 3) concentrations < 50 %, the lift force acting on an intruder was found to be nearly independent of the intruder concentration, while the lift force decreased with intruder concentrations, for concentrations > 50 %. Hence, the cooperative dynamics of multiple intrudes require further studies.

In Chapter 5 we derive an expression for the lift force acting on an intruder from a thermodynamic description of granular materials. While the model shows good agreement with (numerical) measurements, several key questions require further work. For example, the equation of state of granular materials, i.e. the correlation between granular pressure, temperature and solid fraction is not well developed, in particular for dense granular systems which are particularly interesting for engineering applications (Kim and Kamrin 2020; Taylor and Brodsky 2017). We feel that size differences between the intruder and bed particles need to be considered in such a correlation, i.e., correlations for bi- or multi-disperse granular systems are required. Recent work suggests that an equation of state for a binary mixture of hard spheres allows to calculate the buoyancy force acting on intruders for systems of different intruder concentrations (Kumar, Khakhar, and Tripathi 2019). Hence, further work on the establishment of such correlations is crucial to further refine lift force models, i.e., to develop models that link the granular temperature/pressure disturbance (induced by the intruder) to flow parameters such as shear rate, shear rate gradient, etc. In addition, the lift force model proposed here was developed and validated for a steady-state dense shear flow system, it would be interesting to investigate whether the model can be applied also to dynamic granular systems, e.g., wall-driven flow, silo flow or vibrofluidzed beds.

Chapter 6 studies granular interface instabilities, i.e., a granular Rayleigh-Taylor-type instability and a Richtmyer-Meshkov-type instability. As a next step we propose to extent the experimental work to determine if the instability can be triggered by vibration alone which would be of practical importance. Furthermore, we established a critical yield parameter for the granular RT instability, which coincides with the critical yield value for plumes rising in the lower Earth mantle. It would be interesting to assess whether this yield criterion is also valid in further granular systems such as shear driven granular systems (D'Ortona and Thomas 2020). For the granular instability to occur a

reasonably large system is often required. Such large systems are challenging for computer simulations making it difficult to probe numerically for example the granular Taylor-vortex. Hence more efficient modelling approaches are required. Recently, a method called material point method (Bardenhagen, Brackbill, and Sulsky 2000) has shown some promising results to simulate large particle systems (Hu et al. 2019; Li et al. 2021). However, it is unclear whether this method is able to reproduce well instability phenomena in granular systems, hence requiring further validation and potentially further development.

Albert, I., J. G. Sample, A. J. Morss, S. Rajagopalan, A. L. Barabasi, and P. Schiffer. 2001. 'Granular drag on a discrete object: Shape effects on jamming', *Physical Review E*, 64: 061303.

Albert, R., M. A. Pfeifer, A. L. Barabasi, and P. Schiffer. 1999. 'Slow drag in a granular medium', *Physical Review Letters*, 82: 205-08.

Amon, A., P. Born, K. E. Daniels, J. A. Dijksman, K. Huang, D. J. Parker, M. Schröter, R. Stannarius, and A. Wierschem. 2017. "Preface: Focus on imaging methods in granular physics." In, 051701. AIP Publishing LLC.

Andreotti, B., Y. Forterre, and O. Pouliquen. 2013. *Granular media: between fluid and solid* (Cambridge University Press).

Antypov, D., and J. A. Elliott. 2011. 'On an analytical solution for the damped Hertzian spring', *Europhysics Letters*, 94: 50004.

Aranson, I. S., and L. S. Tsimring. 2001. 'Continuum description of avalanches in granular media', *Physical Review E*, 64.

Aranson, I. S., and L. S. Tsimring. 2006. 'Patterns and collective behavior in granular media: Theoretical concepts', *Reviews of Modern Physics*, 78: 641.

Asenjo, D., F. Paillusson, and D. Frenkel. 2014. 'Numerical Calculation of Granular Entropy', *Physical Review Letters*, 112.

Babic, M. 1997. 'Average balance equations for granular materials', *International Journal of Engineering Science*, 35: 523-48.

Bagnold, R. A. 1954. 'Experiments on a Gravity-Free Dispersion of Large Solid Spheres in a Newtonian Fluid under Shear', *Proceedings of the Royal Society of London Series a-Mathematical and Physical Sciences*, 225: 49-63.

Bardenhagen, S. G., J. U. Brackbill, and D. Sulsky. 2000. 'The material-point method for granular materials', *Computer methods in applied mechanics*, 187: 529-41.

Bartelt, P., and B. W. McArdell. 2009. 'Granulometric investigations of snow avalanches', *Journal of Glaciology*, 55: 829-33.

Baule, A., F. Morone, H. J. Herrmann, and H. A. Makse. 2018. 'Edwards statistical mechanics for jammed granular matter', *Reviews of Modern Physics*, 90.

Bellman, R., and R. H. Pennington. 1954. 'Effects of Surface Tension and Viscosity on Taylor Instability', *Quarterly of Applied Mathematics*, 12: 151-62.

Bensimon, D., L. P. Kadanoff, S. D. Liang, B. I. Shraiman, and C. Tang. 1986. 'Viscous flows in two dimensions', *Review of Modern Physics*, 58: 977.

Bocquet, L., W. Losert, D. Schalk, T. C. Lubensky, and J. P. Gollub. 2001. 'Granular shear flow dynamics and forces: Experiment and continuum theory', *Physical Review E*, 65: 011307.

Bouzid, M., M. Trulsson, P. Claudin, E. Clement, and B. Andreotti. 2013. 'Nonlocal Rheology of Granular Flows across Yield Conditions', *Physical Review Letters*, 111.

Brown, R. L. 1939. 'The fundamental principles of segregation', *Journal of the Institute of Fuel*, 13: 15-23.

Burtally, N., P. J. King, and M. R. Swift. 2002. 'Spontaneous air-driven separation in vertically vibrated fine granular mixtures', *Science*, 295: 1877-9.

Campbell, C. S., and A. Gong. 1986. 'The Stress Tensor in a Two-Dimensional Granular Shear-Flow', *Journal of Fluid Mechanics*, 164: 107-25.

Chandrasekhar, Subrahmanyan. 2013. *Hydrodynamic and hydromagnetic stability* (Courier Corporation).

Chen, S. J., R. X. Cai, Y. Zhang, H. R. Yang, H. Zhang, and J. F. Lyu. 2021. 'A semi-empirical model to estimate the apparent viscosity of dense, bubbling gas-solid suspension', *Powder Technology*, 377: 289-96.

Cheng, X., L. Xu, A. Patterson, H. M. Jaeger, and S. R. Nagel. 2008. 'Towards the zero-surface-tension limit in granular fingering instability', *Nature Physics*, 4: 234-37.

Chevalier, C., M. Ben Amar, D. Bonn, and A. Lindner. 2006. 'Inertial effects on Saffman-Taylor viscous fingering', *Journal of Fluid Mechanics*, 552: 83-97.

Ciamarra, M. P., A. Coniglio, and M. Nicodemi. 2006. 'Thermodynamics and statistical mechanics of dense granular media', *Physical Review Letters*, 97.

Colafigli, A., L. Mazzei, P. Lettieri, and L. Gibilaro. 2009. 'Apparent viscosity measurements in a homogeneous gas-fluidized bed', *Chemical Engineering Science*, 64: 144-52.

Conway, S. L., T. Shinbrot, and B. J. Glasser. 2004. 'A Taylor vortex analogy in granular flows', *Nature*, 431: 433-37.

Conzelmann, N. A., A. Penn, M. N. Partl, F. J. Clemens, L. D. Poulikakos, and C. R. Muller. 2020. 'Link between packing morphology and the distribution of contact forces and stresses in packings of highly nonconvex particles', *Physical Review E*, 102.

Cooke, W., S. Warr, J. M. Huntley, and R. C. Ball. 1996. 'Particle size segregation in a two-dimensional bed undergoing vertical vibration', *Physical Review E*, 53: 2812-22.

Crosta, G. B., H. Chen, and C. F. Lee. 2004. 'Replay of the 1987 Val Pola Landslide, Italian Alps', *Geomorphology*, 60: 127-46.

Cundall, P. A., and O. D. L. Strack. 1979. 'Discrete Numerical-Model for Granular Assemblies', *Geotechnique*, 29: 47-65.

D'Ortona, U., and N. Thomas. 2020. 'Self-Induced Rayleigh-Taylor Instability in Segregating Dry Granular Flows', *Physical Review Letters*, 124.

da Cruz, F., S. Emam, M. Prochnow, J. N. Roux, and F. Chevoir. 2005. 'Rheophysics of dense granular materials: Discrete simulation of plane shear flows', *Physical Review E.*, 72.

Davaille, A., P. Carrez, and P. Cordier. 2018. 'Fat Plumes May Reflect the Complex Rheology of the Lower Mantle', *Geophysical Research Letters*, 45: 1349-54.

de Gennes, P. G. 1999. 'Granular matter: a tentative view', *Reviews of Modern Physics*, 71: S374-S82.

Derec, C., A. Ajdari, and F. Lequeux. 2001. 'Rheology and aging: A simple approach', *European Physical Journal E*, 4: 355-61.

Duan, Y. F., P. B. Umbanhowar, J. M. Ottino, and R. M. Lueptow. 2021. 'Modelling segregation of bidisperse granular mixtures varying simultaneously in size and density for free surface flows', *Journal of Fluid Mechanics*, 918.

Duran, J, J Rajchenbach, and E Clément. 1993. 'Arching effect model for particle size segregation', *Physical Review Letters*, 70: 2431.

Duran, J., T. Mazozi, E. Clement, and J. Rajchenbach. 1994. 'Size Segregation in a 2-Dimensional Sandpile - Convection and Arching Effects', *Physical Review E*, 50: 5138-41.

Duran, J., J. Rajchenbach, and E. Clement. 1993. 'Arching Effect Model for Particle-Size Segregation', *Physical Review Letters*, 70: 2431-34.

Edwards, S. F. 1994. 'The role of entropy in the specification of a powder.' in, *Granular Matter* (Springer).

Edwards, S. F., and R. B. S. Oakeshott. 1989. 'Theory of Powders', *Physica A*, 157: 1080-90.
Faug, T. 2015. 'Macroscopic force experienced by extended objects in granular flows over a very broad Froude-number range', *The European Physical Journal E*, 38: 1-10.
Felix, G., and N. Thomas. 2004. 'Evidence of two effects in the size segregation process in dry granular media', *Physical Review E*, 70.
Ferdowsi, B., C. P. Ortiz, M. Houssais, and D. J. Jerolmack. 2017. 'River-bed armouring as a granular segregation phenomenon', *Nature Communications*, 8.
Forterre, Y., and O. Pouliquen. 2008. 'Flows of dense granular media', *Annual Review of Fluid Mechanics*, 40: 1-24.
Gajjar, P., and J. M. N. T. Gray. 2014. 'Asymmetric flux models for particle-size segregation in granular avalanches', *Journal of Fluid Mechanics*, 757: 297-329.
Garzó, V, and J. W. Dufty. 1999. 'Dense fluid transport for inelastic hard spheres', *Physical Review E*, 59: 5895.
Garzo, V. 2008. 'Brazil-nut effect versus reverse Brazil-nut effect in a moderately dense granular fluid', *Physical Review E*, 78.
Gillemot, K. A., E. Somfai, and T. Borzsonyi. 2017. 'Shear-driven segregation of dry granular materials with different friction coefficients', *Soft Matter*, 13: 415-20.
Glasser, B. J., and I. Goldhirsch. 2001. 'Scale dependence, correlations, and fluctuations of stresses in rapid granular flows', *Physics of Fluids*, 13: 407-20.
Goldenberg, C., A. P. F. Atman, P. Claudin, G. Combe, and I. Goldhirsch. 2006. 'Scale separation in granular packings: Stress plateaus and fluctuations', *Physical Review Letters*, 96.
Goldhirsch, I. 1999. 'Scales and kinetics of granular flows', *Chaos*, 9: 659-72.
Goldhirsch, Isaac. 2010. 'Stress, stress asymmetry and couple stress: from discrete particles to continuous fields', *Granular Matter*, 12: 239-52.
Goniva, C., C. Kloss, N. G. Deen, J. A. M. Kuipers, and S. Pirker. 2012. 'Influence of rolling friction on single spout fluidized bed simulation', *Particuology*, 10: 582-91.
Gray, J. M. N. T., and A. R. Thornton. 2005. 'A theory for particle size segregation in shallow granular free-surface flows', *Proceedings of the Royal Society a-Mathematical Physical and Engineering Sciences*, 461: 1447-73.

Guillard, F., Y. Forterre, and O. Pouliquen. 2016. 'Scaling laws for segregation forces in dense sheared granular flows', *Journal of Fluid Mechanics*, 807.

Haff, P. K. . 1983. 'Grain flow as a fluid-mechanical phenomenon', *Journal of Fluid Mechanics*, 134: 401-30.

Hamzeloo, E., M. Massinaei, and N. Mehrshad. 2014. 'Estimation of particle size distribution on an industrial conveyor belt using image analysis and neural networks', *Powder Technology*, 261: 185-90.

Harrison, W. J. . 1908. 'The influence of viscosity on the oscillations of superposed fluids', *Proceedings of the London Mathematical Society*, 2: 396-405.

Heckel, R. W. 1961. 'Density-Pressure Relationships in Powder Compaction', *Transactions of the Metallurgical Society of Aime*, 221: 671-75.

Herrmann, H. J. 1993. 'On the thermodynamics of granular media', *Journal De Physique Ii*, 3: 427-33.

Hill, K. M., A. Caprihan, and J. Kakalios. 1997. 'Axial segregation of granular media rotated in a drum mixer: Pattern evolution', *Physical Review E*, 56: 4386.

Hill, K. M., and Y. Fan. 2008. 'Isolating segregation mechanisms in a split-bottom cell', *Physical Review Letters*, 101.

Hill, K. M., and D. S. Tan. 2014. 'Segregation in dense sheared flows: gravity, temperature gradients, and stress partitioning', *Journal of Fluid Mechanics*, 756: 54-88.

Hill, R. J., D. L. Koch, and A. J. C. Ladd. 2001. 'The first effects of fluid inertia on flows in ordered and random arrays of spheres', *Journal of Fluid Mechanics*, 448: 213-41.

Hilton, J. E., and P. W. Cleary. 2011. 'The influence of particle shape on flow modes in pneumatic conveying', *Chemical Engineering Science*, 66: 231-40.

Hong, D. C., P. V. Quinn, and S. Luding. 2001. 'Reverse Brazil nut problem: Competition between percolation and condensation', *Physical Review Letters*, 86: 3423-26.

Hu, Y. M., L. Anderson, T. M. Li, Q. Sun, N. Carr, J. Ragan-Kelley, and F. Durand. 2019. 'Difftaichi: Differentiable programming for physical simulation', *arXiv:1910. 00935*.

Huang, H. Y., F. S. Zhang, P. Callahan, and J. Ayoub. 2012. 'Granular Fingering in Fluid Injection into Dense Granular Media in a Hele-Shaw Cell', *Physical Review Letters*, 108.

Huerta, D. A., and J. C. Ruiz-Suarez. 2004. 'Vibration-induced granular segregation: A phenomenon driven by three mechanisms', *Physical Review Letters*, 92.

Huerta, D. A., V. Sosa, M. C. Vargas, and J. C. Ruiz-Suarez. 2005. 'Archimedes' principle in fluidized granular systems', *Physical Review E*, 72.

Jaeger, H. M., S. R. Nagel, and R. P. Behringer. 1996. 'Granular solids, liquids, and gases', *Reviews of Modern Physics*, 68: 1259-73.

Janda, A., D. Maza, A. Garcimartin, E. Kolb, J. Lanuza, and E. Clement. 2009. 'Unjamming a granular hopper by vibration', *Europhysics Letters*, 87.

Janssen, H. A. 1895. 'Versuche uber getreidedruck in silozellen', *Z. Ver. Dtsch. Ing.*, 39: 1045-49.

Jenkins, J. T., and D. Berzi. 2010. 'Dense inclined flows of inelastic spheres: tests of an extension of kinetic theory', *Granular Matter*, 12: 151-58.

Jenkins, J. T., and D. K. Yoon. 2002. 'Segregation in binary mixtures under gravity', *Physical Review Letters*, 88.

Jenkins, James T. 2006. 'Dense shearing flows of inelastic disks', *Physics of Fluids*, 18: 103307.

Jing, L., J. M. Ottino, R. M. Lueptow, and P. B. Umbanhowar. 2020. 'Rising and sinking intruders in dense granular flows', *Physical Review Research*, 2.

Jing, L., J. M. Ottino, R. M. Lueptow, and P. B. Umbanhowar. 2021. 'A unified description of gravity-and kinematics-induced segregation forces in dense granular flows', *Journal of Fluid Mechanics*, 925.

Johnsen, O., R. Toussaint, K. J. Maloy, and E. G. Flekkoy. 2006. 'Pattern formation during air injection into granular materials confined in a circular Hele-Shaw cell', *Physical Review E*, 74.

Jones, R. P., A. B. Isner, H. Y. Xiao, J. M. Ottino, P. B. Umbanhowar, and R. M. Lueptow. 2018. 'Asymmetric concentration dependence of segregation fluxes in granular flows', *Physical Review Fluids*, 3: 094304.

Jop, P., Y. Forterre, and O. Pouliquen. 2005. 'Crucial role of sidewalls in granular surface flows: consequences for the rheology', *Journal of Fluid Mechanics*, 541: 167-92.

Jop, P., Y. Forterre, and O. Pouliquen. 2006. 'A constitutive law for dense granular flows', *Nature*, 441: 727-30.

Julien, Pierre Y. 2018. *River mechanics* (Cambridge University Press).

Jullien, R., P. Meakin, and A. Pavlovitch. 1992. '3-Dimensional Model for Particle-Size Segregation by Shaking', *Physical Review Letters*, 69: 640-43.

Jullien, R., P. Meakin, and A. Pavlovitch. 1993. 'Particle-Size Segregation by Shaking in 2-Dimensional Disc Packings', *Europhysics Letters*, 22: 523-28.

Kamrin, K., and G. Koval. 2012. 'Nonlocal Constitutive Relation for Steady Granular Flow (vol 108, 178301, 2012)', *Physical Review Letters*, 108.

Ketterhagen, W. R., J. S. Curtis, C. R. Wassgren, A. Kong, P. J. Narayan, and B. C. Hancock. 2007. 'Granular segregation in discharging cylindrical hoppers: A discrete element and experimental study', *Chemical Engineering Science*, 62: 6423-39.

Kiani Oshtorjani, Mehrdad, Liu Meng, and Christoph R. Müller. 2021. 'Accurate buoyancy and drag force models to predict particle segregation in vibrofluidized beds', *Physical Review E*, 103: 062903.

Kim, S. M., and K . Kamrin. 2020. 'Power-law scaling in granular rheology across flow geometries', *Physical Review Letters*, 125: 088002.

Kloss, C., C. Goniva, A. Hager, S. Amberger, and S. Pirker. 2012. 'Models, algorithms and validation for opensource DEM and CFD-DEM', *Progress in Computational Fluid Dynamics*, 12: 140-52.

Knight, J. B., H. M. Jaeger, and S. R. Nagel. 1993a. 'Vibration-Induced Size Separation in Granular Media - the Convection Connection', *Physical Review Letters*, 70: 3728-31.

Knight, James B, Heinrich M Jaeger, and Sidney R Nagel. 1993b. 'Vibration-induced size separation in granular media: The convection connection', *Physical Review Letters*, 70: 3728.

Koch, D. L., and R. J. Hill. 2001. 'Inertial effects in suspension and porous-media flows', *Annual Review of Fluid Mechanics*, 33: 619-47.

Komatsu, T. S., S. Inagaki, N. Nakagawa, and S. Nasuno. 2001. 'Creep motion in a granular pile exhibiting steady surface flow', *Physical Review Letters*, 86: 1757-60.

Kumar, A., D. V. Khakhar, and A. Tripathi. 2019. 'Theoretical calculation of the buoyancy force on a particle in flowing granular mixtures', *Physical Review E*, 100: 042909.

Kumaran, V. 2008. 'Dense granular flow down an inclined plane: from kinetic theory to granular dynamics', *Journal of Fluid Mechanics*, 599: 121-68.

Kumaran, V. 2015. 'Kinetic theory for sheared granular flows', *Comptes Rendus Physique*, 16: 51-61.
Lamb, Horace. 1924. *Hydrodynamics* (University Press).
Lange, A, M Schröter, MA Scherer, A Engel, I Rehberg, and Complex Systems. 1998. 'Fingering instability in a water-sand mixture', *European Physical Journal B*, 4: 475-84.
Langston, P. A., M. A. Al-Awamleh, F. Y. Fraige, and B. N. Asmar. 2004. 'Distinct element modelling of non-spherical frictionless particle flow', *Chemical Engineering Science*, 59: 425-35.
Li, X. Y., B. Sovilla, C. F. F. Jiang, and J. Gaume. 2021. 'Three-dimensional and real-scale modeling of flow regimes in dense snow avalanches', *Landslides*, 18: 3393-406.
Liu, M., and C. R. Müller. 2021. 'Lift force acting on an intruder in dense, granular shear flows', *Physical Review E*, 104: 064903.
Louge, Michel Y. 2003. 'Model for dense granular flows down bumpy inclines', *Physical Review E*, 67: 061303.
Lu, G., R. C. Hidalgo, J. R. Third, and C. R. Muller. 2016. 'Ordering and stress transmission in packings of straight and curved spherocylinders', *Granular Matter*, 18.
Lu, G., and C. R. Muller. 2020. 'Particle-shape induced radial segregation in rotating cylinders', *Granular Matter*, 22.
Lu, G., J. R. Third, and C. R. Muller. 2015. 'Discrete element models for non-spherical particle systems: From theoretical developments to applications', *Chemical Engineering Science*, 127: 425-65.
Luding, S., and F. Alonso-Marroquín. 2011. 'The critical-state yield stress (termination locus) of adhesive powders from a single numerical experiment', *Granular Matter*, 13: 109-19.
Lun, C. K. K, S. B Savage, D. J Jeffrey, and N Chepurniy. 1984. 'Kinetic theories for granular flow: inelastic particles in Couette flow and slightly inelastic particles in a general flowfield', *Journal of Fluid Mechanics*, 140: 223-56.
Martiniani, S. 2017. 'On the complexity of energy landscapes: algorithms and a direct test of the Edwards conjecture', University of Cambridge.
Martiniani, S., K. J. Schrenk, K. Ramola, B. Chakraborty, and D. Frenkel. 2017. 'Numerical test of the Edwards conjecture shows that all packings are equally probable at jamming', *Nature Physics*, 13: 848-51.

Massmeyer, A., E. Di Giuseppe, A. Davaille, T. Rolf, and P. J. Tackley. 2013. 'Numerical simulation of thermal plumes in a Herschel–Bulkley fluid', *Journal of Non-Newtonian Fluid Mechanics*, 195: 32-45.

McLaren, C. P., T. M. Kovar, A. Penn, C. R. Muller, and C. M. Boyce. 2019. 'Gravitational instabilities in binary granular materials', *Proceedings of the National Academy of Sciences of the United States of America*, 116: 9263-68.

Mehta, A., and S. F. Edwards. 1990. 'A Phenomenological Approach to Relaxation in Powders', *Physica A*, 168: 714-22.

Metzger, M. J., B. Remy, and B. J. Glasser. 2011. 'All the Brazil nuts are not on top: Vibration induced granular size segregation of binary, ternary and multi-sized mixtures', *Powder Technology*, 205: 42-51.

MiDi, G. D. R. 2004. 'On dense granular flows', *European Physical Journal E*, 14: 341-65.

Müller, C. R., J. F. Davidson, J. S. Dennis, P. S. Fennell, L. F. Gladden, A. N. Hayhurst, M. D. Mantle, A. C. Rees, and A. J. Sederman. 2006. 'Real-time measurement of bubbling phenomena in a three-dimensional gas-fluidized bed using ultrafast magnetic resonance imaging', *Physical Review Letters*, 96: 154504.

Müller, C. R., D. J. Holland, A. J. Sederman, S. A. Scott, J. S. Dennis, and L. F. Gladden. 2008. 'Granular temperature: Comparison of Magnetic Resonance measurements with Discrete Element Model simulations', *Powder Technology*, 184: 241-53.

Müller, T., D. de las Heras, I. Rehberg, and K. Huang. 2015. 'Ordering in granular-rod monolayers driven far from thermodynamic equilibrium', *Physical Review E*, 91.

Nakagawa, M., S. A. Altobelli, A. Caprihan, E. Fukushima, and E. K. Jeong. 1993. 'Non-invasive measurements of granular flows by magnetic resonance imaging', *Experiments in fluids*, 16: 54-60.

Nettleton, L. L. 1934. 'Fluid Mechanics of Salt Domes', *AAPG Bulletin*, 18: 1175-204.

Noetinger, Benoît 1989. 'A two fluid model for sedimentation phenomena', *Physica A: Statistical Mechanics and its Applications*, 157: 1139-79.

Ogawa, S. 1978. "Multitemperature theory of granular materials." In *Proc. of the US-Japan Seminar on Continuum Mechanical and Statistical Approaches in the Mechanics of Granular Materials, 1978*, 208-17. Gakajutsu Bunken Fukyu-Kai.

Olafsen, J. S., and J. S. Urbach. 1998. 'Clustering, order, and collapse in a driven granular monolayer', *Physical Review Letters*, 81: 4369-72.

Ottino, J. M. 2006. 'Granular matter as a window into collective systems far from equilibrium, complexity, and scientific prematurity', *Chemical Engineering Science*, 61: 4165-71.

Pan, T. W., D. D. Joseph, and R. Glowinski. 2001. 'Modelling Rayleigh-Taylor instability of a sedimenting suspension of several thousand circular particles in a direct numerical simulation', *Journal of Fluid Mechanics*, 434: 23-37.

Parker, D. J., T. W. Leadbeater, X. F. Fan, M. N. Hausard, A. Ingram, and Z. F. Yang. 2008. 'Positron imaging techniques for process engineering: recent developments at Birmingham', *Measurement Science and Technology*, 19: 094004.

Penn, Alexander, Takuya Tsuji, David O Brunner, Christopher M Boyce, Klaas P Pruessmann, and Christoph R Müller. 2017. 'Real-time probing of granular dynamics with magnetic resonance', *Science advances*, 3: e1701879.

Pereira, G. G., S. Pucilowski, K. Liffman, and P. W. Cleary. 2011. 'Streak patterns in binary granular media in a rotating drum', *Applied Mathematical Modelling*, 35: 1638-46.

Pouliquen, O., J. Delour, and S. B. Savage. 1997. 'Fingering in granular flow', *Nature*, 386: 816-17.

Pouliquen, O., and Y. Forterre. 2009. 'A non-local rheology for dense granular flows', *Philosophical Transactions of the Royal Society a-Mathematical Physical and Engineering Sciences*, 367: 5091-107.

Reddy, K. A., Y. Forterre, and O. Pouliquen. 2011. 'Evidence of Mechanically Activated Processes in Slow Granular Flows', *Physical Review Letters*, 106.

Richtmyer, R. D. 1960. 'Taylor Instability in Shock Acceleration of Compressible Fluids', *Communications on Pure and Applied Mathematics*, 13: 297-319.

Rosato, A., K. J. Strandburg, F. Prinz, and R. H. Swendsen. 1987. 'Why the Brazil nuts are on top: Size segregation of particulate matter by shaking', *Physical Review Letters*, 58: 1038-40.

Rusche, H. 2003. 'Computational fluid dynamics of dispersed two-phase flows at high phase fractions', Imperial College London (University of London).

Saasen, A., and J. D. Ytrehus. 2018. 'Rheological properties of drilling fluids: use of dimensionless shear rates in herschel-bulkley and power-law models', *Applied Rheology*, 28.

Sandnes, B., H. A. Knudsen, K. J. Måløy, and E. G. Flekkøy. 2007. 'Labyrinth Patterns in Confined Granular-Fluid Systems', *Physical Review Letters*, 99: 038001.

Savage, S. B., and D. J. Jeffrey. 1981. 'The Stress Tensor in a Granular Flow at High Shear Rates', *Journal of Fluid Mechanics*, 110: 255-72.

Savage, S. B., and C. K. K. Lun. 1988. 'Particle-Size Segregation in Inclined Chute Flow of Dry Cohesionless Granular Solids', *Journal of Fluid Mechanics*, 189: 311-35.

Seidler, G. T., G. Martinez, L. H. Seeley, K. H. Kim, E. A. Behne, S. Zaranek, B. D. Chapman, S. M. Heald, and D. L. Brewe. 2000. 'Granule-by-granule reconstruction of a sandpile from x-ray microtomography data', *Physical Review E*, 62: 8175-81.

Seife, C. 2005. 'So much more to know', *Science*, 309: 78-102.

Shinbrot, T., and F. Muzzio. 2000. 'Nonequilibrium patterns in granular mixing and segregation', *Physics Today*, 53: 25-30.

Shinbrot, T., and F. J. Muzzio. 1998. 'Reverse buoyancy in shaken granular beds', *Physical Review Letters*, 81: 4365-68.

Shishodia, N., and C. R. Wassgren. 2001. 'Particle segregation in vibrofluidized beds due to buoyant forces', *Physical Review Letters*, 87.

Silbert, L. E., D. Ertas, G. S. Grest, T. C. Halsey, D. Levine, and S. J. Plimpton. 2001. 'Granular flow down an inclined plane: Bagnold scaling and rheology', *Physical Review E*, 64.

Simsek, E., S. Wirtz, V. Scherer, H. Kruggel-Emden, R. Grochowski, and P. Walzel. 2008. 'An experimental and numerical study of transversal dispersion of granular material on a vibrating conveyor', *Particulate Science and Technology*, 26: 177-96.

Sinnott, M. D., and P. W. Cleary. 2009. 'Vibration-induced arching in a deep granular bed', *Granular Matter*, 11: 345-64.

Song, C. M., P. Wang, Y. L. Jin, and H. A. Makse. 2010. 'Jamming I: A volume function for jammed matter', *Physica a-Statistical Mechanics and Its Applications*, 389: 4497-509.

Song, C., P. Wang, and H. A. Makse. 2008. 'A phase diagram for jammed matter', *Nature*, 453: 629-32.

Sperl, M. 2006. 'Experiments on corn pressure in silo cells - translation and comment of Janssen's paper from 1895', *Granular Matter*, 8: 59-65.
Stannarius, R. 2017. 'Magnetic resonance imaging of granular materials', *Review of Scientific Instruments*, 88.
Staron, L. 2018. 'Rising dynamics and lift effect in dense segregating granular flows', *Physics of Fluids*, 30: 123303.
Tan, M. L., and I. Goldhirsch. 1998. 'Rapid granular flows as mesoscopic systems', *Physical Review Letters*, 81: 3022.
Taylor, G. I. 1950. 'The instability of liquid surfaces when accelerated in a direction perpendicular to their planes. I', *Proceedings of the Royal Society of London*, 201: 192-96.
Taylor, S., and E. Brodsky. 2017. 'Granular temperature measured experimentally in a shear flow by acoustic energy', *Physical Review E*, 96: 032913.
Thomas, N. 2000. 'Reverse and intermediate segregation of large beads in dry granular media', *Physical Review E*, 62: 961-74.
Tripathi, A., and D. V. Khakhar. 2011. 'Numerical simulation of the sedimentation of a sphere in a sheared granular fluid: a granular Stokes experiment', *Physical Review Letters*, 107: 108001.
Tripathi, A., and D. V. Khakhar.. 2013. 'Density difference-driven segregation in a dense granular flow', *Journal of Fluid Mechanics*, 717: 643-69.
Trujillo, L., and H. J. Herrmann. 2003. 'Hydrodynamic model for particle size segregation in granular media', *Physica A*, 330: 519-42.
Trulsson, M., M. Bouzid, J. Kurchan, E. Clement, P. Claudin, and B. Andreotti. 2015. 'Athermal analogue of sheared dense Brownian suspensions', *European Physical Letters*, 111.
Tsuji, Y., T. Kawaguchi, and T. Tanaka. 1993. 'Discrete particle simulation of two-dimensional fluidized bed', *Powder Technology*, 77: 79-87.
Tsuji, Yutaka, Toshitsugu Tanaka, and T Ishida. 1992. 'Lagrangian numerical simulation of plug flow of cohesionless particles in a horizontal pipe', *Powder Technology*, 71: 239-50.
Tunuguntla, Deepak R, Thomas Weinhart, and Anthony R Thornton. 2017. 'Comparing and contrasting size-based particle segregation models', *Computational Particle Mechanics*, 4: 387-405.
van der Vaart, K., P. Gajjar, G. Epely-Chauvin, N. Andreini, J. M. N. T. Gray, and C. Ancey. 2015. 'Underlying Asymmetry within Particle Size Segregation', *Physical Review Letters*, 114.

van der Vaart, K., M. P. V. Lantman, T. Weinhart, S. Luding, C. Ancey, and A. R. Thornton. 2018. 'Segregation of large particles in dense granular flows suggests a granular Saffman effect', *Physical Review Fluids*, 3.

Vanarase, A. U., M. Alcala, J. I. J. Rozo, F. J. Muzzio, and R. J. Romanach. 2010. 'Real-time monitoring of drug concentration in a continuous powder mixing process using NIR spectroscopy', *Chemical Engineering Science*, 65: 5728-33.

Vinningland, J. L., O. Johnsen, E. G. Flekkoy, R. Toussaint, and K. J. Maloy. 2007. 'Granular rayleigh-taylor instability: Experiments and simulations', *Physical Review Letters*, 99.

Voltz, C., W. Pesch, and I. Rehberg. 2002. 'Rayleigh-Taylor instability in a sedimenting suspension', *Physical Review E*, 65.

Weinhart, T., R. Hartkamp, A. R. Thornton, and S. Luding. 2013. 'Coarse-grained local and objective continuum description of three-dimensional granular flows down an inclined surface', *Physics of Fluids*, 25: 070605.

Weinhart, T., C. Labra, S. Luding, and J. Y. Ooi. 2016. 'Influence of coarse-graining parameters on the analysis of DEM simulations of silo flow', *Powder Technology*, 293: 138-48.

Weinhart, T., A. R. Thornton, S. Luding, and O. Bokhove. 2012. 'From discrete particles to continuum fields near a boundary', *Granular Matter*, 14: 289-94.

Wieghardt, K. 1975. 'Experiments in Granular Flow', *Annual Review of Fluid Mechanics*, 7: 89-114.

Windows-Yule, C. R. K., T. Weinhart, D. J. Parker, and A. R. Thornton. 2014. 'Effects of Packing Density on the Segregative Behaviors of Granular Systems', *Physical Review Letters*, 112.

Wysocki, Adam, C Patrick Royall, Roland G Winkler, Gerhard Gompper, Hajime Tanaka, Alfons van Blaaderen, and Hartmut Löwen. 2009. 'Direct observation of hydrodynamic instabilities in a driven non-uniform colloidal dispersion', *Soft Matter*, 5: 1340-44.

Xu, N., D. Frenkel, and A. J. Liu. 2011. 'Direct Determination of the Size of Basins of Attraction of Jammed Solids', *Physical Review Letters*, 106.

Xue, K., X. L. Shi, J. S. Zeng, B. L. Tian, P. P. Han, J. R. Li, L. Liu, B. Q. Meng, X. H. Guo, and C. H. Bai. 2020. 'Explosion-driven interfacial instabilities of granular media', *Physics of Fluids*, 32.